USING LINEAR INVERSE METHODS AND FINITE ELEMENT MODELS TO EXPLORE SENSITIVITY TO HOMOGENEOUS ELASTIC HALF-SPACE ASSUMPTIONS IN DEFORMATION MODELS OF THE 2000 ERUPTION OF HEKLA VOLCANO, ICELAND

by

SARAH KATHERINE COMPTON

SAMANTHA HANSEN, COMMITTEE CHAIR
TIMOTHY MASTERLARK
CHRISTODOULOS KYRIAKOPOULOS
ANDREW GOODLIFFE
CHUNMIAO ZHENG

A DISSERTATION

Submitted in partial fulfillment of the requirements
for the degree of Doctor of Philosophy in
the Department of Geological Sciences
in the Graduate School of
The University of Alabama

TUSCALOOSA, ALABAMA

2013

ABSTRACT

On February 26, 2000, the 12-day, 18th historic eruption of Hekla volcano in Iceland began with an explosive Subplinian eruptive column and pyroclastic basaltic flows fed by column collapses (Höskuldsson et al., 2007). Interferometric synthetic aperture radar (InSAR) captured the deformation pattern associated with the movement of a shallow fissure (i.e. dike) during the eruption (Ofeigsson et al., 2011). These data present the opportunity to use inverse methods to estimate parameters describing the behavior of the eruptive fissure (Fukushima et al., 2010, Anderson and Segall, 2011, Ofeigsson et al., 2011). I use the 2000 eruption of Hekla as an example in linear inversions that investigate the influence of topography and layered rock properties in 3-D finite element models (FEMs) on estimates of parameters associated with the fissure movement.

FEMs are used for this study because they are the best type of model which allow for arbitrary geometric configurations of the domain and effectively satisfies the static elastic governing equations. The results of the study are:

1. FEMs of fissure movement are sensitive to a free-surface geometry representing topography but less sensitive to rock property distribution.
2. The estimated magnitude of each movement responds differently to unique inputs. Including topography increased estimates of strike-slip motion and decreased estimates of opening relative to a homogeneous elastic half-space model or a layered elastic half-space model.

3. Including topography directly into the model domain allows exploration of arbitrary dike geometry, such as a dike which changes strike, which is not possible with HEHS assumptions and topographic corrections, but is indicated in this study.

The flexibility and power of FEMs far outweighs the computational burden they used to present. The results of this study will guide future modelers to required steps to build the most accurate and efficient model to estimate parameters related to fissure behavior during an eruption. These results can help elucidate the plumbing system of a volcano, including the relationship between processes in the magma chamber and in the conduit during an eruption. This can help geologists, volcanologists, and hazard assessment teams assemble more accurate eruption forecasts.

DEDICATION

This dissertation is dedicated to my family, which is quite extensive, to my close friends, and to my adviser(s). A special dedication goes to my husband, Kevin, whose unconditional love and support through the roller-coaster that is scientific research helped make this dissertation a reality.

LIST OF ABBREVIATIONS AND SYMBOLS

A	Askja
Bá	Bárbarbunga
cm	centimeters
E	easting
EVZ	Eastern Volcanic Zone
FEM(s)	finite element model(s)
GF(s)	Green's Function(s)
GPa	Giga-Pascal
GPS	Global Positioning System
Gr	Grímsvötn
HEHS	Homogeneous elastic half-space
InSAR	Interferometric Synthetic Aperture Radar
km	kilometers
Ka	Katla
Kr	Krafla
LEHS	Layered elastic half-space
LOS	line of sight
m	meters
mm	millimeters

N	northing
NVZ	Northern Volcanic Zone
RADAR	Radio direction and ranging
SISZ	South Icelandic Seismic Zone
SRTM	Shuttle Radar Tomography Mission
SSE	Summed squared error
μrad	microradian
UTM	Universal Transverse Mercator
WGS	World G
WVZ	Western Volcanic Zone
$^{-1}$	inverse
$\lvert\ \rvert$	absolute value of
$\boldsymbol{d}$	displacement vector
Δ	change in
∂	partial derivative
$\boldsymbol{e}$	error vector
E	Young's modulus
ε	elastic strain
$\sum_{i=1}^{n}$	summation from i=1 to n
F_i	body force in i^{th} direction
G	Shear modulus
$\boldsymbol{G}$	matrix of Green's Functions
∇	Gradient: vector differential operator

$\boldsymbol{m}$	slip distribution vector
$\boldsymbol{m}^{est}$	estimated slip distribution vector
$M(U)$	average magnitude of displacement
N	number of calculation points
ρ	density
R_i	residual at pixel *i*
s_0^2	Variance of the baseline model
s_1^2	Variance of the compared model
σ	stress
T	transpose
ν	Poisson's ratio
u_1	displacement in the x direction
u_i	displacement for node in kinematic equation
uLOS	displacement in the LOS direction
U_i^{FE}	predicted deformation from the FEM at *i*
U_i^{HEHS}	predicted deformation from the HEHS at *i*
$\Delta(U)$	average difference in deformation prediction
u_2	displacement in the y direction
V_s	shear-wave velocity
u_3	displacement in the z direction
x	Cartesian coordinate
y	Cartesian Coordinate
z	Cartesian Coordinate

=	Equal to

ACKNOWLEDGEMENTS

I've said it before, and I'll say it again; these belong further up front. Regardless, there are many people to thank so let's get to it. First off, I'd like to thank my adviser, Dr. Timothy Masterlark for his help and loyalty to me these four years and especially these last few months. Thank you for that and much more, but especially for requiring me to take differential equations, and you know why. Remember to be careful which classes you recommend, Tim: you never know what all might follow your student home from them.

Thank you to the rest of my committee, Drs. Samantha Hansen, Christodoulos Kyriakopoulos, Andrew Goodliffe, and Chunmiao Zheng. Thank you all for your hard work and continuous support. Thank you especially to Samantha Hansen for stepping up as committee chair and performing the duties beautifully. Thank you also to Christos for your remarkable ability to come into the research so late but still provide insightful, timely, and helpful feedback. Thank you to the department of Geological Sciences and the University of Alabama for funding my research and allowing me the freedom to pursue it.

Thank you to the colleagues I've met along the way that helped mold this project into reality. Thank you to Dr. Matthew Haney and Andrew Nies for the tomography of Hekla. Thank you to Dr. Rikke Pedersen for the helpful conversations. Thank you to Dr. Benedik Ofeigsson for laying the groundwork from which I based my research, including the processed InSAR data, which was crucial for this research and answers to my associated questions. Many bright scholars walked in and out of the lab while I worked and all helped my research in one way or another. Thank you to Dr. Kristin Hellem Hughes, who pointed me towards the University of

Alabama and whose dissertation has been an absolutely invaluable resource. Thank you to Erika Ronchin, M.Sc., Dr. Wei Tao, and Jonathan Stone, M.Sc. for your input, discussions, guidance, and sometimes annoyingly good questions. Thank you also to Halldor Olafsson for being such an amazing field guide.

Thank you to the friends I've met and made along the way that helped me get through these past four years with much more joy than I would have otherwise. Thank you to Meghan Alesce, Tacoma Morrissey, and my CrossFit friends who have witnessed first-hand the required release of stresses that accompany a task such as a dissertation.

Finally, I would like to thank God, my husband Kevin, my parents Edward and Kathy Needy, and the rest of my family. To Kevin, thank you for your love, support, and encouragement, as well as helping me keep the dissertation where it belongs; firmly in the backseat to life. To my parents, your unconditional love and support have been a blessing throughout my life. Thank you. To the rest of my family: Dan Stankovich, Kim Stankovich, Caiti Stankovich, Rae Stankovich, Danni Lee Stankovich, CJ Stankovich, Robert Gosnell, Jill Gosnell, Mark Gosnell, Zach Gosnell, David Needy, Nichole Needy, Aurora Needy, Ashlyn Needy, Eric Needy, Barbara Compton, Dusty Compton, and Amber Compton (phew!), I am thankful every day to have all of you in my life and in my corner. Thank you.

CONTENTS

List of Tables

List of Figures

CHAPTER 1

INTRODUCTION

PROJECT BACKGROUND

The 18th historic eruption of Hekla volcano in Iceland (Figure 1.1) began on February 26, 2000. The 12-day eruption started explosively, with a Subplinian eruptive column and pyroclastic basaltic flows fed by column collapses (Höskuldsson et al., 2007). Interferometric synthetic aperture radar (InSAR) captured the deformation pattern (Figure 1.2), presumably associated with coeruptive magma chamber deflation and the movement of magma into a shallow fissure (i.e. dike) during the eruption (Ofeigsson et al., 2011).

InSAR and GPS have better spatial and temporal resolution than previous geodetic methods such as tiltmeters (Sturkell et al., 2006), and InSAR provides this resolution from a satellite platform. As such, InSAR data have revolutionized our ability to observe and quantify deformation of the surface of the earth caused by eruption-related volcanic processes and are invaluable when characterizing volcanic activity (e.g. Anderson and Segall, 2011; Masterlark, 2007; Ofeigsson et al. 2011; Pedersen et al., 2009; Solaro et al., 2010; Sturkell et al., 2006). The InSAR data used in this study are acquired from two passes of a satellite over Hekla at different times. The first pass occurred in October, 1999, and the second pass occurred in June, 2000. During each pass, a measurement was made of the distance between the ground and the

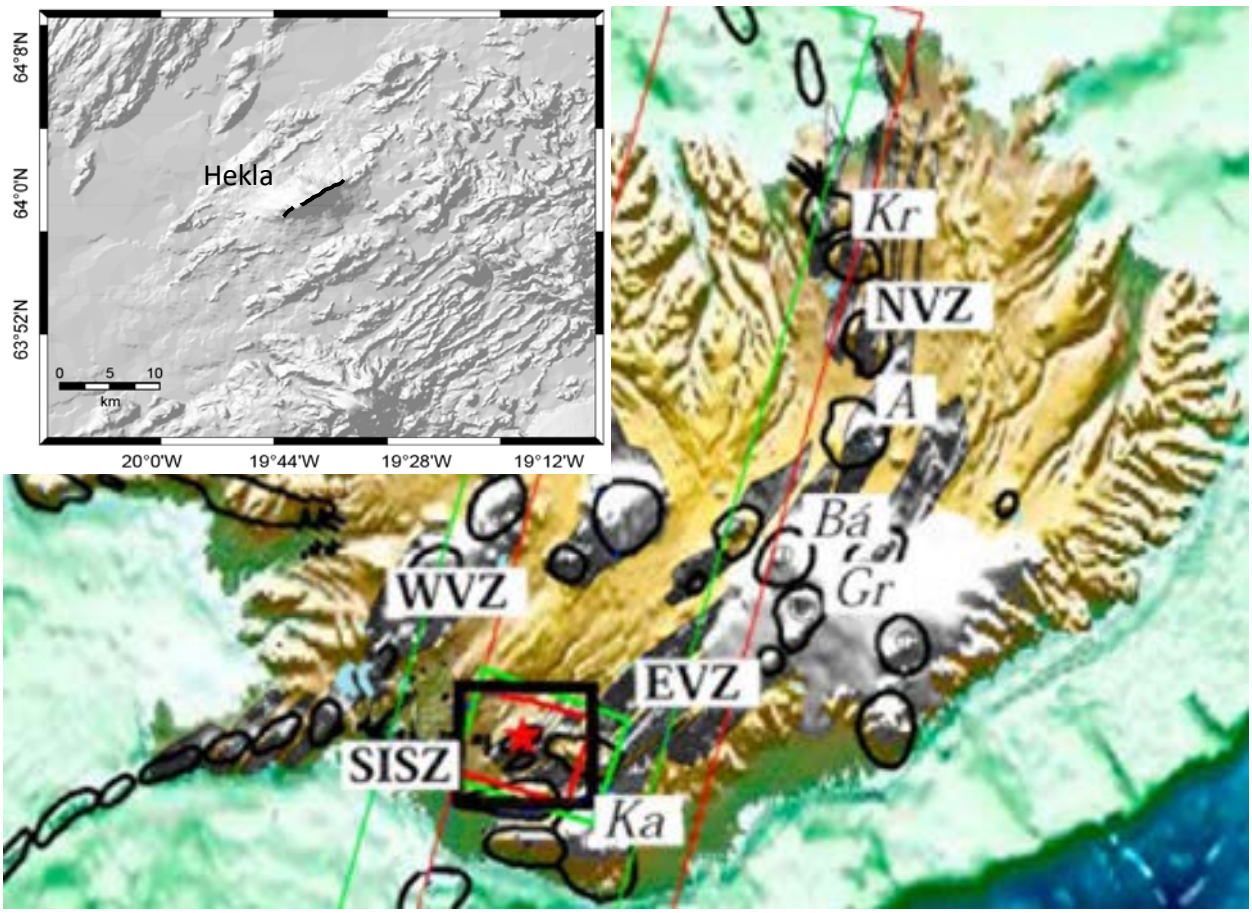

Figure 1.1. General tectonic setting of Iceland, which straddles the Mid-Atlantic Ridge and has volcanic systems with central volcanoes (black oval outlines) and dike swarms (gray areas; modified from Ofeigsson et al., 2011). Colored boxes indicate InSAR passes. The red box is ERS track 52 and is the track of interest. The green track is Envisat track 324. Hekla is located near the intersection of the South Icelandic Seismic Zone (SISZ) and the Eastern Volcanic Zone (EVZ) and is the red star in the center of the outlined black box in south-central Iceland. Other volcanic zones labeled are the Western Volcanic Zone (WVZ) and Northern Volcanic Zone (NVZ). Labeled volcanic systems are A, Askja; Bá, Bárdarbunga, Gr, Grímsvötn, Ka, Katla, Kr, Krafla. Inset is a hillshade image of Hekla from SRTM data.

satellite. The difference between those measurements is interpreted to be the average ground deformation of Hekla in that interval. Because the eruption occurred during that time period, deformation sources related to the eruption, such as a dike opening, are interpreted to be the main source of the deformation. These deformation data present the opportunity to use inverse methods which can estimate parameters describing the behavior of the feeding fissure, based on the observed deformation (Fukushima et al., 2010; Anderson and Segall, 2011; Ofeigsson et al., 2011).

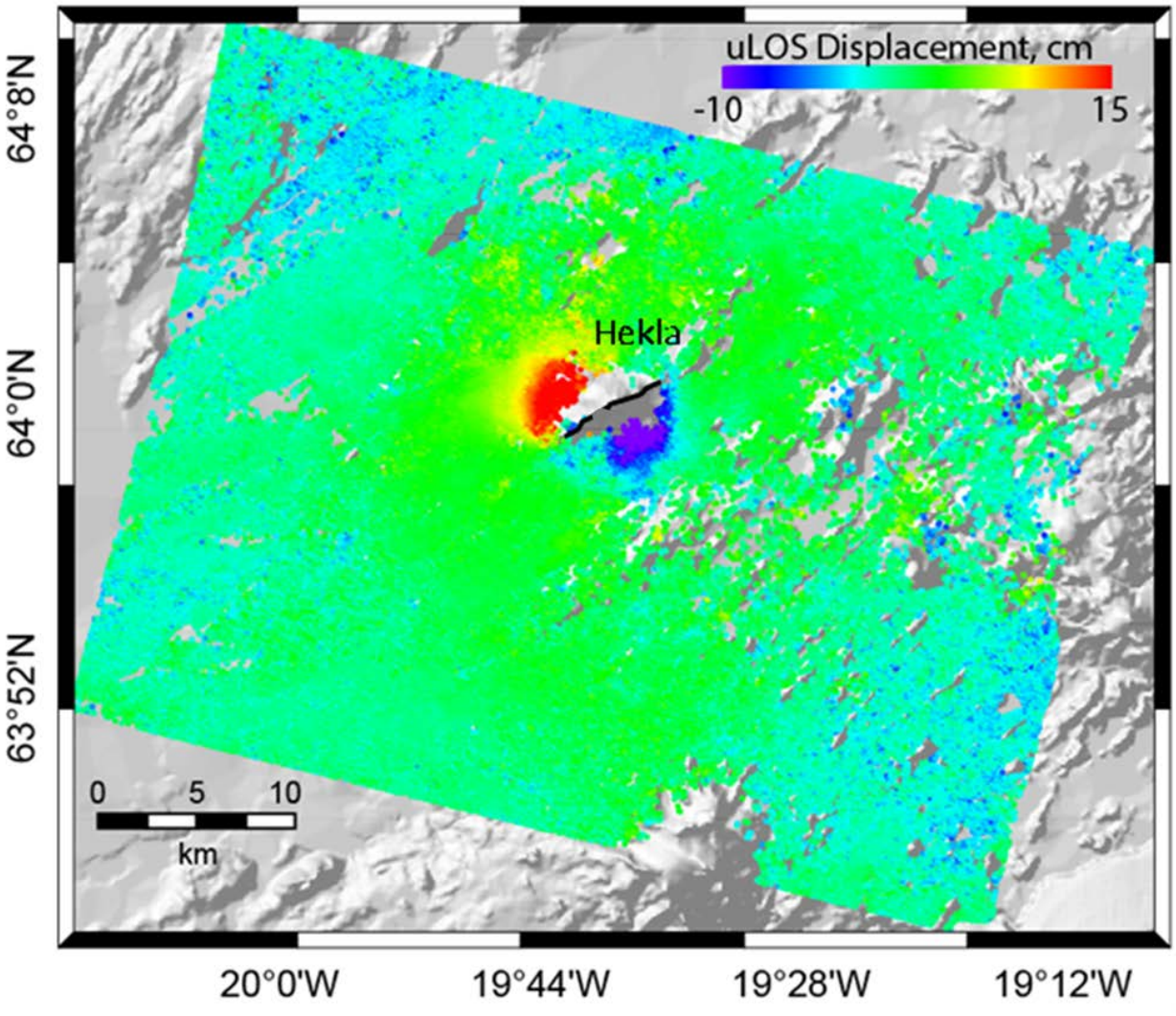

Figure 1.2. InSAR line of sight (LOS) displacement between October 15, 1999, and June 16, 2000, capturing the deformation presumably associated with the dike movement during the 2000 eruption of Hekla volcano in Iceland (modified from Ofeigsson et al., 2011). The northwest side of the volcano moved over 15 cm towards the satellite, and the southeast side of the volcano moved over 10 cm away from the satellite.

The 2010 eruption of Eyjafjallajökull shut down air travel to significant parts of Europe for about four days (http://www.theguardian.co/uk), highlighting the effect Icelandic volcanoes can have on the modern world. Some of Hekla's prehistoric eruptions have spewed layers of ash and tephra throughout northern Europe, and tephras from selected eruptions are recognized as main Holocene geochronologic markers as far east as Sweden (Dugmore, 1996; Swindles et al., 2011). The erupted volume and wind direction are not the only controlling factors which

determine how far ash and tephra will travel; eruption column dynamics also play a role (Swindles et al., 2011). Dike shape and size, which are related to the amount of opening during an eruption, are directly tied to eruption column dynamics (Giberti and Wilson, 1989). Thus, understanding dike behavior at Hekla could provide insights for eruption column dynamics and possibly provide additional background information for ash-transport forecasts for future eruptions. Additionally, lethal levels of fluorine in tephra from several of Hekla's most recent eruptions have killed thousands of livestock nearly 200 km away (Gronvöld et al., 1983; Gudmundsson et al., 1992; Thorarinsson and Sigvaldason, 1971) This, coupled with Hekla's eruption history, highlight the need to understand the inner workings of this volcano.

I explore the effects of flat, free-surface geometry and rock property homogeneity on models of the dike behavior during the 2000 eruption and suggest models of volcanoes should include a free-surface geometry which honors topography and material properties which reflect the local heterogeneity of the rock properties. The effects of these additions to the model domain are explored by holding the dike geometry fixed and comparing the predictions of an HEHS model, a FEM with a free-surface representing topography, an LEHS, and a FEM with a free surface representing topography and layered material properties reflecting the measured layering of local rock properties.

Parameters for the dike geometry at Hekla are poorly constrained, as demonstrated by the widely varying results between geodetic studies attempting to decipher the geometry of this internal structure (Table 1.1) (Linde et al., 1993; Ofeigsson et al., 2011; Sturkell et al., 2013). One way to better constrain these parameters with the existing geodetic data may be by reassessing some fundamental assumptions necessary for current models, resulting in models which better represent the real system. In particular, two standard assumptions in volcano

deformation models, homogeneity or rock properties and flat free surface, strongly deviate from the actual volcano system. This dissertation utilizes modeling techniques never before attempted with deformation data from Hekla by including topography and layered material properties reflecting measured rock property variations. These new techniques have implications for Hekla, but also for other active volcanic systems (e.g. Piton de la Fournaise on Réunion Island) whose best-fit dike geometry does not fully explain the deformation data, likely as a result of assumed homogeneity in material properties of the model (Fukushima et al., 2010). The limited effectiveness of the results of these models is directly related to the limits placed on the models by the fundamental model assumptions. These assumptions were once necessary simplifications required to analyze the systems, but advancements in technology have rendered these simplifications obsolete. The bias these assumptions place on predictions has been demonstrated in several studies (Fukushima et al., 2010; Masterlark, 2003, 2007; Williams and Wadge 1998, 2000), and is no longer acceptable. Models which are a closer approximation of the system yield different results than models currently employed and should yield better predictions from the best-fit results of these models.

ICELAND'S GEOLOGIC SETTING

Iceland is the only sub-aerial expression of the Mid-Atlantic Ridge (MAR) and is situated over a melt spot in the North Atlantic Ocean. The interaction between the ridge and melt spot causes eastward jumps in the MAR and reorganization of the plate boundary, leading to a uniquely complex and fascinating tectonic and geologic setting (Figure 1.1; Darbyshire et al., 2000; Sigmundsson, 2006, Geirsson et al., 2012). The interaction results in the production of an oceanice crust that is 20-40 km thick (Darbyshire et al., 2000; Maclennan et al., 2001; Fedorova

et al., 2005; Kelly and Barton, 2008), roughly 3 to 5 times as thick as typical MAR crust, which is about 6-8 km thick (e.g. Sigmundsson, 2006).

The MAR is exposed in Iceland as a series of volcanic zones, containing more than 30 active volcanic systems. A volcanic system is defined as a main area of volcanic production, some with central volcanoes and/or collapse structures, a high temperature geothermal system, and an associated fissure swarm (Darbyshire et al., 2000; Pedersen, 2013, personal comm; Sigmundsson, 2006). Two of thesee volcanic zones are in the south of Iceland; the Western Volcanic Zone (WVZ) and the Eastern Volcanic Zone (EVZ). A third volcanic zone, the Northern Volcanic Zone (NVZ), is the northern extension of the EVZ (Figure 1.1). The WVZ and EVZ are rift zones oriented roughly subparallel to each other, and these take up all of the ~19 mm/yr plate motion, although most of that motion is currently taken up by the EVZ (Geirsson et al., 2012; Jónsson et al, 1997; LaFemina et al., 2005; Sigmundsson et al., 1995; Sigmundsson, 2006). The two volcanic zones are separated by an active transform fault zone, the South Iceland Seismic Zone (SISZ), which is accommodating the strain accumulation between the WVZ and the EVZ in the form of "bookshelf" faulting (Darbyshire et al., 2000; Jónsson et al, 1997; LaFemina et al., 2005; Sigmundsson et al., 1995; Sigmundsson, 2006). The volcanic zones may be split into two types of neovolcanic zones: volcanic flank zones have almost no or little spreading associated with them, while volcanic rift zones are associated with extensive rifting, as the name implies (Sigmundsson, 2006).

The SISZ had significant earthquakes in 2000 and 2008, and interseismic deformation is consistent with a single east-trending shear zone below the brittle crust (Arnadottir et al., 2005, 2009; Decriem et al., 2010; Geirsson et al., 2012; Pedersen et al., 2003). The EVZ has not had a major rifting episode since the 1862-1864 eruption of Tröllagígar (Jónsson et al., 1997), placing

the present deformation of the EVZ into the inter-rifting phase with well-documented strain accumulation (Arnadottir, 2005, 2009; Jónsson et al., 1997; LaFemina et al., 2005), which occurs most rapidly at the western part of the EVZ (Geirsson et al., 2012; LaFemina, 2005).

1. Geodesy in Iceland

Crustal deformation due to Iceland's unique setting has drawn the attention of geodesists for decades, including German geodesists inspired by Wegner's theory of Continental Drift who installed Iceland's first geodetic network in 1938 to measure the widening of the rift zone in the northern part of the country (Sigmundsson, 2006). Strainmeters and seismometers were (and continue to be) installed throughout the country. As early as 1950, Eysteinn Tryggvason installed a network of wet and dry leveling stations, even using lake surfaces as tiltmeters (Sigmundsson, 2006; Sturkell et al., 2006). Decker et al. (1971) used electronic leveling surveys to measure extension in Iceland in the context of the (then) relatively new theory of plate tectonics. Their study indicated the eastern rift zone in Iceland widened about 6-7 cm during 1967-1970, possibly during the 1970 event at Hekla. As technology progressed, so did the geologic and geodetic exploration of Iceland. The early 1980's witnessed the advent of GPS, and initial GPS measurements were made in Iceland in 1986, followed shortly by InSAR measurements in the early 1990's (Gerisson et al., 2012; Sigmundsson, 1992, 2006).

HEKLA VOLCANO GEOLOGIC SETTING

Hekla lies on the western edge of the EVZ, near the intersection of the EVZ and SISZ (Figure 1.1). It is one of Iceland's most active volcanoes, producing more silicic material than any other Icelandic volcano since glacial times (Sigmarsson et al., 199; Thorarinsson, 1967).

Before 1970, the eruption frequency and style at Hekla was one or two relatively explosive, silicic eruptions every century, and the silica content of the initial volcanic products from those eruptions was directly related to the repose time between eruptions (Sigmundsson, 2006; Sigvaldason, 1974; Thorarisnsson, 1967). The repose time was (and still is) correlated to the volume of erupted material, such that about 1 km^3 erupts every century (Sigmundsson, 2006, Sigvaldason, 1967; Thorarinsson, 1967). Since 1970, there has been a more effusive, intermediate (andesite to andesitic basalt) eruption roughly every decade (Grönvold et al., 1983; Gudmundsson et al., 1992; Höskuldsson et al., 2007; Thorarinsson and Sigvaldason, 1972), the most recent of which occurred in February, 2000. Therefore, another decadal eruption is, by now, three years overdue (Figure 1.3).

Hekla's ridge strikes ~N65°E, slightly oblique to most fissures in the EVZ, indicating that the stress field at Hekla may be affected by the junction of the rift, transform, and volcanic flank zone (Soosalu and Einarsson, 1997), all of which are in the vicinity of Hekla. The ridge and eruptive fissure strike are similar to one of the main fault trends in the seismic zone, indicating the horizontal shear tectonics of the SISZ may play a bigger role in the fissure orientation than the extensional tectonics of the rift zone (Gronvöld et al., 1983). Also, Hekla is closer to the axis of the SISZ and the little inter-eruption seismicity that exists is similar to the pattern of seismicity for the SISZ, signifying Hekla is in the SISZ (Soosalu and Einarsson, 2005).

Hekla has been studied extensively using various geodetic methods such as borehole strain meters, dry- and continuous tilt, electronic distance measurements, continuous and episodic GPS, and InSAR (Geirsson et al., 2012; Gronvöld et al., 1983; Ofeigsson et al., 2011; Sigmundsson et al., 1992; Sturkell et al., 2006, 2013; Tryggvason, 1994). These studies

attempted to constrain the depth to the inferred magma chamber under Hekla with varying results, as summarized in Table 1.1. Estimates of the magma chamber depth from studies before the 2000 eruption varied from 5-11 km depth, but Soosalu and Einarsson (2003) used seismic tomography under Hekla with a resolution of 800 m to indicate that if a chamber with a diameter of 800 m or greater exists under Hekla, it exists above 4 km or below 14 km. Results from Ofeigsson et al. (2011), based on InSAR, are in agreement with that constraint. Recent results from Sturkell et al. (2013) using GPS and strain measurements estimate the chamber is at levels deeper than 10 km. Some studies have also attempted to solve the best-fit geometry of the dike with varying results (Table 1.1). Linde et al. (1993) use borehole strain meter data to estimate a dike which is connected to the chamber, resulting in a dike with dimensions of 4 km by 4 km and 85 cm of opening. Ofeigsson et al. (2011) use inversions of coeruptive InSAR data in topographically corrected HEHS models. Their results estimate a 6.6 km long dike, extending to 5.8 km with a 70-73° dip to the southeast, which opened 18-23 cm with 23-31 cm of left-

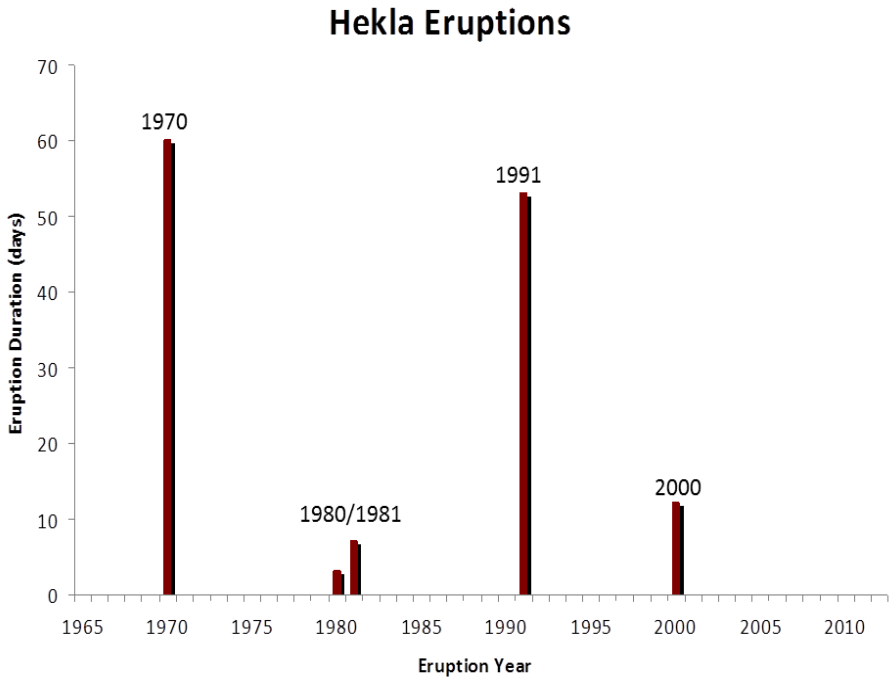

Figure 1.3. The decadal eruptions of Hekla and their durations. Another decadal eruption is three years overdue (Höskuldsson et al., 2007; Grönvold et al., 1983; Gudmundsson et al., 1992; Thorarinsson and Sigvaldason, 1972).

Table 1.1. Summary of estimates for magma chamber and dike at Hekla from selected studies.

Eruption	Method	Depth (km)	Location of center (if given)	Dike (if modeled)	Reference
1980	EDM (electronic distance measurements)	7 to 8	Below summit		Gronvold et al., 1983
1991	GPS	2 to 15			Sigmundsson et al., 1992
1991	Borehole strain meter	over ~4-5	Under summit	Connected to chamber, 4 x 4 km, 85 cm opening	Linde et al., 1993
1970-1977 repose	Optical levelling tilt	5 to 7	NW		Tryggvason, 1994
1987-1990 repose	Optical levelling tilt	5 to 6	1 to 2 km NW Litla Hekla		Tryggvason, 1994
1991	Optical levelling tilt	5.0-6.2	4-6 km NNW Hekla Summit		Tryggvason, 1994
2000	Seismic	over 14			Soosalu and Einarsson, 2003
1991	Strain meter	11^			Sturkell et al., 2006
2000	InSAR	14 to 18 km	SE	6.6 x 5.8 km, 70-73°SE dip, 18-23 cm opening, 23-31 left-later strike-slip	Ofeigsson et al., 2011
post-2000 repose	GPS	22-29*			Geirsson et al., 2012
2000	GPS, strain meter	<10 km	Under summit	6.6 x .35 km, 1.6 m opening	Sturkell et al., 2013

^reported as a personal com with Kristján Áugústsson. This estimate is a correction to the Linde estimate based on new information about the borehole data.
* This study investiaged several possible source geometries. The result reported here is for spherical source

lateral strike-slip motion. The most recent findings (Sturkell et al., 2013) use GPS and strain meter data in inversions of an HEHS model with the magma chamber and dike in a single model to estimate a dike, which is not connected to the chamber, with a best-fit geometry of 6.6 km length, 0.35 km width, and 1.6 m of opening and a N60°E strike.

Borehole strain measurements and tilt meter data (Figure 1.4) reveal a cyclic pattern of deformation, consisting of steady inflation before an eruption, followed by co-eruption dike formation and rapid deflation (Tryggvason, 1994; Ofeigsson et al., 2011; Geirsson et al., 2012; Sturkell et al., 2013). In contrast to the steady deformation measured by tiltmeters, Hekla is seismically quiet between eruptions. Seismic activity did not begin until a half hour before the 1991 eruption (Gudmundsson et al., 1992; Linde et al., 1993) and not until roughly 80 minutes before the 2000 eruption (Soosalu et al., 2005; Höskuldsson et al., 2007). By the end of the 2000 eruption, a total of 0.189 km^3 dense rock equivalent (DRE) of basaltic andesite magma had been emitted through an eruptive fissure, which split into five segments totaling 6.6 km in length (Höskuldsson et al.,

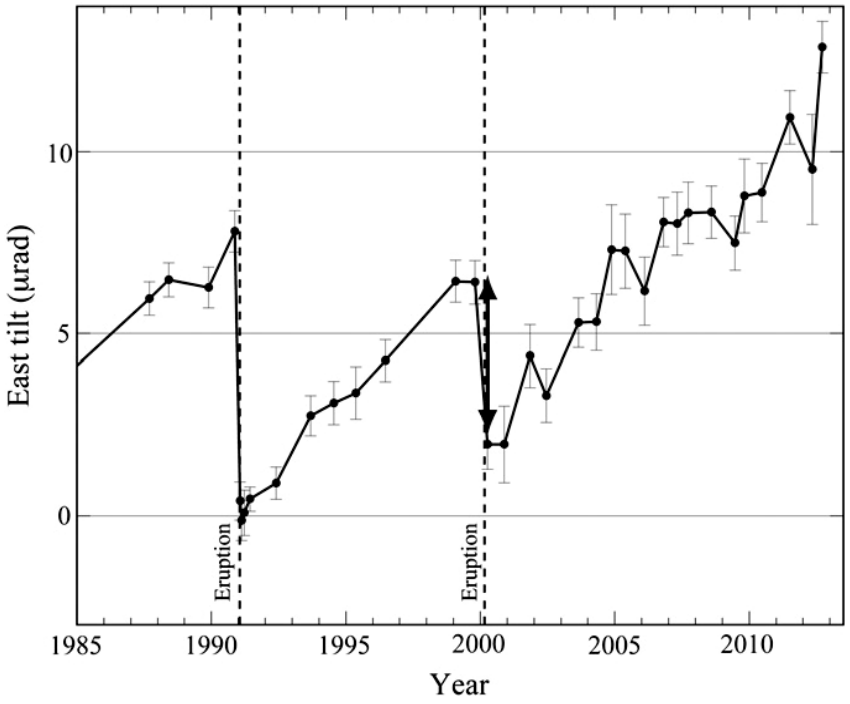

Figure 1.4. Tiltmeter data from Hekla spanning 1985-2012. The cyclic pattern includes rapid tilt changes due to eruptions. Tilt levels as of 2012 are greater than before the 2000 eruption (Sturkell et al., 2013).

2007; Ofeigsson et al., 2011). The segments activated first at the highest altitude and then down to the lowest, with the lower altitude segments continuing activity throughout the eruption (Höskuldsson et al., 2007). Hekla has been steadily inflating since the February-March eruption in 2000 (Ofeigsson et al., 2011; Geirsson et al., 2012; Sturkell et al., 2013), and tilt levels measured through 2012 (Figure 1.4) surpass those attained just prior to the 2000 eruption. These data and the relatively recent decadal eruption rate indicate this volcano could be ripe for another event.

GEODETIC MODELING

1. General History

Dikes feed eruptions, and understanding how dikes propagate and behave is fundamental in understanding how magma moves through and is extruded from volcanoes (Acocella and Neri, 2009). Such knowledge is crucial to the development of forward models of volcanoes and may eventually lead to better eruption forecasts. Models of dike behavior treat dikes as fractures and are typically discussed in one of two contexts: applied stress (pressure) or prescribed strain (displacement). While studies discussing fracture mechanics in terms of stress are thought by some (e.g. Fukushima et al., 2010; Anderson and Segall, 2011) to be more accurate reflections of the modeled system, applying prescribed displacements to the system accomplishes the same goal because stress and strain are conjugate variables in the 3-D governing equations for displacement in a static elastic medium:

$$G\nabla^2 u_1 + \frac{G}{1-2v}\left[\frac{\partial^2 u_1}{\partial x^2} + \frac{\partial^2 u_2}{\partial x \partial y} + \frac{\partial^2 u_3}{\partial x \partial z}\right] = -F_x$$
$$G\nabla^2 u_2 + \frac{G}{1-2v}\left[\frac{\partial^2 u_1}{\partial y \partial x} + \frac{\partial^2 u_2}{\partial y^2} + \frac{\partial^2 u_3}{\partial y \partial z}\right] = -F_y \qquad 1.1$$

$$G\nabla^2 u_3 + \frac{G}{1-2v}\left[\frac{\partial^2 u_1}{\partial z \partial x} + \frac{\partial^2 u_2}{\partial z \partial y} + \frac{\partial^2 u_3}{\partial z^2}\right] = -F_z$$

where G is the shear modulus, displacements in the x, y, and z directions are designated by u_1, u_2, and u_3, respectively, v is the Poisson's ratio, and F_x, F_y, and F_z are the body forces per bulk volume (Wang, 2000). Elastic strain (ε) is a function of the change in displacement and stress (σ) shown by:

$$\begin{aligned}
\varepsilon_{xx} &= \frac{\partial u_1}{\partial x} = c_1\sigma_{xx} + c_2\sigma_{yy} + c_3\sigma_{zz} \\
\varepsilon_{yy} &= \frac{\partial u_2}{\partial y} = c_4\sigma_{xx} + c_5\sigma_{yy} + c_6\sigma_{zz} \\
\varepsilon_{zz} &= \frac{\partial u_3}{\partial z} = c_7\sigma_{xx} + c_8\sigma_{yy} + c_9\sigma_{zz} \\
\varepsilon_{xy} &= \frac{1}{2}\left(\frac{\partial u_1}{\partial y} + \frac{\partial u_2}{\partial x}\right) = c_{10}\sigma_{xy} \\
\varepsilon_{xz} &= \frac{1}{2}\left(\frac{\partial u_1}{\partial z} + \frac{\partial u_3}{\partial x}\right) = c_{11}\sigma_{xz} \\
\varepsilon_{yz} &= \frac{1}{2}\left(\frac{\partial u_2}{\partial z} + \frac{\partial u_3}{\partial y}\right) = c_{12}\sigma_{yz}
\end{aligned} \qquad 1.2$$

where $c_{1\text{-}12}$ are constants (Wang, 2000). Analytical solutions that satisfy 1.1 for an elastic dislocation embedded in an HEHS are widely used to simulate surface parallel (e.g., fault slip) and surface normal (dike/sill opening) dislocations (Okada, 1992), the latter of which is used to study dike movement.

Inversions for magma plumbing parameters from geodetic data (e.g., InSAR) utilize a variety of methods to best represent the system being modeled. Relatively simple analytical solutions are commonly used because they provide fast, exact, and computationally inexpensive results. These analytical solutions (e.g. Okada; equation 1.1) simulate expansion of dikes as

elastic dislocations of rectangular surfaces (Figure 1.5) embedded in a homogeneous, elastic half-space (HEHS). The assumptions fundamental to the analytical solutions oversimplify the deformation system of a volcano. By utilizing these assumptions, the modeler implies the material properties of a volcano are elastic, do not vary in space, and that the (stress-free) land surface is flat. Previous studies (e.g. Masterlark et al. 2010, 2012; Williams and Wadge 1998, 2000) have shown that half-space model assumptions can strongly bias both source parameter estimates determined with inverse models and forward model predictions for deformation and stress.

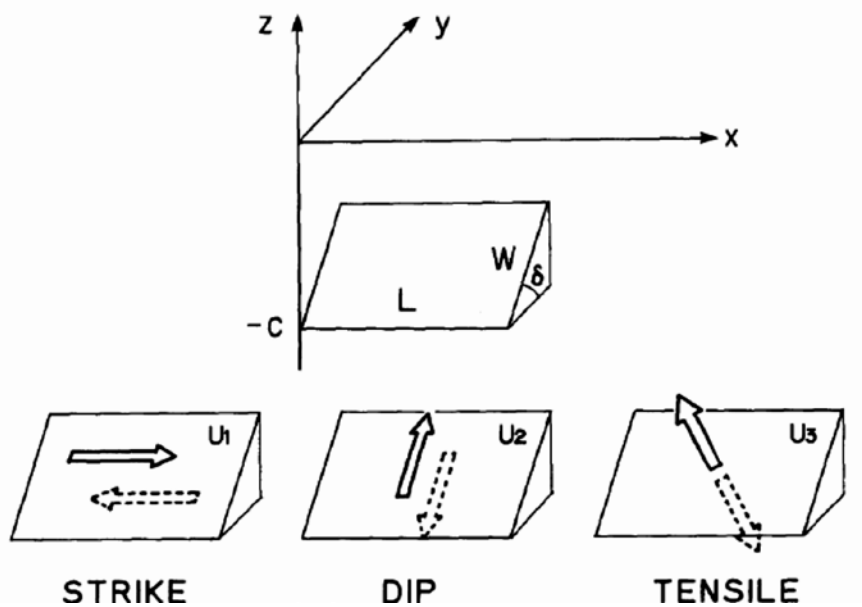

Figure 1.5. Geometry and conventions of the model space (Okada, 1992). The x axis is along-strike, i.e. the length of the dike, L. The y axis corresponds to the width of the dike, W. The z axis is perpendicular to the fault plane, and δ is the angle between the fault plane and the land surface. The point below the surface of the earth at which the calculation point would intersect is –C. U_1 is deformation in the x direction, along strike. U_2 is deformation in the y direction, along the dip, and U_3 is the deformation in the z direction caused by tension.

In spite of the limitations, HEHS models of volcanoes, with corrections for topography, have been utilized effectively to account for deformation caused by fissure movement. Williams and Wadge (1998, 2000) found that topography, in some cases, may have more of an influence on deformation predictions than other source parameters and suggest a series expansion of an elastic half-space solution with small slope approximations to correct for topography. They use a

finite element model (FEM), which splits the model domain into smaller parts with potential for individual unique property definitions, for validation. Ofeigsson et al. (2011) use the topographic correction from Williams and Wadge (2000) on a HEHS model of the fissure movement on Hekla volcano. Fukushima et al. (2010) utilized a combination Boundary Element Method (BEM), which solves for a set of linear partial differential equations set up as integrals, and a Monte Carlo inversion algorithm which simulated a model domain with topography in their study of the evolution of magma conduits at Piton de la Fournaise volcano on Réunion Island. These are just two examples of studies that include corrections for topography in their models. Models of Hekla need to include topography because Hekla's relief is significant (1.45 km), and the strike of Hekla's eruptive fissure does not line up with the general trend of other faults and dikes in the area, indicating a local feature (e.g. the volcanic edifice) may be affecting the strike of the eruptive fissure and dike at depth.

The material property assumptions to HEHS models call for homogeneous property definitions in the model domain, but observed material variations at volcanoes invalidate this assumption (e.g. Masterlark et al., 2007, 2010; Haney et al., 2011). Generalized material properties of rocks can be extracted from various compilations of lab and field studies for use in model design (e.g.Turcotte and Schubert, 2002; Christensen and Mooney, 1995; Christensen, 1996; Wang, 2000). It is favorable, however, to have precise, in situ estimates based on local material properties because those properties will have direct influence on deformation predictions (equation 1.1). Results from Heap et al. (2009) suggest the "average" crustal model may over-estimate the Young's modulus and under-estimate the Poisson's ratio of basalts which have undergone repeated stress cycles from volcanoes. The repeated stressing leads to anisotropic deformation, increasing the level of crack damage (Heap et al., 2009). Models which

do not take these effects into account may assume higher material strength. Reliable estimates of mechanical properties and their behavior under stress are crucial to accurately model ground deformation data (Heap et al., 2009). A viable improvement on the HEHS model is to utilize layers of different material properties and create a layered elastic half-space model (LEHS) using observed material properties (Roth, 1990). A further improvement is a model which allows unique property definitions throughout a model domain which can have complicated geometry representing topography, rather that the simple geometry and homogeneity of a HEHS.

2. Finite Element Models

FEMs allow geometric and material variations not possible with other modeling techniques by splitting the model domain into an assembly of finite elements with potential for individual, unique property definitions of each element. This piecewise construction allows for arbitrary geometric configurations of the domain while satisfying the governing equations (equation 1.1) for the case of having heterogeneous and/or anisotropic material properties. The FEM method for elastic models in Abaqus (http://www.simulia.com) includes a piecewise force balance that simultaneously integrates the partial differentials to minimize the principle of virtual work over the entire domain.

Simple, first order topographic corrections are not applicable to all models of dikes, and the corrections which are applicable do not allow the dike to intersect the surface; the dike must begin at sea level regardless of the topography. FEMs permit modeling of a dike which intersects the surface, even if that surface is 1.5 km above sea level. The most recent model of the Hekla dike (Sturkell et al., 2013) utilizes a combination Okada-Mogi model with no topographic corrections to estimate source parameters for the inferred deep-seated magma chamber and dike

in a single model. Results indicate the dike cannot be more than 0.5 km wide, with a 0.35 km wide dike being the favored option. Such a width, when taken from the surface of Hekla (approximately 1.45 km above sea level) would place the entire dike above sea level. This geometry is poorly represented without including topography in the model domain, but results from Sturkell et al. (2013) indicate it is a geometry which deserves exploring. Another example is the study at Piton de la Fournaise volcano, which rises more than 2.6 km over Reunion Island. Fukushima et al. (2010) utilized multiple dike geometries in their attempt to fit the InSAR deformation data from several successive eruptions of Piton de la Fournaise in the late 1990's in an effort to track conduit evolution. As mentioned before, they used a boundary element method, which allowed them to embed a topographic mesh in their models, and their preferred dike models all had dike bottoms about 1.3 km above sea level (i.e. half the topography of the volcano). In other words, the best-fit geometry for this volcano includes a dike that doesn't reach sea level. Some best-fit models also included dikes which are curved, and this is yet another geometry HEHS models cannot simulate well. Their models could not account for observed and calculated differences in rock properties, however, and this was cited as a main reason some of their models could not fully explain the data. These examples illustrate the importance of being able to include both topography and rock heterogeneity (such as layering) in a volcanic model.

FEMs have generally been avoided due to the computational intensity required for meshing the model and computation time for the FEM solution (Fukushima et al., 2010; Grapenthin et al., 2010; Ofeigsson et al., 2011; Williams and Wadge, 2000). Computational power, however, has drastically increased in the past decade. As such, FEMs of volcanoes are no longer the computational burden they once were. Model domain meshes accurately representing topography can be readily generated by converting topographic data from a point cloud

representation into a surface object that defines the free (land) surface of a 3-D domain using standard CAD software. This, in turn, can be used in an FEM domain that satisfies equation 1.1. Assigning different parts of the FEM unique property definitions is an easy process, but the time it can take to implement is directly related to the complexity of the rock properties. In these models, the addition of layering increased the time it took to build the model by a few minutes. Simulations of fissure movement in an elastic domain spanning thousands of cubic kilometers and meshed with hundreds of thousands of elements and nodes can be calculated in minutes on workstations having multi-core processors and physical memory that is sufficient to keep the entire problem in core.

PROJECT SUMMARY

This dissertation investigates the influence of an irregular topographic free surface as part of the elastic model domain and the influence of a layered distribution of rock properties in FEMs of deformation triggered by kinematic loading along Hekla's dike during the 2000 eruption. The significance of this study lies in the ability to generate models of conduit behavior during a volcanic eruption. Magma moves to the surface during an eruption through either a fissure (dike) or volcanic vent (pipe). These conduits are the link between the magma chamber and the surface. As such, they feed eruptions, so understanding their geometry and how they behave during an eruption is a key element to understanding their overall role in the magmatic plumbing system of active volcanoes. The findings of this study may guide researchers in designing optimal model configurations to use in inversions of dike geometry parameters. Such parameters are absolutely essential before dike behavior can be precisely estimated.

The first FEM of this study investigates the influence of topography independent of the influence of realistic layering in rock properties. New issues generated by including topography in the model domain, such as the initial origin for the top of the dike, are investigated by varying the starting elevation of two dikes between sea level and the summit of the volcano. The two dikes are unique in their widths (i.e. down-dip length): one has a 5.8 km width and the other has a 0.35 km width. These widths are from the best-fit geometry of two different estimates for the dike at Hekla (Ofeigsson et al., 2011; Sturkell et al., 2013). By varying the starting elevation of the different dikes, the relationship between the (stress) free surface and dike can be elucidated, which is not something that can be explored using commonly employed topographic corrections (e.g. Williams and Wadge, 1998, 2000). Also, placing the top of the 0.35 km dike at the summit of Hekla will cause the dike to be totally encased in the volcano because it does not extend far enough down to intersect sea level. This is something that has never been explored at Hekla, but it deserves investigation because this width is the best-fit geometry from the most recent study at Hekla (Sturkell et al., 2013), which had a more dense network of local deformation data near the dike, but it did not use any topographic corrections in the model domain.

The second model investigates the relationship between rock property layering and dike width independent of topography by varying the thickness of the top layer from 1 km to 0.5 km using the same two dike widths as the first model. The 5.8 km wide dike will pass through all layers of the model, regardless of the top layer configuration, while the 0.35 km wide dike will be contained entirely within the first layer. There are two configurations for the layers. In one configuration, the layers each have a thickness of 1 km, but in the other, the top layer is split into two 0.5 km layers. Properties of the layers are determined from the shear-wave velocity profile from Haney et al. (2011) taken 15 km southeast of the volcano. These configurations have

implications for how dikes and faults are loaded in models, and how layering of rock properties, especially near the surface, might or might not affect those loading parameters.

The third type of FEM configuration for this study includes topography and layering into a single model domain. This model explores the complex relationship between topography, rock property layers, and dike widths. Six configurations are explored and comparisons of the predictions to the other types of FEM configurations demonstrate the effect rock property layering and dike width have in a model domain with topography. Although sparse data coverage near the dike cannot be ignored, the results of this study emphasize the need for further exploration of this technique, with a much more dense data network near the dike; such an exploration could provide better insights into volcanic processes.

Models are simplifications of a natural system, and an accurate model enables the modeler to quantitatively understand mechanical and geological processes. Such an understanding is a key requirement for eruption forecasts. There is a trade-off, however, between accuracy of the model and computation time, as well as accuracy of the model and the process modelers seek to understand. Thus, modelers always seek the ideal balance between a model that accurately portrays the process they seek to understand which can be quickly analyzed without sacrificing quality in the results. These models highlight short-comings in current techniques (i.e. accurate portrayal of a real system) but also in the technique utilized in this study. The time it takes to compile and analyze these models has decreased drastically in the last decade as advances in computing continue to race forward. FEMs, however, still take considerably longer to build and analyze than the simpler HEHS models, and analyses seeking to constrain non-linear parameters such as dike geometry would still be quite time consuming. Automation and optimization of the techniques related to both FEM design and implementation would greatly

advance the feasibility of these models in such analyses. The findings of this study may guide researchers in designing optimal model configurations which to use in inversions of dike geometry parameters. Such parameters are absolutely essential before dike behavior can be precisely estimated.

Some major innovations of this study include: (1) investigation of how the relationship of the upper boundary of a dike (i.e. the fissure) to the (stress) free surface of a model can affect model predictions, (2) modeling a dike in Hekla which never reaches sea level but intersects the surface,(3) modeling the behavior of the Hekla dike in a domain with locally constrained rock properties, and (4) incorporating topography with local layering of rock properties into a single model domain of a 3-D FEM simulating the behavior of the dike during the eruption.

CHAPTER 2

DEFORMATION MODELING PROTOCOL

INTRODUCTION

The ability of a model to efficiently and accurately represent a natural system directly impacts the results and usefulness of the model. I follow a formal modeling protocol (Hughes and Masterlark, 2008; Hughes, 2011) to ensure the models of Hekla simulate the natural system in the most efficient, accurate, and reproducible way possible (Figure 2.1). The protocol is iterative; every step leads to the next step or re-evaluation and modification of the model. The subsequent sections discuss each step of the modeling protocol in detail and include a general summary and application of the concept to each type of model.

DEFINE PURPOSE

The purpose of the model drives the entire modeling process and must, therefore, be explicitly defined. My study examines the effects of deformation model characteristics such as rock property layering and topography using InSAR data from the 2000 eruption of Hekla volcano in Iceland by isolating those characteristics in numerical inversions. I build three models: the first model implements the topographic surface directly in a model domain with homogeneous properties, the second model includes layering of the local rock properties, and the third model combines topography and rock

property layers, which is unprecedented at Hekla. My results indicate the current limits to our ability to reconstruct the observed deformation field may be related to the limits which have previously been placed on the commonly used models simulating deformation processes. The models built for this study are "state of the art" move beyond those limits. The study furthermore provides an investigation of trade-offs between the various model complexities considered. These specific models apply only to Hekla, but the process for building them can be used to propel volcanic modeling out of the HEHS and into the 3-D domains available with FEMs and the computing power of the modern world.

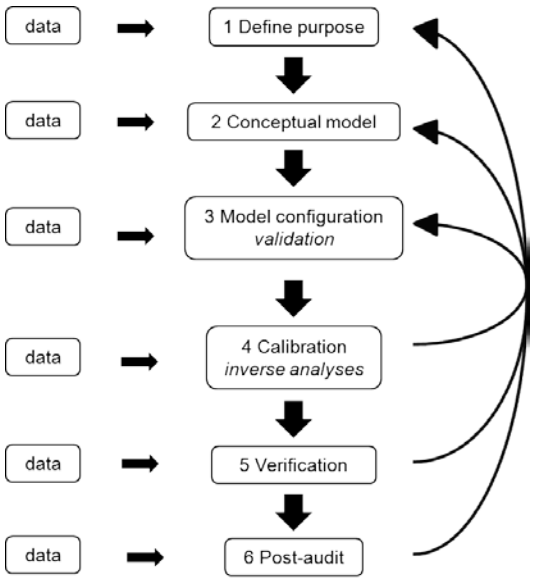

Figure 2.1. Iterative modeling protocol utilized in this study after Masterlark and Hughes (2008).

CONCEPTUAL MODEL

The conceptual model is the general design of the model, and its implications propagate throughout the modeling protocol (Masterlark and Hughes, 2008). Inaccurate inputs to the model create unreliable predictions, which can have dangerous implications regarding analysis of stress regimes, subsequent deformations (Hughes, 2011), and ultimately, interpretations of fissure generation during eruptions, which can bias eruption forecasts. There are an overwhelming amount of physical processes that affect dike propagation in nature, and any computer model simulating these events has to ignore or simplify some of the processes (Buck et al., 2006). The following paragraphs explain different assumptions made to the conceptualization of Hekla volcano and how they may affect model results.

The conceptualization of Hekla's feeding dike during the 2000 eruption relates ground deformation captured by two satellite radar passes, which encompass the event as an InSAR image, to the movement generated by the dike and fissure formation during the eruption in a three dimensional elastic problem domain. The InSAR data include other signals besides just the deformation relating to the dike movement. These signals are accounted for in methods described under the Calibration: InSAR Data and Preparation section below.

The deformation is assumed to be static and independent of time (equation 1.1), meaning the deformation remains after the formation of the dike. The assumption is placed on the model to constrain the problem to one which addresses how topography and layered rock properties affect model results. If the assumption of static and time-independent deformation is removed, either governing equations that describe transient process or transient loading functions that describe how the Hekla system deforms through time would have to be implemented. Quantifying such a relationship goes beyond the scope of this project, and is unrelated, as the topic of this project is the overall net (incremental) deformation.

The feeding dike of the volcano is represented as a plane with uniform prescribed relative displacement through a deformable surface, embedded in a three dimensional model domain. Although uniform displacement along the dike may be geologically unrealistic, it is used in these models to provide an initial starting point in the modeling process. Distributed displacement, by which a fissure or fault is split into many individual and unique patches that can move relatively independently from one another, can provide further insight into fissure and fault behavior. In simplified HEHS models of fissure movement, splitting a fault into many different independent patches is a relatively simple matter which impacts computation time in a trivial manner compared to the impact such a change has on an FEM. For the latter, splitting the fault into

multiple patches in a FEM requires a separate forward model for each patch while the other patches are held fixed. Computation time is thus increased by a factor of the number of patches. For example, splitting the fissure into two patches doubles computation time because two FEMs must be analyzed. This study lays the groundwork, however, for designing models which could utilize multi-patch concepts, and these models should be explored in future work.

Far-field lateral and depth boundaries of the problem domain are zero displacement and initial conditions are equilibrium. As mentioned earlier, the regional geology and tectonics play a significant role in the Hekla system, and Hekla is not isolated from these effects (e.g. Gronvöld et al., 1983; Soosalu and Einarsson, 1997, 2005; Sturkell et al., 2013). The manner in which these background stresses affect the behavior of the fissure at Hekla during any given eruption, however, is an entirely separate study within itself and beyond the scope of this project to investigate. In the temporal and geographic context of this study, the scale of strain caused by the background stresses (such as the 19 mm/yr of rifting distributed mostly throughout the western EVZ; Geirsson et al., 2012; Jónsson et al, 1997; Sigmundsson et al., 1995), is small compared to both the scale of strain caused by the dike during the eruption and by the scale of deformation InSAR can detect. Therefore, they are assumed to be negligible. Deformation signals which can affect the inversions are discussed in the Calibration: InSAR Data and Preparation section.

MODEL CONFIGURATION

The model is configured to simulate and quantify the processes and relationship of the conceptual model (Hughes, 2011). The FEMs for this study are constructed in Abaqus and satisfy the general elastic governing equations (equation 1.1) over the 3-D problem domain for a given set of boundary conditions, loading specifications, and initial conditions. The model

domain is horizontally 90 km by 90 km with 25 km vertical depth (Figure 2.2). These lateral dimensions are used because they are the closest the model boundaries can be to the dike without the boundaries impacting model results. Details regarding this are discussed in the Validation section. The vertical boundary is based on estimates of the crustal thickness under Hekla (Darbyshire et al., 2000; Kaban et al., 2002) and is also the minimum distance required to not affect model results.

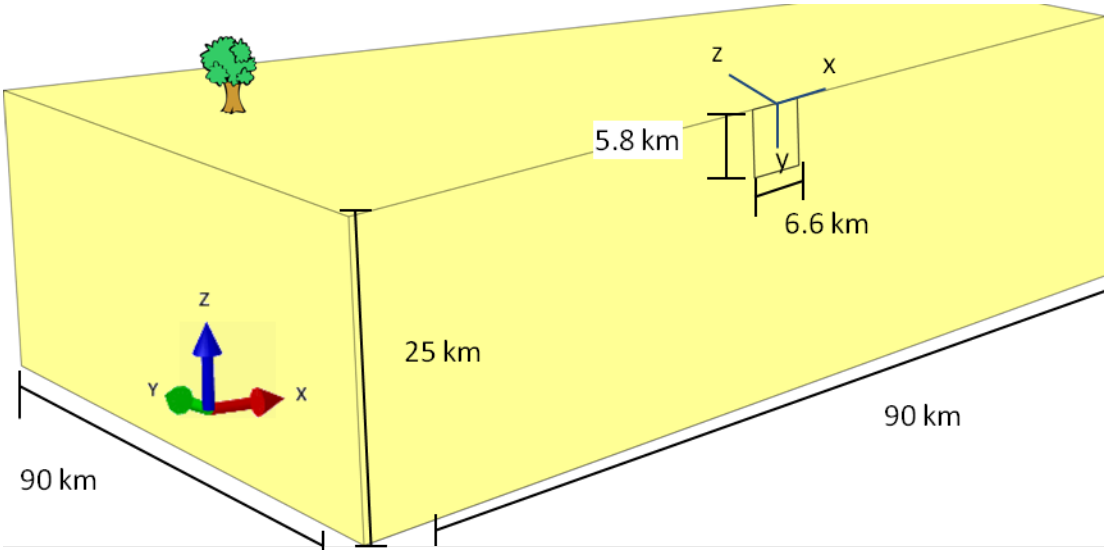

Figure 2.2. Cross-section view of the HEHS model of the 5.8 km width dike at Hekla, cut along the dike. The top of the model is a (stress) free surface located at sea level, and the model is the same color throughout, indicating homogenous material properties. Poisson's ratio is ν=0.25, and Young's modulus is 30 GPa (Grapenthin et al., 2010, Ofeigsson et al., 2011). The dike is 5.8 km deep and 6.6 km long (along strike), and the dike axis system is displayed as blue lines centered on the origin of the model domain. The model domain is 90 km by 90 km by 25 km, with x, y, and z conventions displayed on lower left corner. Tree indicates land surface and is not to scale.

The top surface of the model is the land (stress-free) surface, and the bottom of the problem domain represents the bottom of the elastic crust. The elastic crust under Hekla is represented by a material with a Poisson's ratio of ν=0.25 (Grapenthin et al., 2010; Ofeigsson et al., 2011) and a uniform Young's modulus of 30 GPa (Ofeigsson et al., 2011). Many studies have investigated the thickness of the elastic crust under Iceland and near Hekla. Some find that portions of the middle and deeper crust behave visco-elastically (e.g. Darbyshire et al., 2000;

Grapenthin et al., 2010; Kaban et al., 2002; Ofeigsson et al., 2011). The nature of the crust under Hekla is a key factor in the behavior of these models, but investigating visco-elastic responses to fissure loading at Hekla is beyond the scope of this project, which focuses on elastic behavior that is appropriate for the relatively short time interval spanned by the InSAR data. Previous models investigating Hekla's fissure use HEHS assumptions (Linde et al., 1993; Ofeigsson et al., 2011; Sturkell et al., 2013). The current study investigates two specific alterations to those assumptions, but departures from the elastic rheologic behavior of the crust is not an assumption that is investigated here.

The dike is modeled as a vertical (i.e. 90° dip) 6.6 km long plane with two different widths (i.e. down-dip length) of 5.8 km and 0.35 km. The length is determined by the surface expression of the eruptive fissure (as mapped by Höskuldsson et al., 2007), and the two widths correspond to the most recent estimates of the dike geometry at Hekla (Ofeigsson et al., 2011; Sturkell et al., 2013). The dike is modeled as a tensile fault with strike-slip movement embedded at the top, near the center of the domain. It is created in Abaqus by sketching a vertical partition with the dimensions of the dike into the model domain. A partition is a part of the model which can be assigned different boundary and initial conditions, interactions, and properties from other parts of the model. The partition created for the dike is assigned as a seam and seeded differently for the model mesh than other parts of the model. The elastic dislocation for the two sides of the fissure is implemented using the method of 3-D kinematic constraint equations developed by Masterlark (2003). The precise location of the top of the dike varies for models involving topography, and details regarding that will be given in the Topography section. The origin of the model is sea level at the coordinates of the center of the dike plane: E 565235.25 m and N

7096685 m UTM zone 27N WGS 1984. This is done to provide a cohesive reference point throughout the models, regardless of the free-surface geometry.

The fineness of the mesh (i.e. network of elements) is directly related to the influence a specific location has on the results. The dike is the key geometric entity of the deformation model. Likewise, displacement gradients are anticipated to be greatest near the fissure. Accordingly, the mesh along the dike is extremely fine compared to the mesh along the boundaries, where deformation gradients vanish (Figure 2.3). Validation provides constraints on

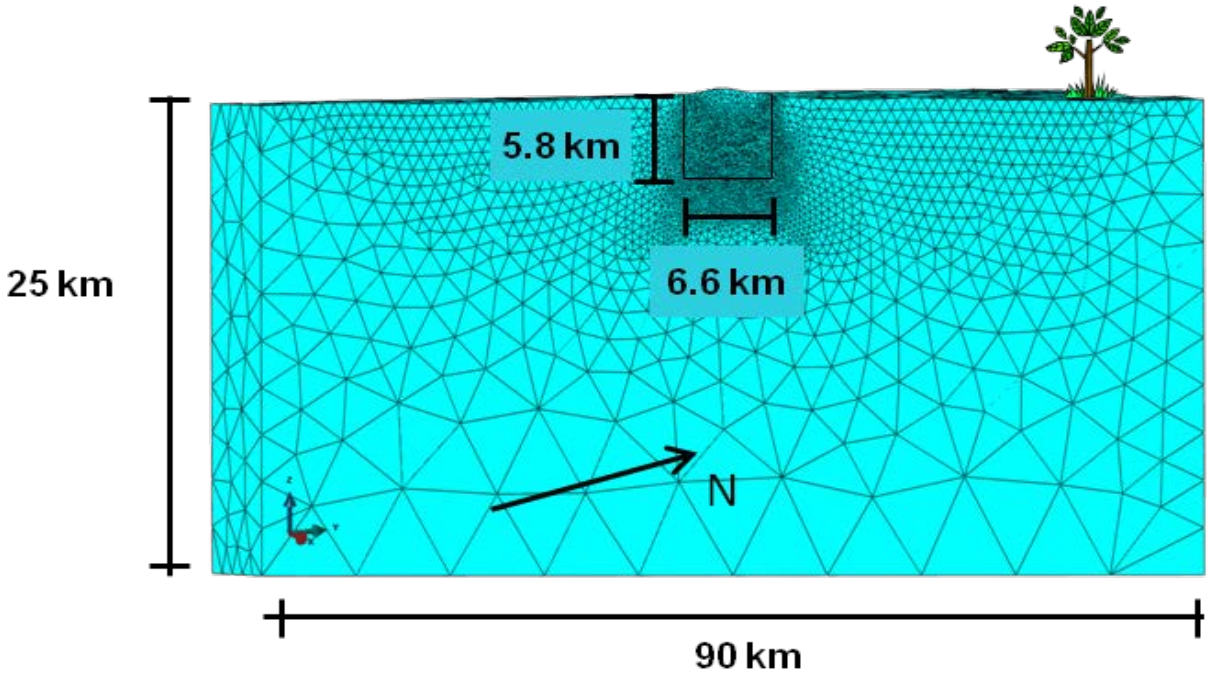

Figure 2.3. Example of a cross-section (cut along the dike) model domain representation for Hekla, showing the mesh and its relationship to the dike. The mesh is much finer near the dike and coarser at the boundaries. This particular model has a (stress) free surface representing topography and homogeneous rock properties, as indicated by the model domain having the same color throughout. Tree indicates land surface and is not to scale.

the size of the elements and fineness of the mesh. It is necessary to have a mesh which is fine enough to capture the deformation effectively but not so fine as to cause unnecessarily long calculation times. The dike has elements seeded at 40 m intervals along its top, 45 m along the sides, and 50 m along the bottom. The mesh along the outer model boundaries is much coarser,

with element seeds every 5,000 m along the top. Seeds along the sides increase in size downward from 7,500 m at the top to 10,000 m at the bottom of the sides. Seeds along the bottom edges of the problem domain are spaced 10,000 m apart. The number of elements created with this seeding profile is anywhere from 200,000 to nearly 2 million depending on the model configuration.

As mentioned previously, the dike geometry is modeled as a seam in Abaqus, meaning overlapping duplicate nodes are placed along the partition, allowing an originally closed face (the fissure) to open during the analysis. The geologic implications of an open versus closed fissure before the eruption are not trivial. One implies a constantly open crack which may or may not still have remnants of melt within the conduit itself, while the other indicates a completely closed off (i.e. cooled off) conduit which is opened or cleared during the eruption. The modeling implications of an open vs. closed dike, however, are logistical and have little impact on predictions.

The elastic dislocation along the dike is implemented using the method of kinematic constraint equations (Figure 2.4), where prescribed relative slip in the local z direction (opening) and local x direction (strike-slip) are applied to the dike via a system of internal boundary conditions (Masterlark, 2003). The prescribed relative displacement is the same along the entire length and width of the dike. For computational convenience, the nodes have a local right-handed coordinate system corresponding to along strike, updip, and fault-normal directions (Figure 2.2).

1. Topographic FEM Configuration

The data used to create the topographic surface for the two model configurations with topography are SRTM data surrounding a 10,000 km^2 area around the fissure center. The deformable topographic surface is created for direct import as a .sat file utilizing the meshing techniques available in the Rhinoceros (Rhino) software (www.rhino3d.com/). The data are imported to Rhino as a point cloud and meshed using the Mesh from Points tool, which creates a mesh of triangles and quadrilaterals (www.rhino3d.com/). A surface is draped over this mesh using the Drape Surface Over Objects tool, and the surface is rendered. The surface is exported as a .sat file, which is then imported as a part in Abaqus. Due to rendering issues, the surface cannot be welded or otherwise combined with a cubic model domain in Abaqus. Instead, the topographic surface is used to cut a negative of the surface onto a different cube, which is

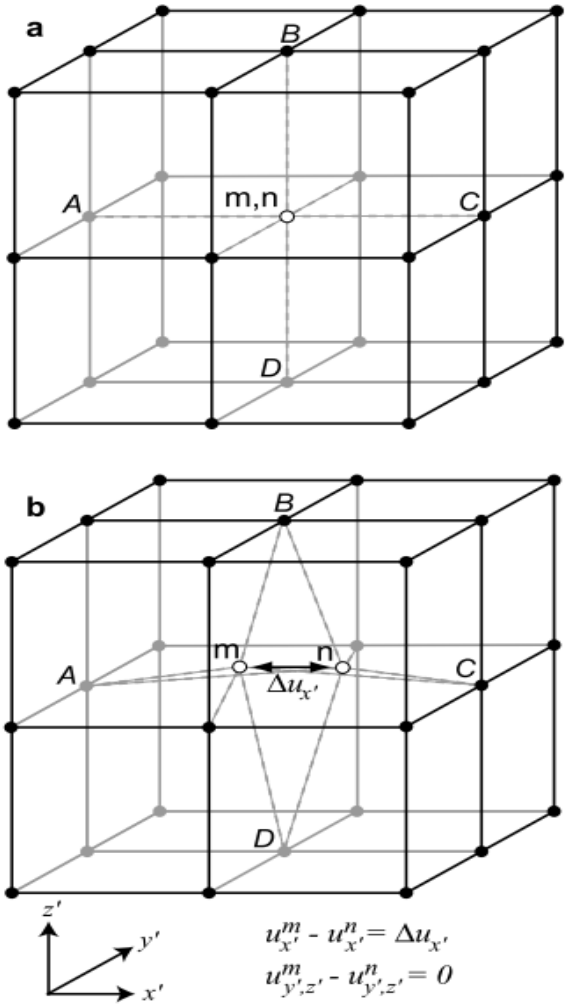

Figure 2.4 Dislocation and kinematic equations of a node-pair from Masterlark (2003). (a) Example FEM mesh includes collocated nodes *m* and *n* on dike ABCD. (b) The static dislocation effected by applying the kinematic constraint equations shown at the bottom. The dislocation vector $\Delta u_{x'}$ is parallel to x' (strike-slip). Likewise, dislocation vectors $\Delta u_{y'}$ and $\Delta u_{z'}$ are parallel to y' (dip-slip) and z' (opening). Dike ABCD is a deformable surface because three-dimensional translation of all three dislocation vectors is allowed.

then used to cut a positive form of the topography on top of the otherwise cube-shaped problem domain. Aside from the topographic surface, the configuration of topographic FEM is essentially the same as discussed earlier, with an important exception: the dike surface area.

An irregular free surface necessarily changes the geometry of the dike where it intersects the surface, thus altering the surface area and areal plane of the dike. A HEHS model permits square dike geometry even though the dike intersects the surface at the mapped fissure location, but a topographic surface does not. Three FEMs with different dike width references are explored for two dike widths: one 5.8 km and one 0.35 km, giving a total of six models for analyses. A HEHS model of a 5.8 km wide dike is utilized as a control for the topographic FEM of a dike with the same width to demonstrate the effect topography has on deformation predictions. The 0.35 km dike in the topographic FEM is compared with the 5.8 km width dike to investigate the effect topography can have on dike induced deformation relative to the width of the dike.

Table 2.1 explains the naming convention for the different models. The name of each model begins with capitalized letter indicating that the model is the HEHS model, or a specific type of FEM. The next letter is a lowercase letter indicating the reference point for the fissure width; either sea level or the topographic surface. The first number in the name is related to the reference dike width. Dikes in FEMs which use the topographic surface as a reference point will have smaller actual widths because they will begin 1.45 km above sea level and extend down the value of their width. Dikes which intersect the topographic surface in the FEMs with topography and extend to their width values below sea level will have bigger actual widths because of the extra 1.45 km from Hekla's topography. Models with layering are discussed in the next section, but if layering is present in the model, the name will have a second number related to the

Table 2.1. Naming convention for the models

Heirarchy	Symbol	Meaning
Type of model	H	HEHS MODEL
	T	FEM WITH TOPOGRPAHY
	L	FEM WITH LAYERING
	LT	FEM WITH LAYERING AND TOPOGRAPHY
Reference point of the "depth" of the model	s	Sea-level
	t	Topographic surface
Dike width	5	5.8 km wide
	3	0.35 km wide
Layering (only if present in the model; homogeneous models will have no second number)	1	First layer is 1 km thick
	2	First two layers are 0.5 km thick
Blind or not	b	Blind
		Fissure intersects the surface if there is no 'b'
Example: The layered topographic FEM with a dike that extends down to 5.8 km below sea level and a top layer 0.5 km thick and is LTs-5.2. The same model, but one in which the fissure extends 5.8 km below the topographic surface is LTt-5.2		

layering used in the model. If a fissure is "blind" (i.e. does not intersect the surface) then the model name will be followed by a 'b'. In blind models, the reference elevation is always sea level.

In the first topographic FEM configuration, the dike begins at the top of Hekla and extend down to the equivalent dike width below sea level. In other words, the topographic FEM of the 5.8 km dike models a dike which extends from the top of Hekla to 5.8 km below sea level for a total dike width of 7.25 km. This model is called Ts-5, because it is the topographic FEM with a sea level reference for the 5.8 km wide dike. The topographic FEM of the 0.35 km wide dike which extends from the top of Hekla down to 0.35 km below sea level is called Ts-3 (Figures 2.5-2.6). These models have a greater dike surface area than their equivalent dike widths in the

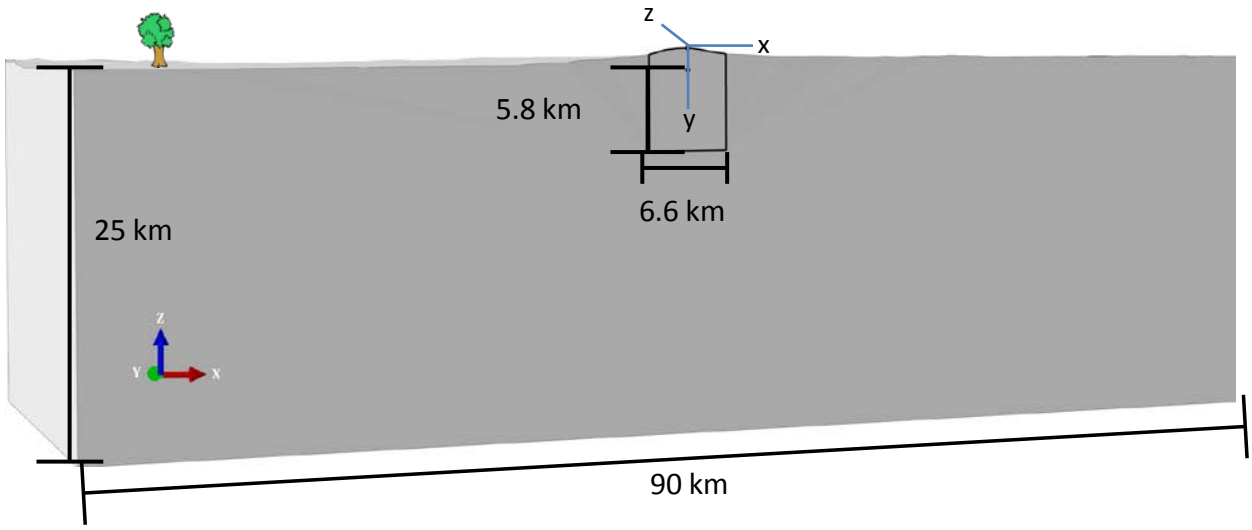

Figure 2.5. Cross-section view of model Ts-5, cut along the dike. The top of the model is a (stress) free surface honoring topography, and the model is the same color throughout, indicating the homogenous material properties. The dike is 7.25 km wide and 6.6 km long (along strike), and the dike axis system is displayed as blue lines centered on the middle of the dike at the top of Hekla. The model domain is 90 km by 90 km by 25 km, with x, y, and z conventions displayed on lower left corner. Tree indicates land surface and is not to scale.

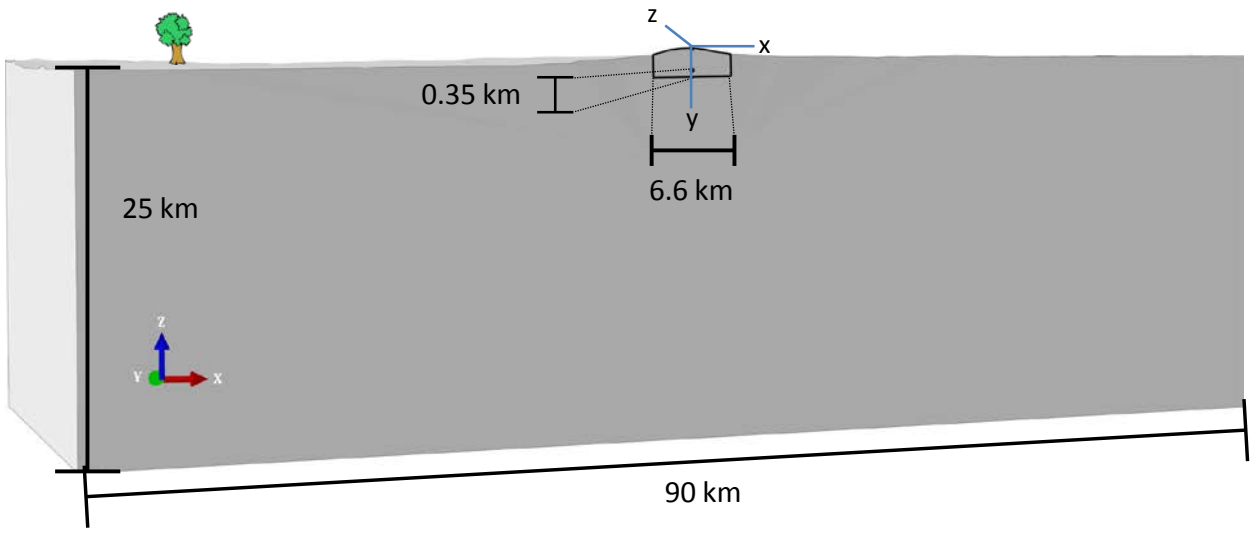

Figure 2.6. Cross-section view of model Ts-3, cut along the dike. The top of the model is a (stress) free surface honoring topography, and the model is the same color throughout, indicating the homogenous material properties. The dike is 1.75 km wide and 6.6 km long (along strike), and the dike axis system is displayed as blue lines in the middle of the of the dike at the top of Hekla. Small dot near the bottom of the dike represents sea level and the origin of the model domain, which is 90 km by 90 km by 25 km, with x, y, and z conventions displayed in lower left corner. Tree indicates land surface and is not to scale.

HEHS model or the other topographic FEMs. The second configuration of topographic FEMs has dikes with starting points at sea level, that extend down to the dike width below sea level. These models are called Ts-5b and Ts-3b, respectively (Figures 2.7-2.8) and are similar to models which use the topographic corrections of Williams and Wadge (1998, 2000). Therefore, the dikes have the same shape and surface area as the dikes for an equivalent HEHS model. The third configuration of topographic FEMs has dikes that begin at the top of Hekla and extend down the amount of their widths. For example, the depth from sea level down to the bottom of this topographic FEM of the 5.8 km reference dike width is approximately 4.4 km. This model is called Tt-5. The depth to the bottom of the dike which is 0.35 km wide (i.e. model number Tt-3) is approximately 1.4 km above sea level (Figures 2.9-2.10). In other words, the bottom of that dike plane never reaches sea level. This dike geometry has the smallest surface area of the three model configurations.

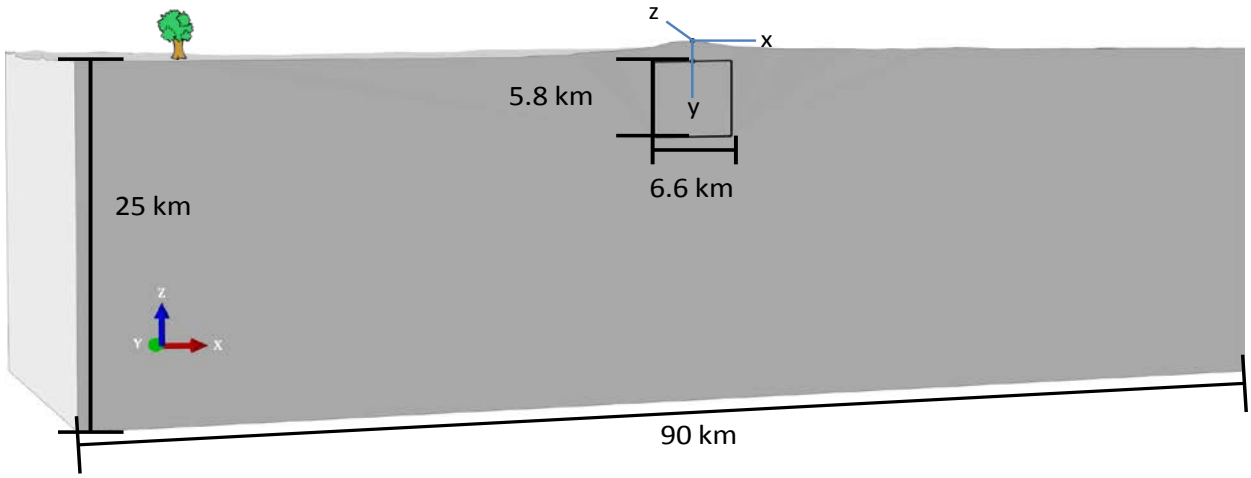

Figure 2.7. Cross-section view of the Ts-5b, cut along the dike. The top of the model is a (stress) free surface honoring topography, and the model is the same color throughout, indicating the homogenous material properties. The dike begins at sea level (i.e. it never intersects the surface), extends down to 5.8 km below sea level, and is 6.6 km long (along strike). The dike axis system is displayed as blue lines at the top of Hekla above the center of the top of the dike. The model domain is 90 km by 90 km by 25 km, with x, y, and z conventions displayed on lower left corner. Tree indicates land surface and is not to scale.

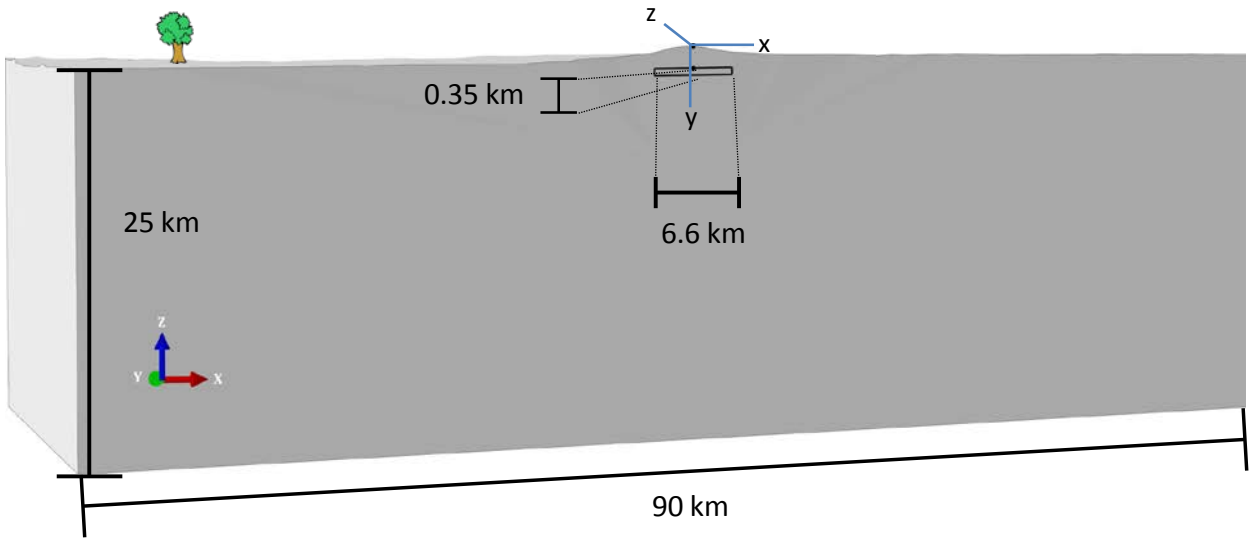

Figure 2.8. Cross-section view of the Ts-3b, cut along the dike. The top of the model is a (stress) free surface honoring topography, and the model is the same color throughout, indicating the homogenous material properties. The dike begins at sea level (i.e. it never intersects the surface), extends down to 0.35 km below sea level, and is 6.6 km long (along strike). The dike axis system is displayed as blue lines at the top of Hekla above the center of the top of the dike. The model domain is 90 km by 90 km by 25 km, with x, y, and z conventions displayed on lower left corner. Tree indicates land surface and is not to scale.

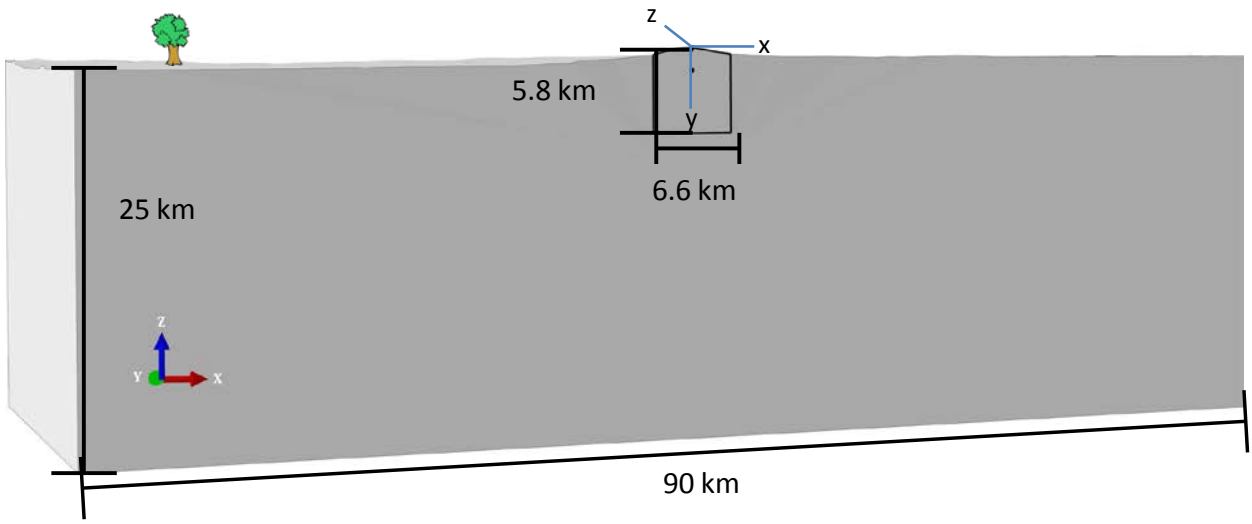

Figure 2.9. Cross-section view of Tt-5, cut along the dike. The top of the model is a (stress) free surface honoring topography, and the model is the same color throughout, indicating the homogenous material properties. The dike begins at the top of Hekla, extends down 5.8 km to roughly 4.4 km below sea level, and is 6.6 km long (along strike). The dike axis system is displayed as blue lines at the top of Hekla on the center of the top of the dike. Small dot near the top of the dike represents sea level, and the model domain is 90 km by 90 km by 25 km, with x, y, and z conventions displayed on lower left corner. Tree indicates land surface and is not to scale.

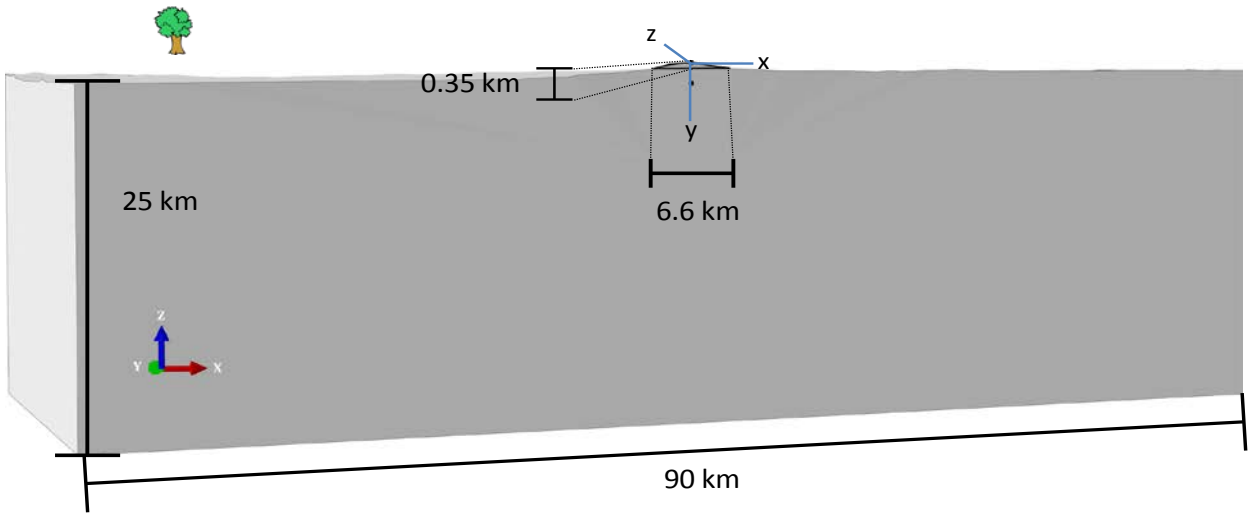

Figure 2.10. Cross-section view of Tt-3, cut along the dike. The top of the model is a (stress) free surface honoring topography, and the model is the same color throughout, indicating the homogenous material properties. The dike begins at the top of Hekla, extends down 0.35 km to roughly 1.4 km above sea level, and is 6.6 km long (along strike). The dike axis system is displayed as blue lines at the top of Hekla on the center of the top of the dike. Small dot under the bottom of the dike represents sea level, and the model domain is 90 km by 90 km by 25 km, with x, y, and z conventions displayed on lower left corner. Tree indicates land surface and is not to scale.

2. LEHS Model Configuration

In addition to exploring how topography can affect model predictions, another primary goal of this project is to demonstrate how layering of rock properties can affect model predictions. Layered models do not require a FEM setup, as alternative modeling techniques are available to include layers in deformation models (e.g. Roth, 1990). An FEM is used for the layered model in this study, however, to easily transition from the LEHS model to the LEHS model with topography embedded in the model domain. The innovations in this model design include the fact that a layered deformation model of Hekla has not been previously constructed, despite the fact that rock property differences exist both within the volcanic edifice and in the substrate below. As such, the results of this set of models have implications for future model design at Hekla but also at other volcanoes where rock property distribution may be known or inferred and can, therefore, be included in volcanic analyses.

The crustal profile from Haney et al. (2011), derived from ambient noise tomography (ANT), provides the basis for the rock properties used in the layered models of Hekla. ANT involves the cross-correlation and inversion of Earth's ambient seismic noise to quantify rock properties, such as shear wave velocity, in a given area (Masterlark et al., 2010; Haney et al., 2011). The cross-correlation of ambient noise between two stations can reproduce the Green's Functions (GFs) for that area by treating one station as a source and the other as the receiver (Masterlark et al., 2010). The oceanic microseism has been shown to be a viable source for ANT (Bensen et al., 2007; Masterlark et al., 2010; Shapiro et al., 2005) and is the source for ANT at Hekla volcano (Haney et al., 2011).

Precisely 52 days of data were collected from four broadband seismometers and were processed to create a one-dimensional crustal model (Figure 2.11) underneath station LARY (Figure 2.12), which is roughly 15 km southeast of the volcano summit. All seismometers are three-component, so multi-component passive seismic interferometry is used, requiring a type of multichannel automatic gain control so the temporal-normalization and spectral whitening filters can be applied identically across all three components (Masterlark et al., 2010, Haney et al., 2011). Haney et al. (2011) describe the crustal model using the mean and standard deviation of the HZ ratio, which describes the ellipticity of the particle motion. The HZ ratio can be inverted based on a perturbational theory posed by Tanimoto and Tsuboi (2009), which linearly relates perturbations in the HZ ratio to shear-wave velocity profile perturbations through a sensitivity matrix (Haney et al., 2011). The resulting model has lower shear wave velocity in the upper 1.5 km

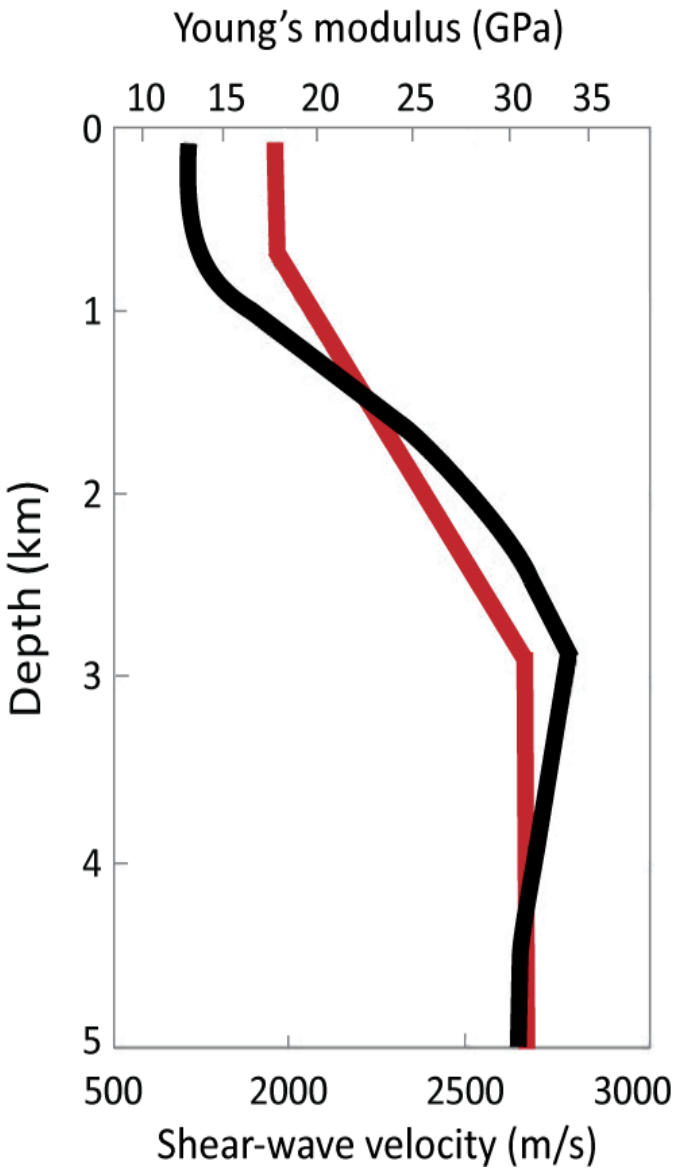

Figure 2.11. Shallow crustal model of Hekla (modified from Haney et al., 2011). The bottom x-axis is shear-wave velocity and the top x-axis is Young's modulus. The solid black line is the ANT inversion from Haney et al. (2011). The solid red line is the velocity model from Soosalu and Einarsson (1997) utilized as the initial guess for the Haney et al. (2011) inversion.

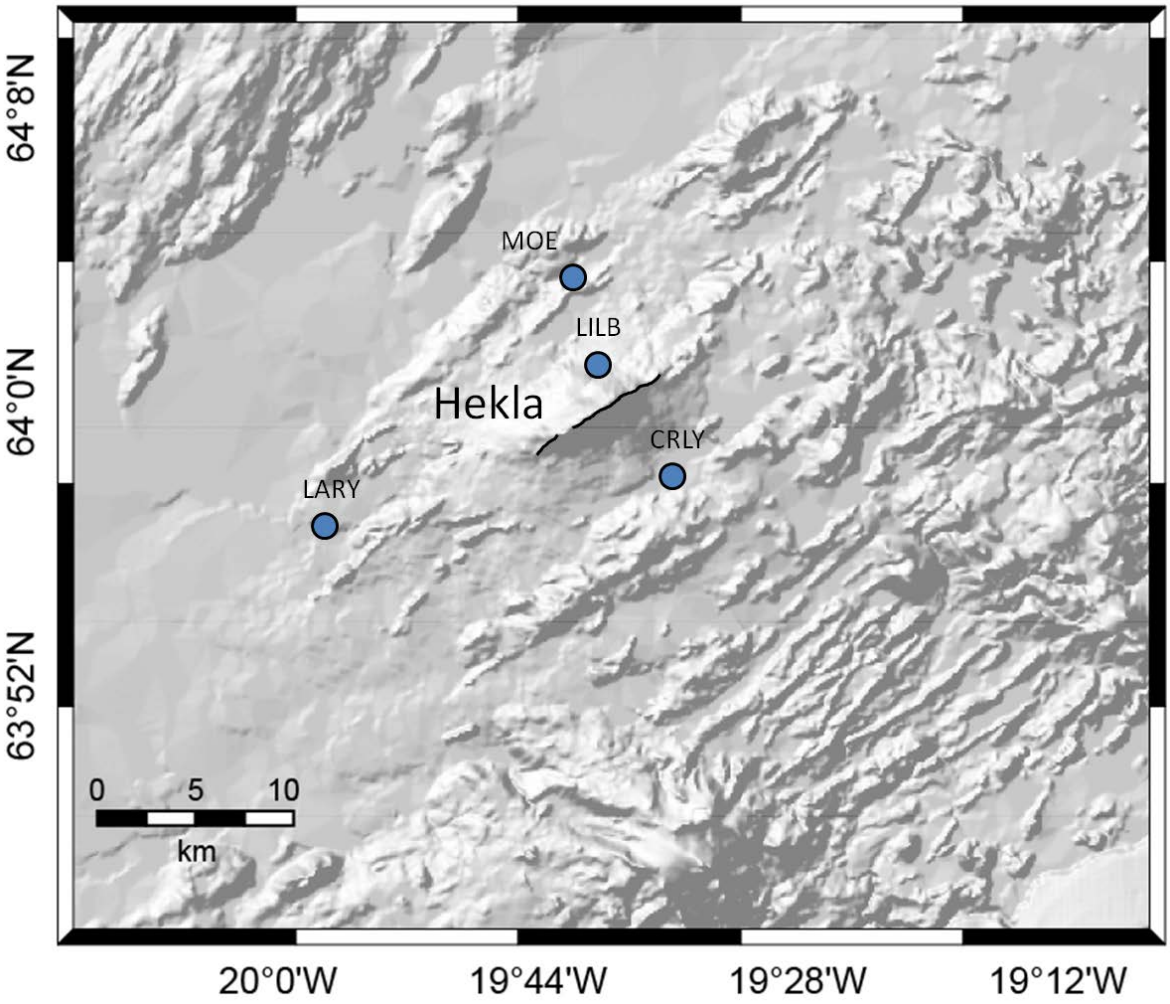

Figure 2.12. Hillshade image of Hekla showing the locations of the temporary seismometers. Locations of seismometers are from Haney et al. (2011) and are shown as blue circles with location names labeled above. Hekla is labeled, and the dike is delineated with a black line. Station LARY is where the crustal model of Haney et al. (2011) is derived.

and faster shear wave velocity in the next 2.5-4 km than a previous model postulated by Soosalu and Einarsson (1997). The slower velocity in the upper layer may represent loose volcanic sediment, as station LARY was located in a sediment-filled valley (Haney et al., 2011). Although such a profile may not be perfectly representative of the volcano, the Hekla edifice has been built up by layers of lava, loose volcanic sediment, and ash (Sigmundsson, 2006; Sigvaldason, 1974), so applying such a velocity profile to the volcano may still be appropriate.

The shear-wave velocity profile of Hekla (Figure 2.11) is used to create a layered elastic half-space (LEHS) FEM of Hekla. The shear-wave velocities are converted to Young's modulus using a simple equation:

$$E = V_s^2 * 2\rho * (1-\nu) \qquad 2.1$$

where E is Young's modulus, V_s is the estimated shear-wave velocity, ρ is the rock type density (I use basalt here), and ν is Poisson's Ratio. Poisson's ratio is assumed to be $\nu = 0.25$ (Grapenthin et al., 2010, Ofeigsson et al., 2011) and assumed density is $\rho = 2950$ kg/m^3 (Turcotte and Schubert, 2002), which is an appropriate crustal approximation for Hekla (e.g. Darbyshire et al., 2000). Although any one of the assumed variables could have different values in each layer, a goal of this study is to isolate the effects of alterations to the Young's modulus in successive layers. Published values for the other variables are chosen and held fixed in an effort to provide continuity throughout the models. Determining the exact crustal profile under Hekla in terms of Poisson's ratio, density, and/or Young's modulus is beyond the scope of this study. Ascertaining the effects layering in rock properties will have on model predictions is a goal of this study, and utilizing an established crustal model, rather than estimating the "best fit" crustal model, is the most efficient approach to achieve that goal.

The calculated Young's moduli are distributed by depth according to the corresponding shear-wave velocity profile from Haney et al. (2011). The profile shows considerable variability in the upper layers, and two variations of the layered model are employed to explore the effects of the layering. These variations are designed to capture the general nature of the profile without excessively characterizing the rock properties beyond reasonable constraints. The thickness of the top layer is either 1 km or 0.5 km. In the models which utilize a top layer of 0.5 km, the second layer is also 0.5 km, but all other layers in the model are 1 km, regardless of the thickness

of the top layer(s). This setup is utilized as a starting point to test the viability of the crustal profile in a model, but it still captures the general variability displayed in the profile. Changing the top layer thickness and properties will have the most effect on the results because the top of the model domain is a stress-free surface and all of the deformation data are from the surface. The property for each layer is taken from the properties at the bottom of that layer in the crustal profile (Figure 2. 11). This way, the transition between layers represents the full range of property differences in each layer.

The layering is designed in Abaqus by partitioning the model domain laterally. Two model configurations are generated. In the first model, four partitions are created where the first three are 1 km thick each, and the fourth layer encompasses the rest of the model domain. Although five layers, each 1 km thick, could be extracted from the profile, the bottom of the fourth and fifth layers have the same properties, so they are treated as one layer. The second model configuration uses five partitions. The top layer of this configuration is split into two 0.5 km thick layers. All other layers are the same as in the first configuration. Each partition is assigned material properties as summarized in Tables 2.2 and 2.3. The upper 2 km of the Haney et al. (2011) model have lower Young's moduli than the homogeneous Young's modulus of 30 GPa (Ofeigsson et al., 2011), while the next kilometer down has a higher Young's modulus. The rest of the model domain has a Young's modulus of approximately 30 GPa, which is in

Table 2.2. Table of rock property characteristics for the first LEHS FEM in which all layers are 1 km thick. The first column is depth, the second column is Young's modulus, and the third column is shear-wave velocity (Haney et al., 2011). The fourth and fifth columns are Poisson's Ratio and density, respectively (Grapenthin et al., 2010; Ofeigsson et al., 2011; Turcotte and Schubert, 2002).

Depth (km)	E (GPa)	V_s (m/s)	ν	ρ (kg/m^3)
0-1 km	14.3	1800	0.25	2950
1-2 km	27.7	2500		
2-3 km	33.5	2750		
> 3 km	29.9	2600		

agreement with the published Young's modulus for Hekla (Grapenthin et al., 2010, Haney et al., 2011, Ofeigsson et al., 2011).

A shortcoming of the uniform movement constraint on dike in these models is that the material properties of each layer cannot individually affect the movement of the dike. The dike movement is a result of the net effect of stress transmitted through all the layers, rather than an effect of the stress transmitted through each layer individually. If the dike had distributed movement, then the part of the dike passing through any given layer could respond to the material properties in that layer in a different manner than a part of the dike passing through a layer with different material properties. A uniform movement constraint does not allow that and may decrease the impact any one layer might have on the predicted dike movement and, therefore, on the predicted ground deformation of the model.

Table 2.3. Table of rock property characteristics for the second LEHS FEM, where the top two layers are 0.5 km thick. The first column is depth, the second column is Young's modulus, and the third column is shear-wave velocity (Haney et al., 2011). The fourth and fifth columns are Poisson's Ratio and density, respectively (Grapenthin et al., 2010; Ofeigsson et al., 2011; Turcotte and Schubert, 2002).

Depth (km)	E (GPa)	V_s (m/s)	ν	ρ (kg/m^3)
0-0.5 km	12.8	1700	0.25	2950
0.5-1 km	14.3	1800		
1-2 km	27.7	2500		
2-3 km	33.5	2750		
> 3 km	29.9	2600		

In an effort to explore this effect within a uniform movement constraint, the LEHS models use two different fissure widths: 5.8 km and 0.35 km. Because there is no topography in these models, all dikes extend their full width below sea level, and the lowercase letters in the model name convention are not used. A second number is added to the model names, however, indicating the number of layers in the uppermost kilometer of the model domain. FEMs with a top layer 1 km thick have a 1, while FEMs with a top layer that is 0.5 km thick have a 2 (Table 2.1).

Two FEMs of the 5.8 km wide dike are made: one with a top layer thickness of 1 km, and the other FEM with a top layer thickness of 0.5 km. These models are named L-5.1 and L-5.2 (Figures 2.13-2.14), respectively, and demonstrate the way rock properties transmit stress when

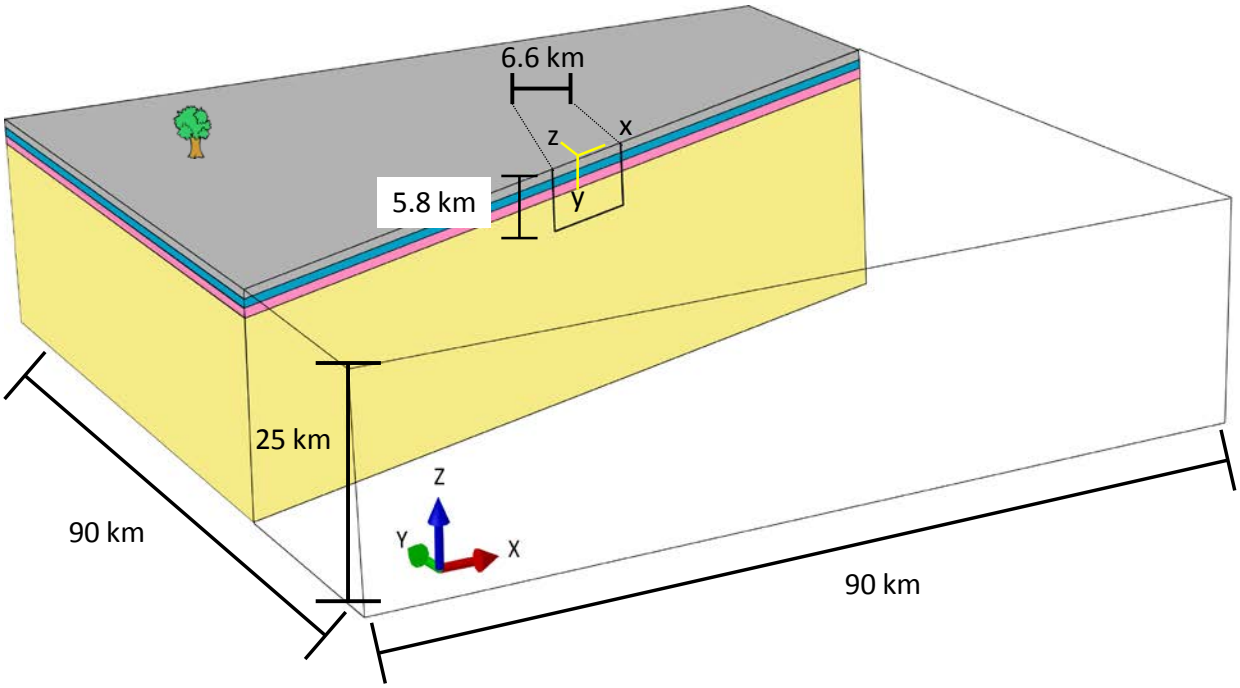

Figure 2.13. Cross-sectional view of L-5.1, cut along the dike. Different colors indicate different rock properties. Poisson's ratio for all layers is v=0.25 (Grapenthin et al., 2010, Ofeigsson et al., 2011). Young's modulus for the grey layer is 14.3 GPa, for the blue layer is 27.7 GPa, for the pink layer is 33.5 GPa, and for the yellow layer (i.e. the rest of the model domain) is 30 GPa (Table 2.2). The dike is 5.8 km wide and 6.6 km long, and the dike axis system is displayed by yellow lines on the dike and is centered on the origin of the model domain. The model domain is 90 km by 90 km by 25 km, with x, y, and z conventions displayed on lower left corner. Tree indicates land surface and is not to scale.

the dike cuts through all the layers. The FEMs of the 0.35km dike width demonstrate how the rock properties of an individual layer might affect the movement of the dike. The layering convention of these models is the same as they are for the FEMs of the 5.8 km dike. Due to complications with Abaqus partitioning, however, the top layer for one of the FEMs of the 0.35 km width dike could not be drawn at 0.5 km depth, but had to be drawn at 0.35 km depth. Such a design still fully contains the 0.35 km fissure in that top layer, however, which is the goal of this model design. The FEM of the 0.35 km dike with a 1 km thick top layer is called L-3.1, while the

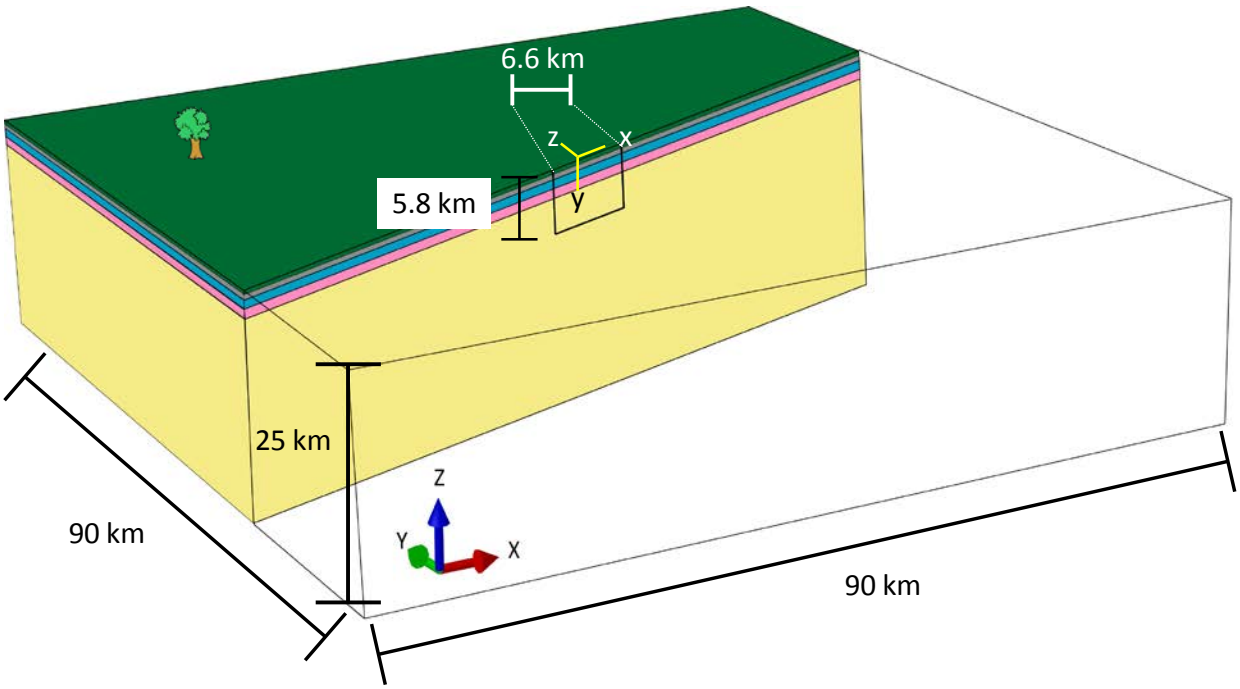

Figure 2.14. Cross-sectional view of L-5.2, cut along the dike. Different colors indicate different rock properties and the top layer two layers are 0.5 km thick. Poisson's ratio for all layers is v=0.25 (Grapenthin et al., 2010, Ofeigsson et al., 2011). Young's modulus for the green layer is 12.8 GPa, for the grey layer is 14.3 GPa, for the blue layer is 27.7 GPa, for the pink layer is 33.5 GPa, and for the yellow layer (i.e. the rest of the model domain) is 30 GPa (Table 2.3). The dike is 5.8 km wide and 6.6 km long, and the dike axis system is displayed by yellow lines on the dike and is centered on the origin of the model domain. The model domain is 90 km by 90 km by 25 km, with x, y, and z conventions displayed on lower left corner. Tree indicates land surface and is not to scale.

FEM of the 0.35 km dike with 0.35 km top layer is called L-3.2 (Figures 2.15-2.17). An extra FEM which has a top layer thickness of 1 km, but the same properties as the top layer in L-3.2 (i.e. Young's modulus of 12.8 GPa, Figure 2.17) is analyzed to further explore the influence of the top layer's material properties on dike movement when the movement is affected by the material properties of that layer. The name of that model is L-3.1Y12, indicating the Young's modulus of the top layer is 12.8.

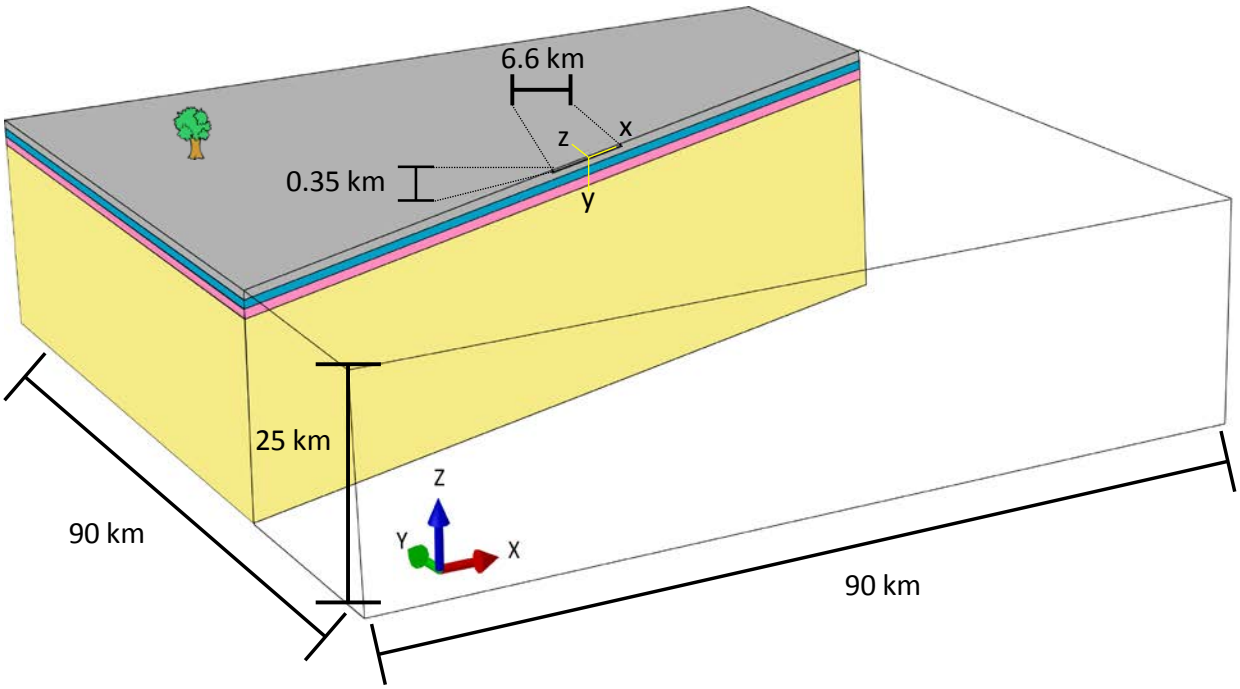

Figure 2.15. Cross-sectional view of L-3.1, cut along the dike. Different colors indicate different rock properties. Poisson's ratio for all layers is v=0.25 (Grapenthin et al., 2010, Ofeigsson et al., 2011). Young's modulus for the grey layer is 14.3 GPa, for the blue layer is 27.7 GPa, for the pink layer is 33.5 GPa, and for the yellow layer (i.e. the rest of the model domain) is 30 GPa (Table 2.2). The dike is 0.35 km wide and 6.6 km long, and the dike axis system is displayed by yellow lines on the dike and is centered on the origin of the model domain. The model domain is 90 km by 90 km by 25 km, with x, y, and z conventions displayed on lower left corner. Tree indicates land surface and is not to scale.

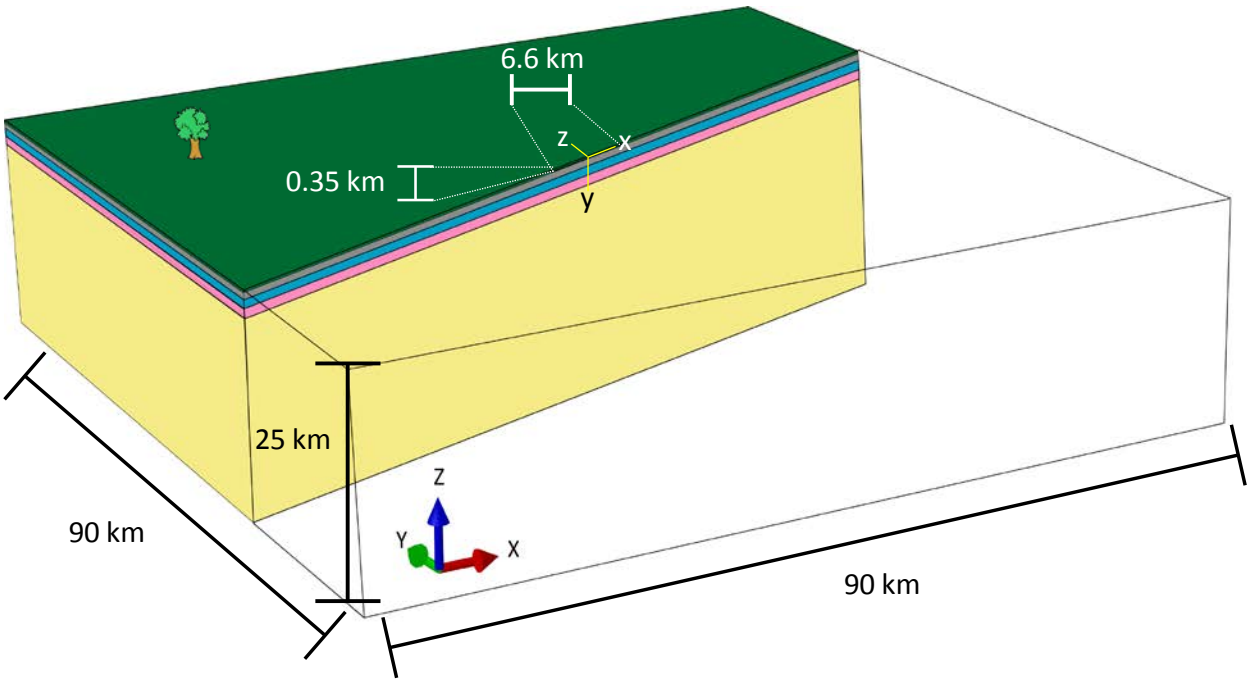

Figure 2.16. Cross-sectional view of L-3.2, cut along the dike. Different colors indicate different rock properties. Poisson's ratio for all layers is v=0.25 (Grapenthin et al., 2010, Ofeigsson et al., 2011). Young's modulus for the green layer is 12.8 GPa, for the grey layer is 14.3 GPa, for the blue layer is 27.7 GPa, for the pink layer is 33.5 GPa, and for the yellow layer (i.e. the rest of the model domain) is 30 GPa (Table 2.3). The dike is 0.35 km wide and 6.6 km long, and the dike axis system is displayed by yellow lines on the dike and is centered on the origin of the model domain. The model domain is 90 km by 90 km by 25 km, with x, y, and z conventions displayed on lower left corner. Tree indicates land surface and is not to scale.

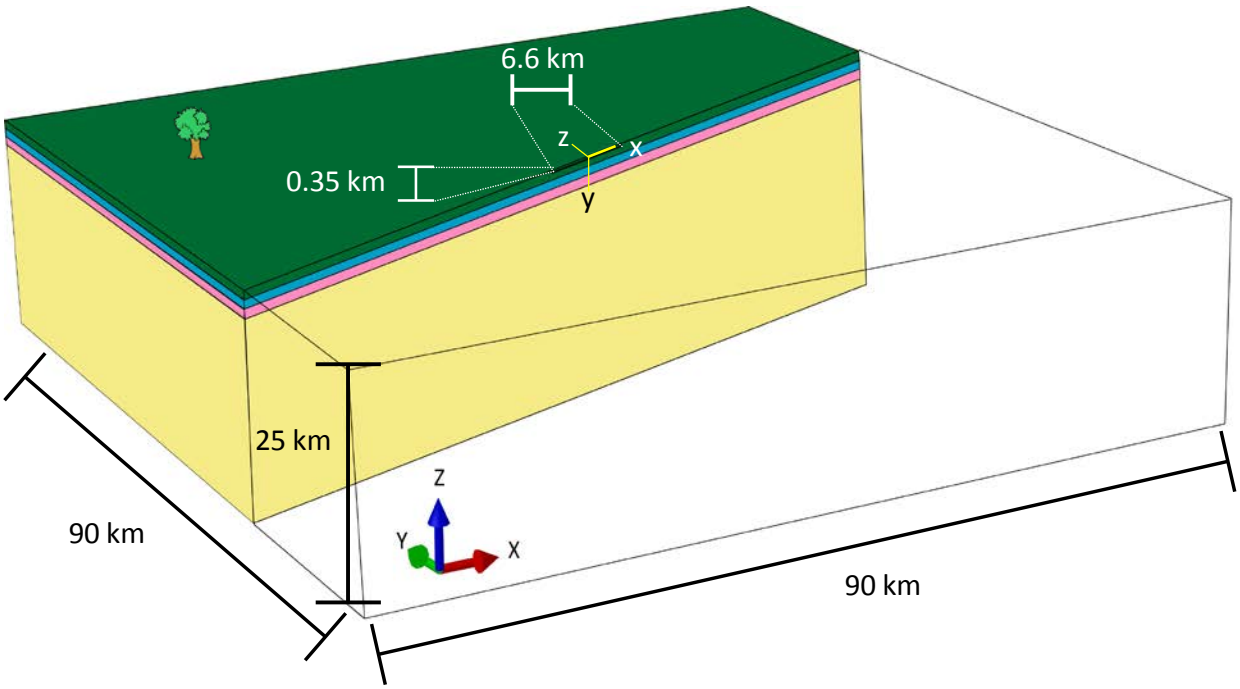

Figure 2.17. Cross-sectional view of L-3.1Y12, cut along the dike. Different colors indicate different rock properties. Poisson's ratio for all layers is v=0.25 (Grapenthin et al., 2010, Ofeigsson et al., 2011). Young's modulus for the green layer is 12.8 GPa, for the blue layer is 27.7 GPa, for the pink layer is 33.5 GPa, and for the yellow layer (i.e. the rest of the model domain) is 30 GPa (Table 2.2). The dike is 0.35 km wide and 6.6 km long, and the dike axis system is displayed by yellow lines on the dike and is centered on the origin of the model domain. The model domain is 90 km by 90 km by 25 km, with x, y, and z conventions displayed on lower left corner. Tree indicates land surface and is not to scale.

3. Layered Topographic FEM Configuration

The FEM with layered rock properties and a free surface representing topography explores the relationship between these characteristics and dike width. One of the end members for different configurations to explore this relationship is to have a layered model in which the topography is basically an extension of the model; there is nothing different in the representation of the actual volcanic edifice in terms of the dike or rock properties relative to the top portion of the model. This model configuration utilizes a top layer thickness of 1 km below sea level, meaning the volcanic edifice has the same rock properties as the top layer of the LEHS, effectively stretching the layer about 1.45 km (i.e. the elevation of Hekla). This configuration is

designed for two FEMs, one for each dike width (Figures 2.18-2.19), and the model names for the 5.8 km dike width and 0.35 km dike width are LTs-5.1 and LTs-3.1, respectively. This

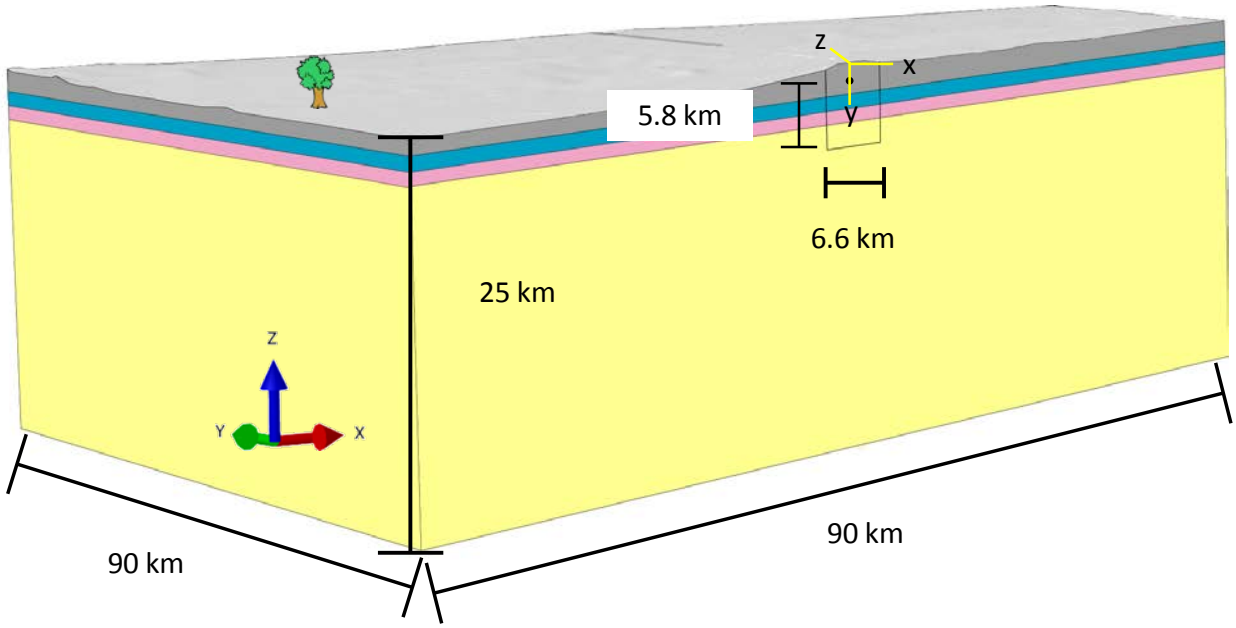

Figure 2.18. Cross-sectional view of LTs-5.1, cut along the dike. Different colors indicate different rock properties. Poisson's ratio for all layers is v=0.25 (Grapenthin et al., 2010, Ofeigsson et al., 2011). Young's modulus for the grey layer is 14.3 GPa, blue layer is 27.7 GPa, pink layer is 33.5 GPa, and yellow layer (i.e. the rest of the model domain) is 30 GPa (Table 2.2). Black dot in the middle of the top layer centered in the dike represents sea level and the origin of the domain. The dike extends down to 5.8 km depth below sea level and is 6.6 km long. The dike axis system is displayed by yellow lines on the dike and is centered over the origin. Model domain is 90 km by 90 km and 25 km deep with x, y, and z conventions displayed on lower left corner. Tree indicates land surface and is not to scale.

configuration has four layers. The other end member is to have the dike and top layer completely contained within the volcanic edifice. This end member is only possible with the 0.35 km wide dike and layering scheme with a top layer of 0.5 km. While multiple, different types of partitioning methods were attempted, the topographic geometry was too complicated to make a partition less than 1 km below sea level which could be assigned unique properties from the layer directly below it. This means the model with a 0.5 km thick top layer has a second layer that still extends 1 km below sea level. It will have a total of five layers. The partitioning required to

make a dike in Abaqus also restricted the dike width in this model. A fissure which terminated within the top layer could not be constructed because Abaqus would not render the model. This

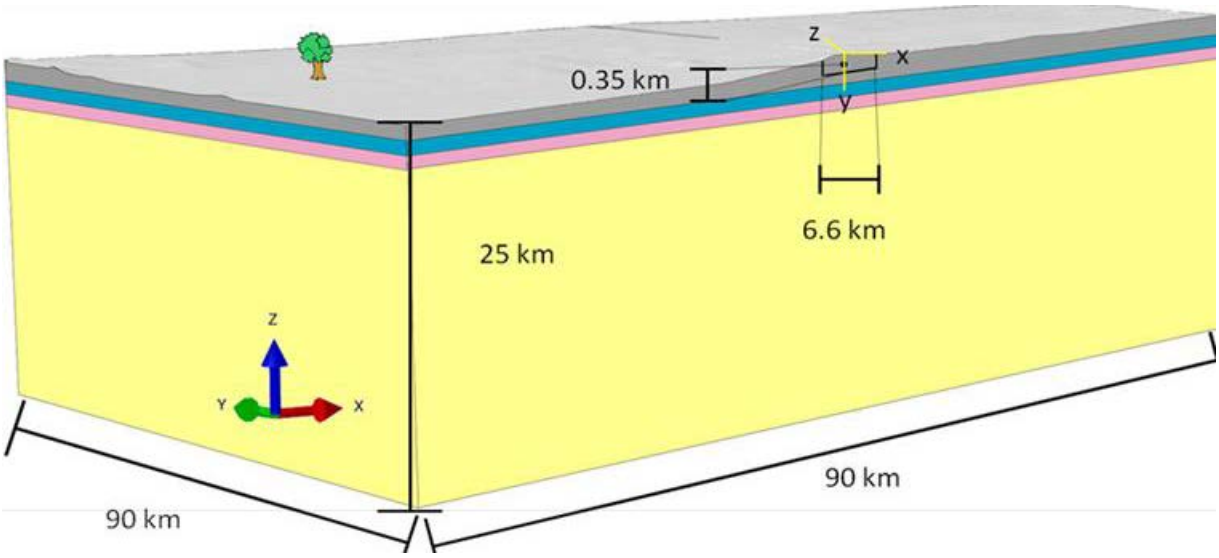

Figure 2.19. Cross-sectional view of LTs-3.1, cut along the dike. Different colors indicate different rock properties. Poisson's ratio for all layers is v=0.25 (Grapenthin et al., 2010, Ofeigsson et al., 2011). Young's modulus for the grey layer is 14.3 GPa, blue layer is 27.7 GPa, pink layer is 33.5 GPa, and yellow layer (i.e. the rest of the model domain) is 30 GPa (Table 2.2). Black dot in the middle of the top layer centered in the dike represents sea level and the origin of the domain. The dike extends down to 0.35 km depth below sea level and is 6.6 km long. The dike axis system is displayed by yellow lines on the dike and is centered over the origin. Model domain is 90 km by 90 km and 25 km deep with x, y, and z conventions displayed on lower left corner. Tree indicates land surface and is not to scale.

is likely due to the complications arising from having two perpendicularly oriented partitions placed only 0.15 km from each other within such a complicated area of the model. As such, the dike for this model configuration is 0.5 km wide, meaning the bottom of the dike is at the same depth as the bottom of the top layer (Figure 2.20). The name of this model will follow the convention scheme for a model of a 0.35 km wide dike and is called LTt-3.2. This dike still never crosses into the second layer, thus remaining contained within the first layer. Two other layered topographic FEMs of Hekla follow this five-layered scheme, one for each dike width, but

the dikes extend from the free surface and down to their corresponding widths below sea level. This configuration is designed for two FEMs, one for each dike width, and the model names for

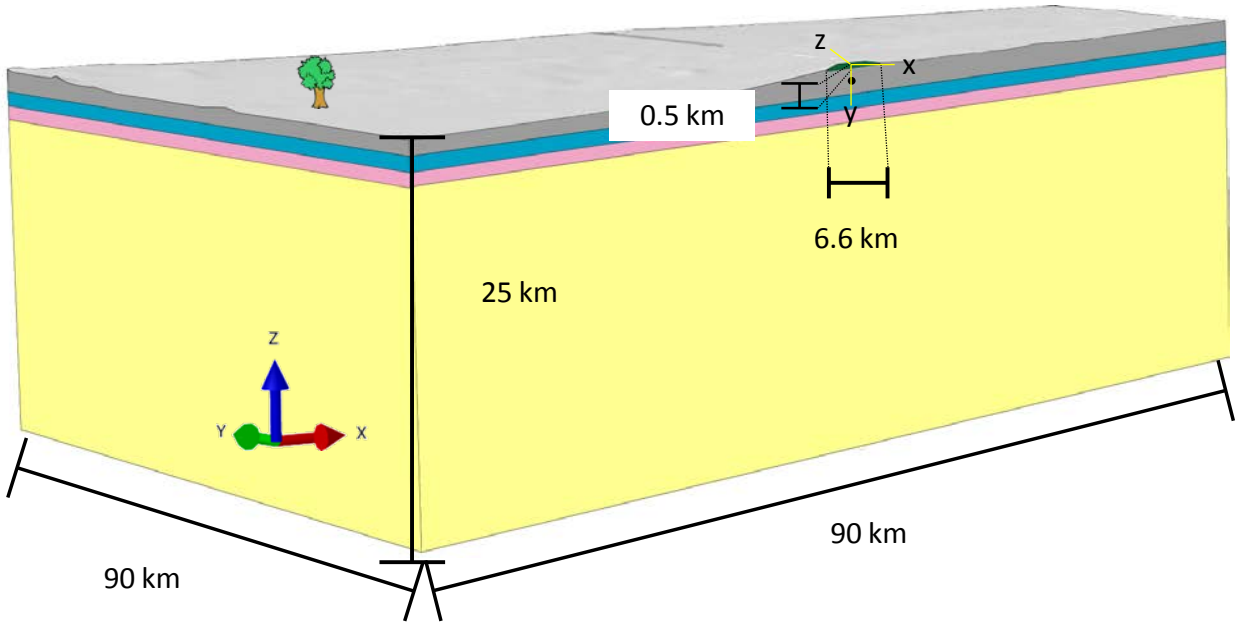

Figure 2.20. Cross-sectional view of LTt-3.2, cut along the dike. Different colors indicate different rock properties. Poisson's ratio for all layers is v=0.25 (Grapenthin et al., 2010, Ofeigsson et al., 2011). Young's modulus for the green layer is 12.8 GPa, grey layer is 14.3 GPa, blue layer is 27.7 GPa, pink layer is 33.5 GPa, and yellow layer (i.e. the rest of the model domain) is 30 GPa (Table 2.3). Black dot in the middle of the top layer centered in the dike represents sea level and the origin of the domain. The dike extends down 0.5 km from the summit and is 6.6 km long. The dike axis system is displayed by yellow lines on the dike and is centered over the origin. Model domain is 90 km by 90 km and 25 km deep with x, y, and z conventions displayed on lower left corner. Tree indicates land surface and is not to scale.

the 0.35 km dike width and the 5.8 km dike width are LTs-3.2 and LTs-5.2, respectively (Figures 2.21-2.22).

Blind dikes were attempted for both layering set-ups of the layered topographic FEM, but the model configuration with a 0.5 km thick top layer would not allow unique properties to be assigned to that top layer if a blind dike was constructed within the model domain. It is possible the complex geometry of the system coupled with extra complexities of unique property

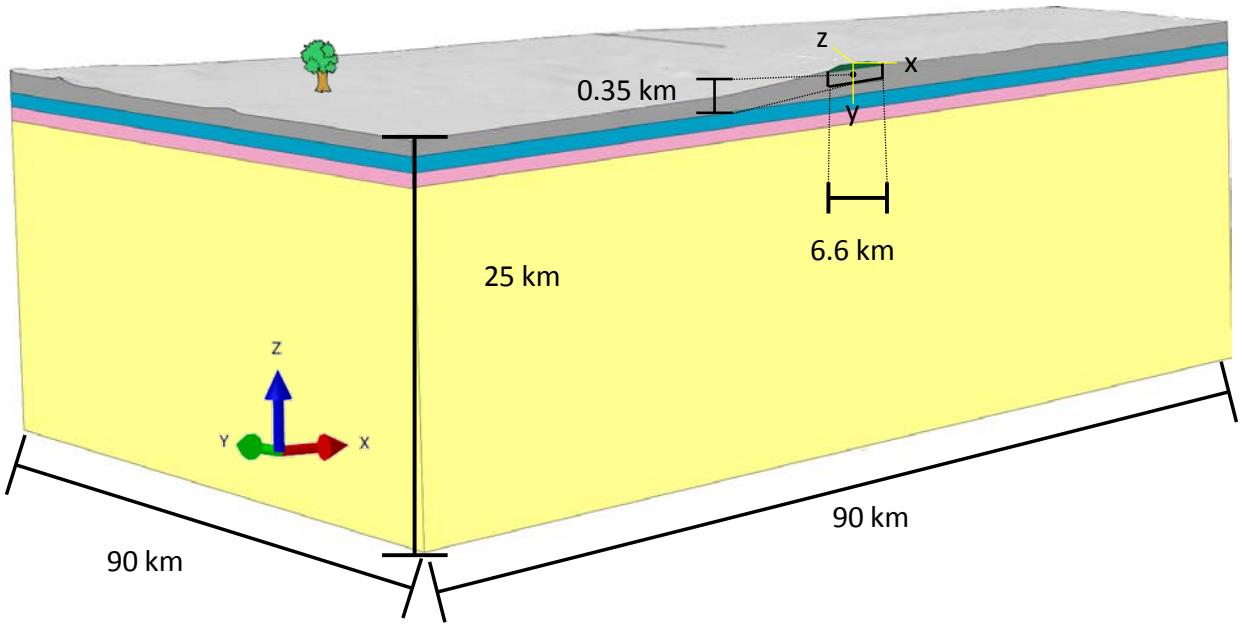

Figure 2.21. Cross-sectional view of LTs-3.2, cut along the dike. Different colors indicate different rock properties. Poisson's ratio for all layers is v=0.25 (Grapenthin et al., 2010, Ofeigsson et al., 2011). Young's modulus for the green layer is 12.8 GPa, grey layer is 14.3 GPa, blue layer is 27.7 GPa, pink layer is 33.5 GPa, and yellow layer (i.e. the rest of the model domain) is 30 GPa (Table 2.3). Black dot in the middle of the top layer centered in the dike represents sea level and the origin of the domain. The dike extends down to 0.35 km below sea level and is 6.6 km long. The dike axis system is displayed by yellow lines on the dike and is centered over the origin. Model domain is 90 km by 90 km and 25 km deep with x, y, and z conventions displayed on lower left corner. Tree indicates land surface and is not to scale.

definitions of the system is too much for Abaqus. Blind dikes are successfully made using the 1 km thick layer configuration, however, and the top of each dike begins in at sea level. These models are called LT-5.1b and LT-3.1b for their respective dike widths.

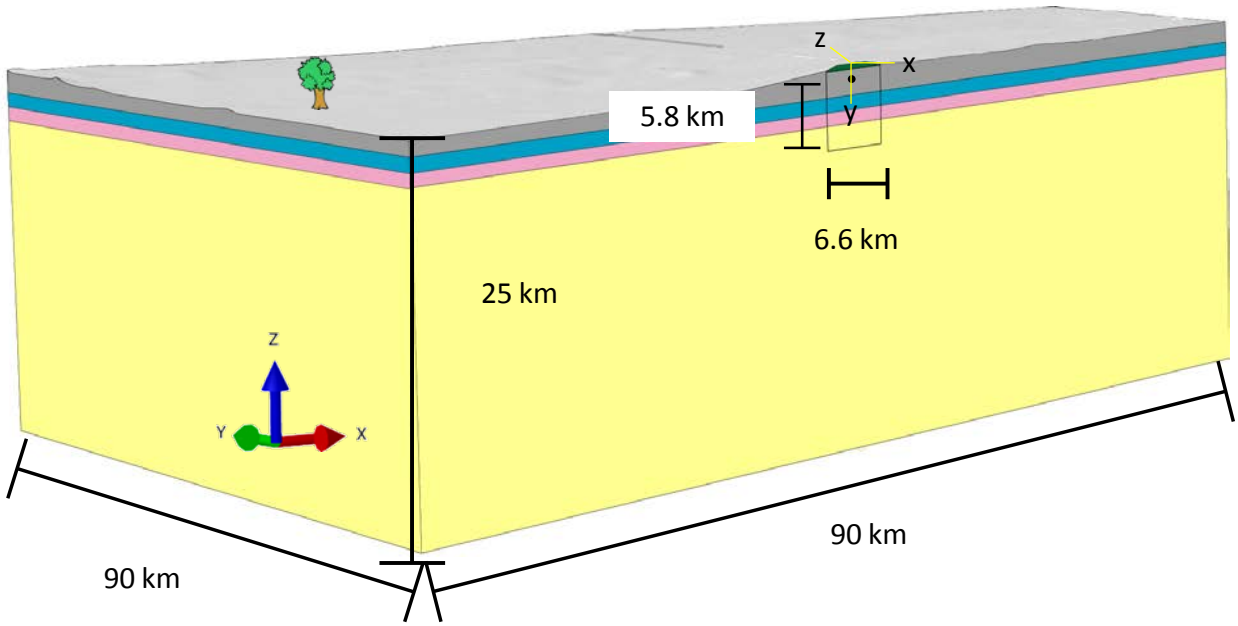

Figure 2.22. Cross-sectional view of LTs-5.2, cut along the dike. Different colors indicate different rock properties. Poisson's ratio for all layers is v=0.25 (Grapenthin et al., 2010, Ofeigsson et al., 2011). Young's modulus for the green layer is 12.8 GPa, grey layer is 14.3 GPa, blue layer is 27.7 GPa, pink layer is 33.5 GPa, and yellow layer (i.e. the rest of the model domain) is 30 GPa (Table 2.3). Black dot in the middle of the top layer centered in the dike represents sea level and the origin of the domain. The dike extends down to 5.8 km below sea level and is 6.6 km long. The dike axis system is displayed by yellow lines on the dike and is centered over the origin. Model domain is 90 km by 90 km and 25 km deep with x, y, and z conventions displayed on lower left corner. Tree indicates land surface and is not to scale.

VALIDATION

The basic input and assumptions of a model affect its ability to mimic a natural system. Therefore, rigorous testing of any new modeling method is required. The best way to do this is to design the model which uses a new method with the same assumptions as an accepted method, which acts as a baseline. A FEM can be designed as a HEHS, for example. Comparing the results of such an FEM to an actual HEHS model ensures the FEM is working properly, that meshing is adequate, that boundary and initial conditions are sufficient, and that the basis of the model is sound. The FEM, having been validated, can then be expanded to accept new inputs, and the effect of those inputs can be examined.

In this study, a HEHS of dike movement as described by Okada (1992) was built in IDL (http://www.exelisvis.com/ProductsServices/IDL.aspx), and an FEM was built in Abaqus which follows the same HEHS assumptions and uses the same parameters as the Okada model. Because the Okada design requires the x-axis of the model domain to line up with the strike of the fissure, the strike of the fissure in the FEM is changed to an exact E-W strike (E-W is the x-axis in the Abaqus model domain) to simplify the validation.

The Okada HEHS models provide a baseline for the FEM configuration, as such, validation is done by comparing the results of the forward model from each configuration. The forward model is:

$$\boldsymbol{Gm} = \boldsymbol{d} \qquad 2.2$$

where $\boldsymbol{G}$ is the Green's Function (GF) matrix, $\boldsymbol{m}$ is the fissure movement vector, and $\boldsymbol{d}$ is the data vector. GFs are differential equations subject to the initial and boundary conditions of the model (Menke, 1989, Hughes, 2011) and describe the behavior of a system. In the validation step, $\boldsymbol{G}$ is created in either Abaqus or by using Okada's equations in a mathematical program such as Matlab or IDL, an assumed $\boldsymbol{m}$ of 1 m of slip is implemented into both models, and the two resulting $\boldsymbol{d}$ matrices are the predicted displacements from the different model set-ups. The value used for $\boldsymbol{m}$ is completely arbitrary as long as it is non-zero and is the same value for both models, so a value of 1 m is used for simplicity. Because the same input for $\boldsymbol{m}$ is used, comparing the two $\boldsymbol{d}$ matrices effectively isolates and highlights any differences in the $\boldsymbol{G}$ matrices constructed by the two different methods. If Abaqus constructs a $\boldsymbol{G}$ matrix for a model following the assumptions of an Okada model, and that $\boldsymbol{G}$ matrix matches one which would be constructed by building the matrix directly using the relationships described by Okada, then the process by which Abaqus constructs the $\boldsymbol{G}$ matrix is validated.

An advantage the HEHS model has over the FEM is direct input of calculation points. Thus, the coordinates for each pixel of deformation measured by InSAR, which will be utilized in the inversion, are the same coordinates of the GFs from the IDL HEHS model. The GFs from the FEM, however, are associated with the coordinates of the nodes from the top of the FEM mesh, which must be interpolated to InSAR coordinates before the inversion. It is possible to constrain the nodes at the top of the FEM to the same coordinates as the InSAR data, but this causes too many nodes in the FEM. Utilizing all the InSAR points in the HEHS model is a trivial matter because the calculations are so fast due to the simplicity of the model, but it becomes more burdensome in the FEM. The process of validation demonstrates extra data points do not improve the results of the FEM and only slow down the calculations. It is much more efficient to interpolate the nodes of the FEM to the InSAR coordinates after the FEM analysis is complete and invert those interpolated values. The effect that interpolation has on the quality and accuracy of the results is determined by comparing the interpolated FEM results to the results of the IDL HEHS model which utilizes the InSAR coordinates as calculation points. Thus, there are two steps in the validation: the first step validates the FEM without interpolation of the results, and the second validates the interpolation.

The first step in the validation is to validate the FEM itself. Only the results which fall in the equivalent area covered by the InSAR data are utilized in both steps of the validation. This ensures any boundary effects of the FEM are insignificant and reflects the fact that only results which can be interpolated to the InSAR coordinates will be used in the final models. The locations for calculation points of the IDL HEHS are the extracted node locations from the HEHS FEM results. Validation is done using the misfit of Williams and Wadge (2000), which is

a ratio of the average difference between estimated displacements of each model at each node to the average magnitude of displacement of the reference model. The displacement at each node is:

$$\Delta(U) = \frac{\sum_{i=1}^{n} \left| U_i^{FE} - U_i^{HEHS} \right|}{N} \qquad 2.3$$

where U_i^{FE} is the predicted deformation from the FEM at point i, U_i^{HEHS} is the equivalent result from the HEHS model, and N is the number of calculation points. The average magnitude of displacement is:

$$M(U) = \frac{\sum_{i=1}^{n} \left| U_i^{HEHS} \right|}{N} \qquad 2.4$$

The misfit of the calculated GFs in all three directions (x, y, and z) for both movements (strike-slip and opening) from the two models is calculated and demonstrates the FEM and HEHS are in excellent agreement. Table 2.4 shows the ratio $\Delta(U_0)/M(U_0)$ is less than 0.05 for all movements without any interpolation of the GFs to the InSAR data. The value of 0.05 indicates that, within a the data are 95% similar. Figure 2.23 shows an example of the results for the model and their residuals.

Table 2.4. Ratio of mean misfit and average magnitude (Williams and Wadge, 2000) for the Green's Functions of the analytical and numerical models.

	Ux	**Uy**	**Uz**
Opening	0.038	0.0066	0.048
Strike-Slip	0.0073	0.020	0.024

The next validation step is validation of the interpolation. Results from the FEM within 6 km of the fissure center are extracted and interpolated to the InSAR coordinates within that area. This is the same area Ofeigsson et al. (2011) indicated is most affected by the fissure in the InSAR data. Figure 2.24 provides an example of the results for both models and their residuals. The misfit (Williams and Wadge, 2000) of the interpolated GFs in all three directions for both movements is calculated and show the interpolation can affect the results (Table 2.5) but the misfit remains below 0.05 for most movements.

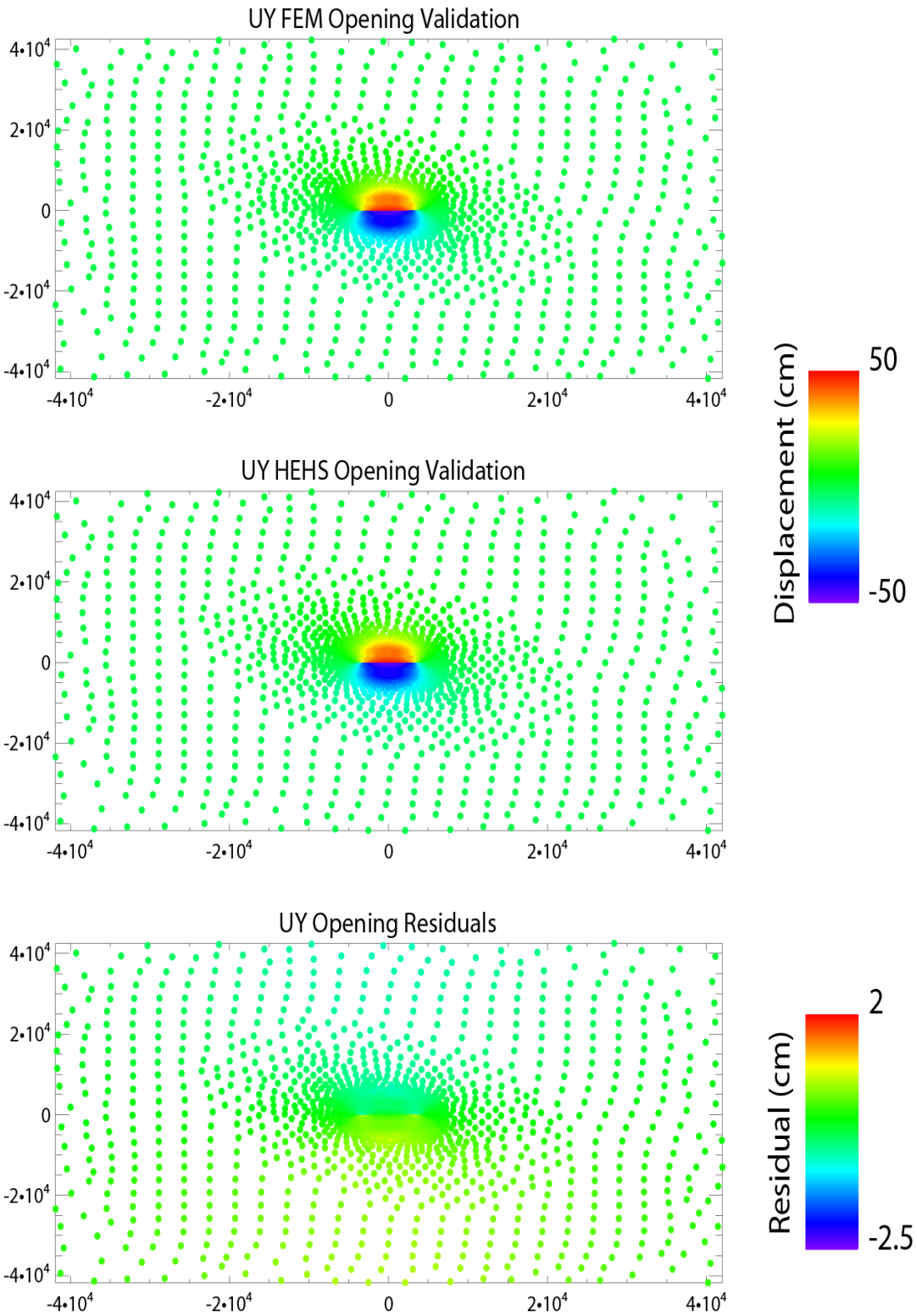

Figure 2.23. Example of the results given by both models and the residuals without interpolation. Opening is applied uniformly across the dike. The misfit (Williams and Wadge, 2000) for these results is 0.0066 (Table 2.4).

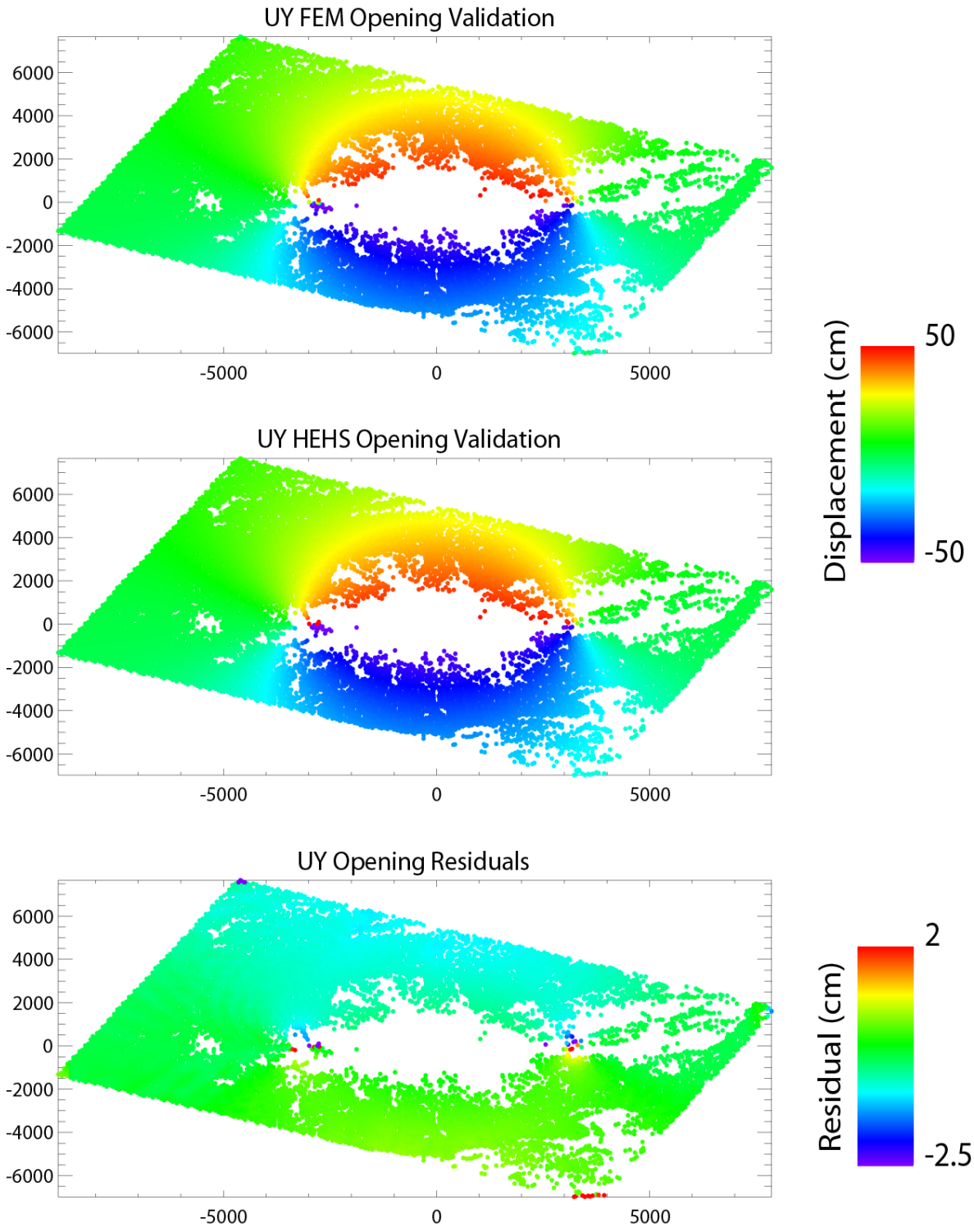

Figure 2.24. Example of the results given by both models and the residuals after interpolation to InSAR data points. The misfit (Williams and Wadge, 2000) for these results is 0.021 (Table 2.5).

There are a few important things to keep in mind with the interpolation validation results, especially with displacements in the z direction (Uz). The Williams and Wadge (2000) misfit does not take into account the scale of the values being compared. Most of the predicted displacements from the models in the z direction are quite small, on the millimeter scale or smaller. Thus, the differences between these values also are millimeter scale or smaller. While those differences are significant compared to each other, they are just at or beyond the detection limit of the InSAR data. Thus, within the detection limits of the data used in the calibration, the models predict the same deformation.

Table 2.5. Ratio of mean misfit and average magnitude (Williams and Wadge, 2000) for the interpolation validation. Although the misfit for opening in the z direction seems large, differences between values are millimeter and sub-millimeter scale, which is at or below the ability of InSAR to detect.

	Ux	**Uy**	**Uz**
Opening	0.027	0.021	0.11
Strike-Slip	0.023	0.029	0.017

CALIBRATION

1. InSAR Data and Preparation

Geodetic techniques such as InSAR produce invaluable, spatially dense centimeter to millimeter measurements of deformation related to volcanic eruptions (https://earth.esa.int/web/guest/missions/esa-operational-eo-missions/ers/satellite). The InSAR data which captured the deformation pattern from the 2000 eruption of Hekla (Figure 1.2) was processed for use in inverse analyses of the dike movement by Ofeigsson et al. (2011) based on amplitude and phase stability, noise, and general atmospheric coherency. The SAR data used to derive the InSAR have a topographic accuracy of 3 m, a spatial resolution of 30 m, a swath width of 100 km, and a wavelength of 5.6 cm (Table 2.6).

After processing, the data comprised 131,374 pixels. An area 12 km east-west by 12 km north-south, centered around the fissure, is extracted from the larger InSAR data and used in the inversion of the predicted deformations within that area. These dimensions are guided by an approximation of the model domain utilized by Ofeigsson et al. (2011) and were selected based on the criteria that the deformation signal within be related mainly to the fissure movement during the 2000 eruption. The deformation signal beyond this distance is likely more closely related to longer-wavelength deformation associated with sources deeper than the fissure, such as the inferred deep seated magma chamber (Ofeigsson et al., 2010). The deep seated magma chamber signal is present within the entire area investigated in this study, and the data must be adjusted for this before any dike modeling can be performed.

Table 2.6. Information about the InSAR data utilized in this study (Ofeigsson et al., 2011, https://earth.esa.int/web/guest/missions/esa-operational-eo-missions/ers/satellite). The average LOS vector is calculated from the average LOS vector for each pixel from the original data set.

SAR Image Pairs	
Image 1	October 15, 1999 ERS descending track 51
Image 2	June 16, 2000 ERS descending track 51
SAR data	
Wavelength	5.6 cm
Topograpic accuracy	3 m
Spatial resolution	30 m
Swath width	100 km
Wavelength	5.6 cm
Frequency	5.3 GHz (C-band)
Bandwidth	15.55 ± 0.1 MHz
Average LOS	[0.326176, -0.0982610, 0.926473]

The deformation of the general area beyond the flanks of Hekla (Figure 1.2) is likely related to behavior of the magma chamber below Hekla before and after the eruption (Pedersen, 2009, Ofeigsson et al., 2011). There is a large area of incoherence directly over the summit of the volcano, but what is there indicates the northwest side of the volcano moved over 25 cm away from the satellite, lengthening the LOS displacement, and the southeast side of the volcano moved over 15 cm towards the satellite, shortening the LOS displacement.

The InSAR data include several other imprints of deformation other than the fissure. These include constant uplift from receding Icelandic glaciers, the maximum of which may exceed 19 mm/yr (Arnadottir et al., 2009). There is also relative subsidence centered on Hekla, likely caused by loading of the crust from lava flows and the volcano itself (Grapenthin et al., 2010; Ofeigsson et al., 2011; Geirsson et al., 2012; Sturkell et al., 2013). The magnitude of these deformations over the time scale captured by the InSAR, and the resolution of the InSAR itself, render the influence these signals have on the data used for this study irrelevant. The long-term loading of the crust by the volcano is an inelastic, long wave-length effect and is not significant given the timeframe, geographic extent of the data used in the inversions, and the fact that the fissure is in the uppermost portion of the crust. Also, including topography in the model automatically adds the relevant load.

Other deformation imprints requiring consideration include the deep-seated magma chamber and deformation caused by lava loading and cooling after the 2000 eruption (Ofeigsson et al., 2011, Grapenthin et al., 2010). These signals play a bigger role in the context of this study than the signals discussed previously and must be accounted for (Grapenthin et al., 2010; Ofeigsson et al., 2011; Pedersen, *personal comm*). The main part of the elastic component of the loading due to the lava from the 2000 eruption is masked by removing data points corresponding to these lava flows. A map of the lava flows is overlain on the data in Rhino, and the points within and along the boundaries of the flows are removed from the data, and a new dataset is output. The signal from the magma chamber can be accounted for many ways, but the method utilized in this study is to calculate the deformation from the chamber can be calculated using Mogi's model of deformation (Mogi, 1958), which is a HEHS model design for calculating deformations related to a magma chamber simulated as either a point source or pressurized

spherical cavity. The maximum of the deformation signal caused by the deflation of the magma chamber during the eruption (Figure 2.25) is less than 7 cm in the HEHS (Mogi, 1992), contained within the 6 km area used for the inversions and is subtracted from the signal.

The precise chamber signal in each of the configurations for this study is much more difficult to ascertain because these models do not follow HEHS assumptions. Determining the signal with greater accuracy would require a magma chamber to be input to the FEM domain, which causes a number of logistical problems. The FEM model domain is only 25 km deep, and the magma chamber is estimated to be at 14 km (Ofeigsson et al., 2011, Soosalu and Einarsson, 2004) making it too close to the lower boundary not to be effected by the boundary. Also, new lateral boundaries and a mesh seeding scheme would have to be derived for a model which includes the chamber. Thus, the surface deformation signal calculated from the best-fit Mogi model from Ofeigsson et al. (2011) is used as a good approximation for the deformation caused by the pressure drop in the deep-seated chamber, and this is removed from the InSAR signal.

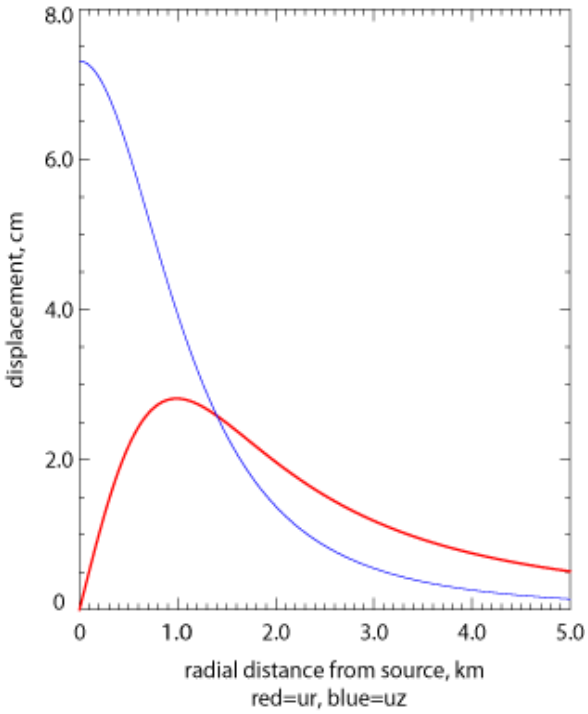

Figure 2.25. Results from the Mogi correction calculation based on the best-fit chamber dimensions from Ofeigsson et al., 20110.

An important way remotely gathered InSAR data differ from ground-based (e.g. GPS) data is that the displacements measured are not relative to positions on the Earth's surface, but rather to the satellite's position in space. Thus, predicted displacements from an Earth-based

referenced system must be projected into the satellite's reference system. Space-borne radar instruments sample targets that are necessarily off-nadir and parallel to a LOS vector. The LOS vector describes the directions of the displacements relative to the satellite. The Earth-based deformations can be projected to the LOS vector by assuming a fixed satellite position. The LOS vector used in the inversions is calculated as an average of all the LOS vectors for each displacement vector of each pixel from the processed data and is listed in Table 2.5.

2. Inversion

GFs for displacement are calculated by predicting deformation caused by 1 m of slip along the dike in separate opening and strike-slip movement simulations using equation 2.2. An initial slip of 1 m is used for simplicity's sake, but the actual value is arbitrary as long as the results of the inversions are scaled appropriately for any other value besides 1 m. The dike is treated as a single plane, which is initially closed, but it moves instantaneously during the eruption (i.e. it is allowed to uniformly open or slip during the simulation). An algorithm that systematically creates the kinematic equations, executes the models, and extracts the GFs for both opening and strike-slip is implemented. This same algorithm performs the inversion of the resulting system of linear equations to calculate the least-squares estimate of the dike movement vector, $\boldsymbol{m}^{est}$:

$$\boldsymbol{m}^{est} = (\boldsymbol{G}^T\boldsymbol{G})^{-1}\boldsymbol{G}^T\boldsymbol{d} \qquad 2.5$$

where $\boldsymbol{G}^T$ is the transpose of $\boldsymbol{G}$ and $(\,)^{-1}$ is the matrix inverse operator. The assumption of a linear system is valid because displacement along the dike plane is linearly related to ground deformation, unlike the geometry of the dike, which is nonlinearly related to deformation.

Because $\boldsymbol{m}$ is 1 m for equation 2.2, any value of $\boldsymbol{m}$ solved for in equation 2.5 will not need to be scaled. Covariance of model estimates is calculated using a parameter covariance matrix:

$$[cov\ \boldsymbol{m}] = \sigma_d^2(\boldsymbol{G}^T\boldsymbol{G})^{-1} \qquad 2.6$$

where$[cov\ \boldsymbol{m}]$ is the covariance matrix of $\boldsymbol{m}$, and σ_d^2 is the variance of the data (Wang, 2000). The assumed variance is 1 cm because this is the max error associated with InSAR data (Lillesand et al., 2004q). Utilizing this error maximizes the calculated variance for the model parameters, producing a "worst case" scenario for my model estimates.

The $\boldsymbol{m}^{est}$ values are then input to the kinematic equations to generate GFs and execute a forward model which predicts the ground deformation during the eruption. These data are projected onto the LOS reference system and used in calculations of residuals:

$$R_i = (\boldsymbol{d}_i - \boldsymbol{G}_i\boldsymbol{m}^{est}) \qquad 2.7$$

where R_i is the prediction residual of pixel *i*, $\boldsymbol{d}_i$ is the LOS displacement measured by InSAR and $\boldsymbol{G}_i\boldsymbol{m}^{est}$ is the predicted displacement projected onto the LOS reference system. Some of the models yield a large range of predicted deformation and subsequent residuals, but have a rapid drop-off in predicted deformation values away from the fissure. Thus, the scale used for the figure may not display the full range of values. Scales for the figures of the predicted deformation of all models are determined based on the ability of the scale to best display the pattern of deformation the model predicts. Similar scales between models are used when possible, but the predicted deformations of many models cannot be properly displayed unless a unique scale is used. The maximum range of predicted deformation is given in the corresponding summary table for each model configuration. Scales of the residuals for all models, however, are between 1 and -1 cm so the prediction of the data can be compared between all models. Results from H-5 (Figure 2.26) are given as an example.

The meshing algorithm in Abaqus does not always follow the same convention when creating the nodes on the dike. When the kinematic constraints are applied to the dike (Figure 2.4), the same side of the dike may move the opposite direction from one model to the next because the meshing convention can change between models. For example, node A on the northwest side of the dike in one model might be node B in the next. There is no way to control the meshing protocol in Abaqus. Thus, sign control after the inversion is implemented such that

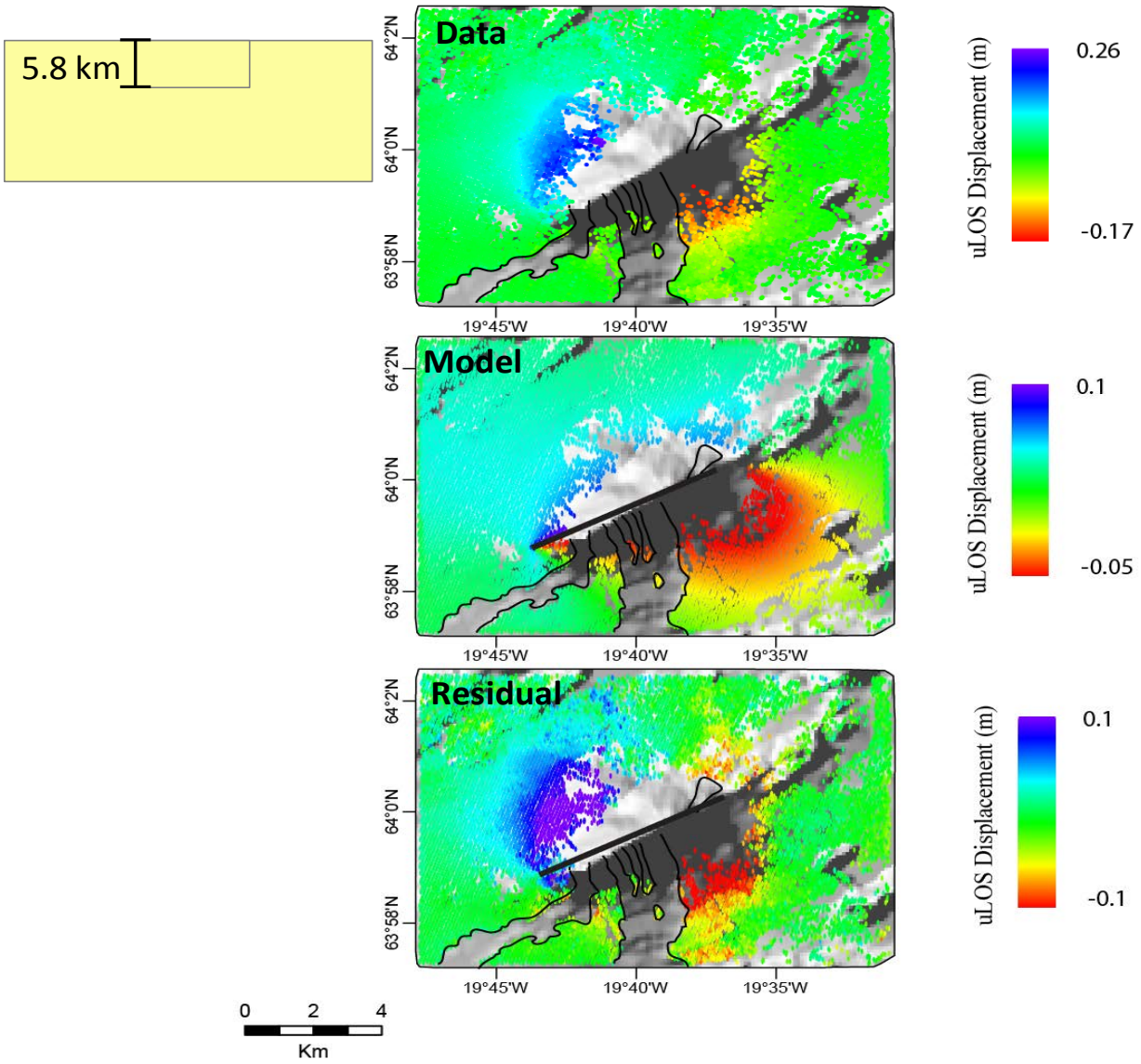

Figure 2.26. Results of H-5. Inset gives a zoomed-in view of the dike configuration. The Young's modulus for the model is 30 GPa. The top image is the InSAR data used, and the lava load is masked from the data. The dike is represented as a black line in the Model and Residual.

opening is always positive and strike-slip is always negative. This can be done because the displacements are linear to the load; meaning the magnitude doesn't change even if the direction does.

3. F-Tests

Almost any complicated model should predict the data better than a simplified one, but it is necessary to know if those predictions are *statistically* better (Menke, 1989). An F-test provides a bulk comparison of the variance from the predictions of the two models:

$$F = \frac{s_0^2}{s_1^2} \; with \; s^2 = \frac{1}{(N-1)} \sum_{i=1}^{N} e_i^2 \qquad 2.8$$

where: where s_0^2 is the sum squared error (SSE) of the baseline model and s_1^2 is the SSE newer model (Menke, 1989). The value of *s* is calculated from the summed square of the residuals:

$$SumSqErr = \left(\sum_{i=1}^{N} R \right)^2 = e^T e \qquad 2.9$$

where *e* is the error vector of the model.

An F-test is implemented comparing the predictions of all configurations to their equivalent dike length in the other configurations. The null hypothesis is H_0: $s_0^2 = s_1^2$, and is true if the value of the F-test is less than a critical value. The number of degrees of freedom for the test in all models is $d = N - M$ = 10,399 - 2, making the critical value, c=1.03, for a significance level of α = .05. These comparisons are bulk comparisons, however, and require geologic context before any meaning is applied to the implications of the results. Some models predict very large deformations in only a few pixels, while others may predict extremely small deformations

throughout. Such disparities can cause a configuration which may visually fit the data better than another configuration to yield an F-test statistic indicating it does not fit the data well.

VERIFICATION AND POST-AUDIT

The next two stages of the modeling protocol are verification and post-audit. These are done for models attempting to discern best-fit parameters, which ideally should lead to the model predicting the observed deformation in a statistically similar way. Discerning the best-fit geometry is not a goal of this study because the best-fit parameters are not linearly related to the deformation. Verification involves using a set of data not involved in the calibration to test the model predictions. This is ideally done once the calibrated model predicts deformations which are statistically similar to observed deformations. In the case of Hekla, dry levelling tilt and strain data (Sturkell et al., 2013) could provide excellent datasets for this purpose.

The final step is to post-audit the model. At Hekla, this would be a post-audit using the next eruption and the associated surface deformation. Post-audits are tenuous because the system often changes between the time the model is created, or from the time the data used for calibration is collected, requiring some sort of new model design or input. This information, however, could be useful for investigating the way a system changes through time.

CHAPTER 3

RESULTS AND DISCUSSION

CHAPTER BRIEF

The inversion, forward model, and calculation of residuals for the FEM with topography, LEHS model, and layered FEM with topography are compared with the InSAR data to determine how each alteration affects estimates of dike behavior. Although the geometries utilized in the models are from "best fit" results of published works (Ofeigsson et al., 2011; Sturkell et al., 2013), the employed geometries are quite different from each other, and both come from different modeling techniques than the FEMs employed here. The configurations for each type of model, however, should isolate the effect each input has on predicted deformations for an unbiased assessment.

FEM WITH TOPOGRAPHY

1. Results

An FEM is modified to simulate HEHS assumptions to test the sensitivity of fissure behavior and deformation predictions to topography (Figure 2.5-2.10). Three model configurations using different references for two different dike geometries are explored for a total of six configurations. In the first configuration, the dike begins at the summit of Hekla, extending down to the equivalent depth below sea level of the dike width (Figures 2.5-2.6).

This model configuration for the 5.8 km dike and 0.35 km dike is called Ts-5 and Ts-3, respectively. The second configuration of topographic FEMs has dikes which start at sea level and extend down to the dike width, meaning they are blind dikes (Figures 2.7-2.8). In this configuration, the dikes have the same shape and surface area as the fissures for the equivalent HEHS models. These model configurations are called Ts-5b and Ts-3b, respectively. The third type of configuration of topographic FEMs use the top of Hekla as a reference, and extend down to the dike width from there (Figures 2.9-2.10). These models are Tt-5 and Tt-3, respectively.

Results for the FEMs with topography are summarized in Table 3.1, and deformation predictions and residuals for the forward models are shown in Figures 3.1-3.6. As seen in the figures, residuals for all models indicate the geometries and configurations used do not predict the deformations in a satisfactory manner, but differences in the predictions of fissure movement from these configurations still provide insight to controlling factors of dike behavior.

The unusual pattern of deformation predictions in Figures 3.2 and 3.6 are attributed to meshing complications created when the dike does not intersect the surface. As discussed, the mesh is denser along the dike, and such mesh density carries over to the free-surface of the model domain near the line of intersection between the dike and the surface. The density of the mesh along free-surface of the model configuration using blind dikes, however, does not increase because there is no surface expression of the dike. Thus, although the validated meshing protocols are followed for the model configurations of the blind dikes, another mesh configuration is worth exploring in future work, even though such a configuration cannot be validated using an equivalent analytical model because no such analytical model exists.

Results of the H-5 and H-3 models are summarized in Table 3.2. H-5 is the control for the equivalent (i.e. same dike width) topographic FEMs, meaning the following comparison of

Table 3.1. Summary results from the topographic FEM configurations.

	Ts-5	Ts-5b	Tt-5	Ts-3	Ts-3b	Tt-3
Open (cm)	3.4 ± 2 cm	3.2 ± 3 cm	7.6 ± 2 cm	3.6 ± 2 cm	16 ± 23 cm	38 ± 5 cm
Strike-slip (cm)	85 ± 3 cm	86 ± 4 cm	93 ± 4 cm	65 ± 4 cm	11m ± 44 cm	65 ± 8 cm
Ground deformation range	-10 to 9 cm	-6 to 4 cm	-13 to 12 cm	-4 to 6 cm	-98 to 70 cm	-1 to 7 cm
Error range	-27 to 28 cm	-32 to 15 cm	-37 to 21 cm	-32 to 14 cm	-1 to 1 cm	-30 to 11 cm

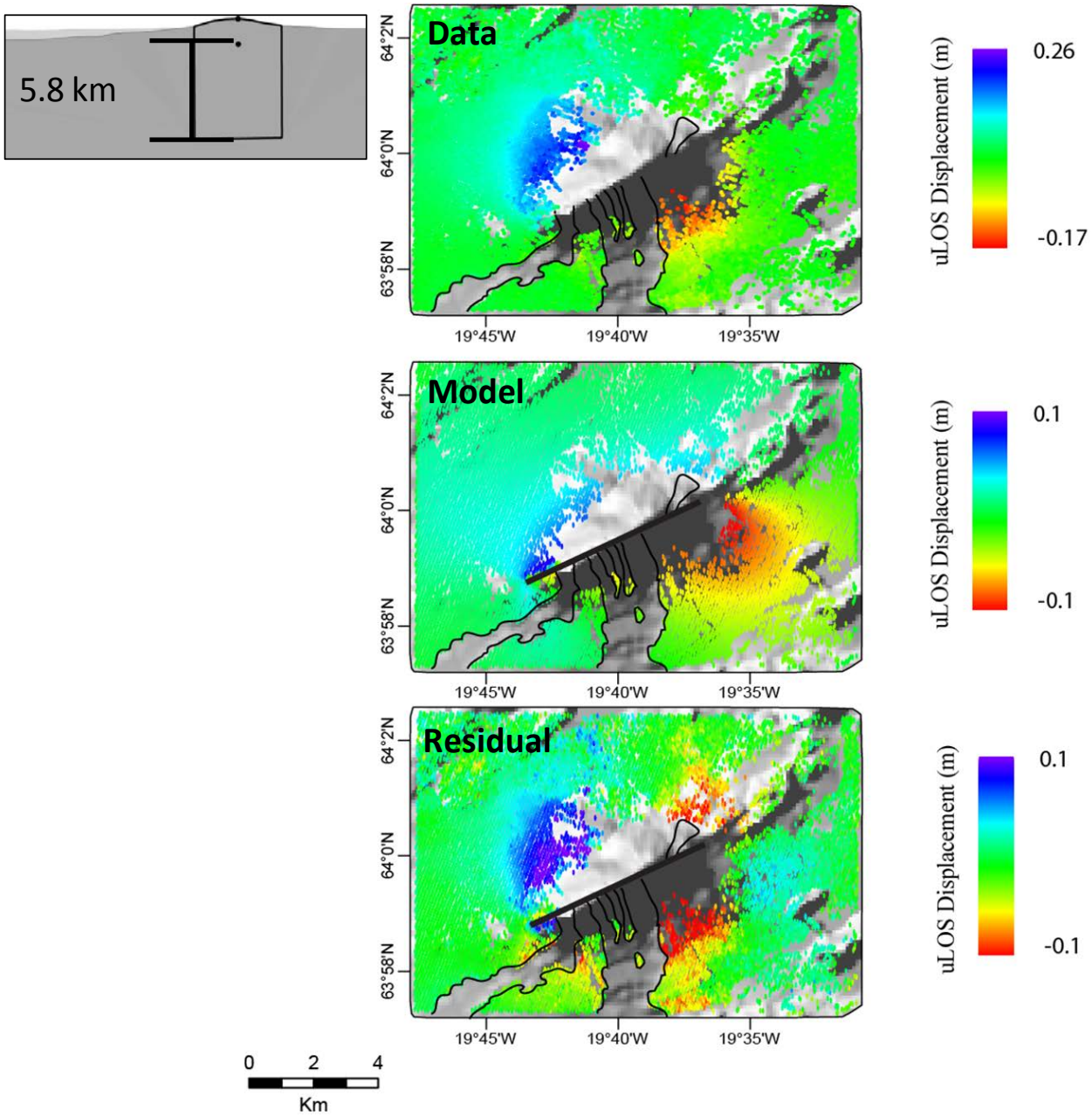

Figure 3.1. Results of Ts-5. Inset gives a zoomed-in view of the dike configuration. The Young's modulus for the model is 30 GPa, and the two black dots in the inset indicate the dike center; one on Hekla summit and the other at sea level. The top image is the InSAR data used, and the lava load is masked from the data, as indicated by black outlines in the figures. The dike is represented as a black line in the Model and Residual results. Strike and length of the dike is approximately to scale.

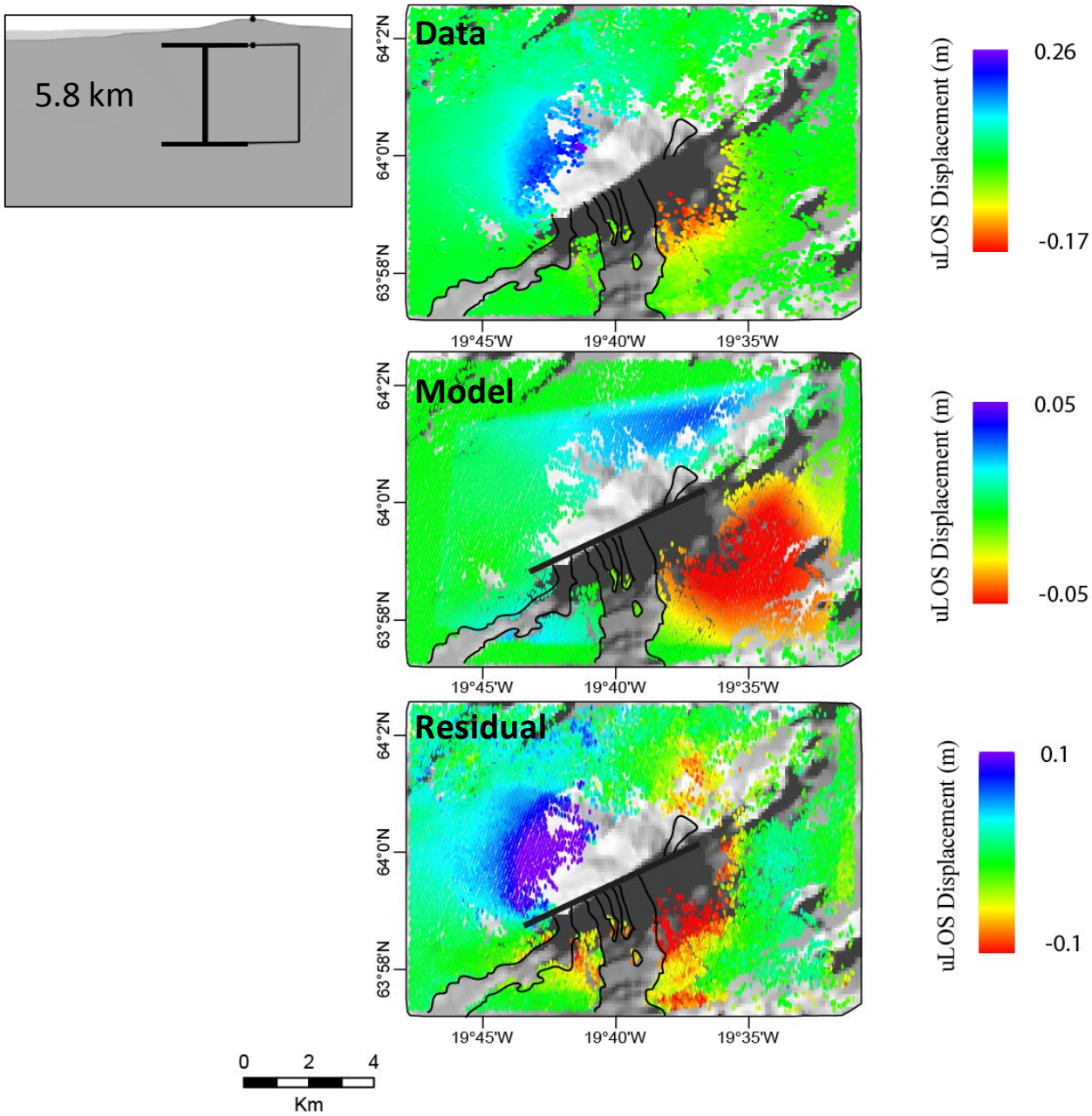

Figure 3.2. Results of Ts-5b. Inset gives a zoomed-in view of the dike configuration. The Young's modulus for the model is 30 GPa, and the two black dots in the inset indicate the dike center; one on Hekla summit and the other at sea level. The top image is the InSAR data used, and the lava load is masked from the data, as indicated by black outlines in the figures. The dike is represented as a black line in the Model and Residual results. Strike and length of the dike is approximately to scale.

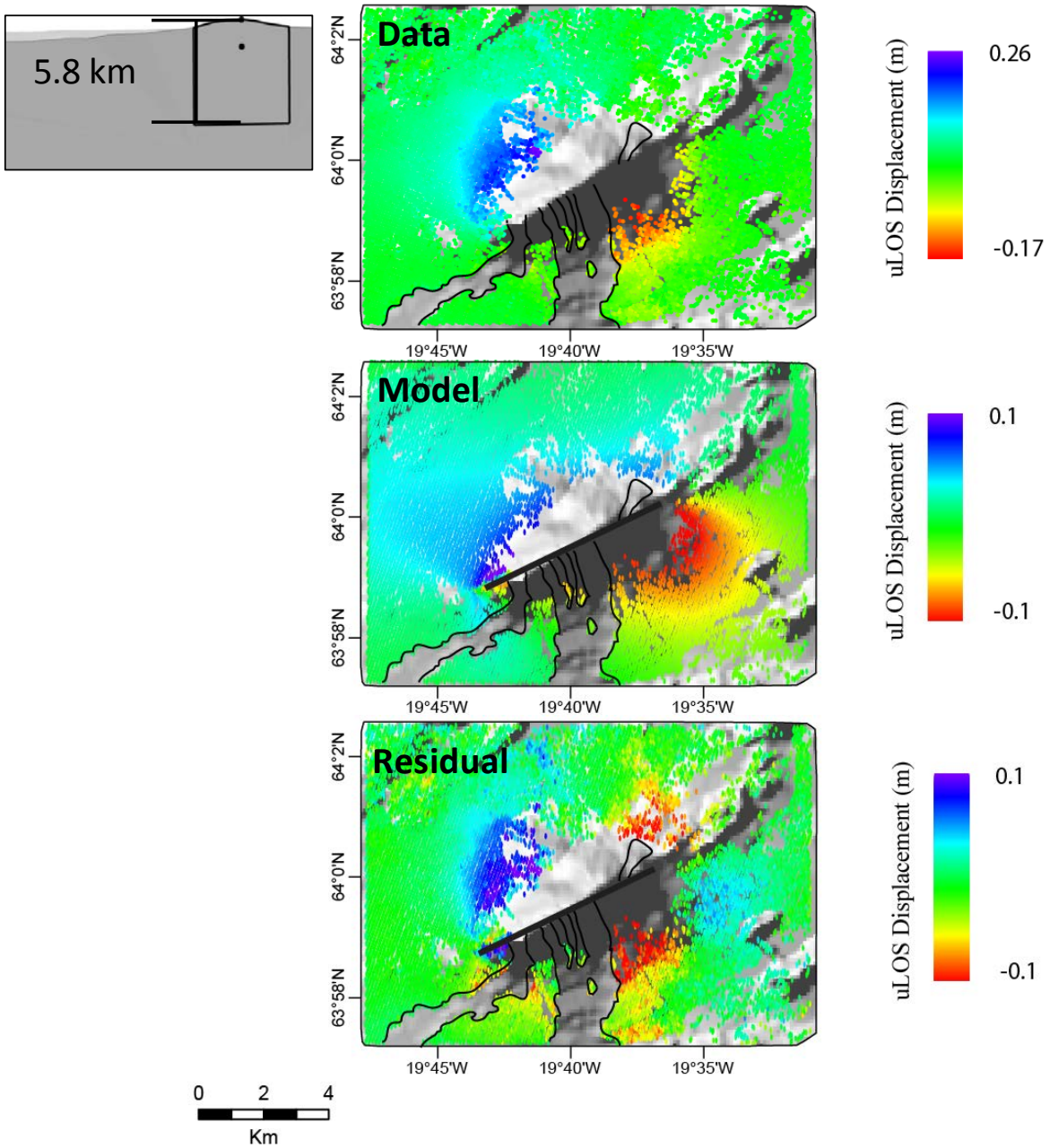

Figure 3.3. Results of Tt-5. Inset gives a zoomed-in view of the dike configuration. The Young's modulus for the model is 30 GPa, and the two black dots in the inset indicate the dike center; one on Hekla summit and the other at sea level. The top image is the InSAR data used, and the lava load is masked from the data, as indicated by black outlines in the figures. The dike is represented as a black line in the Model and Residual results. Strike and length of the dike is approximately to scale.

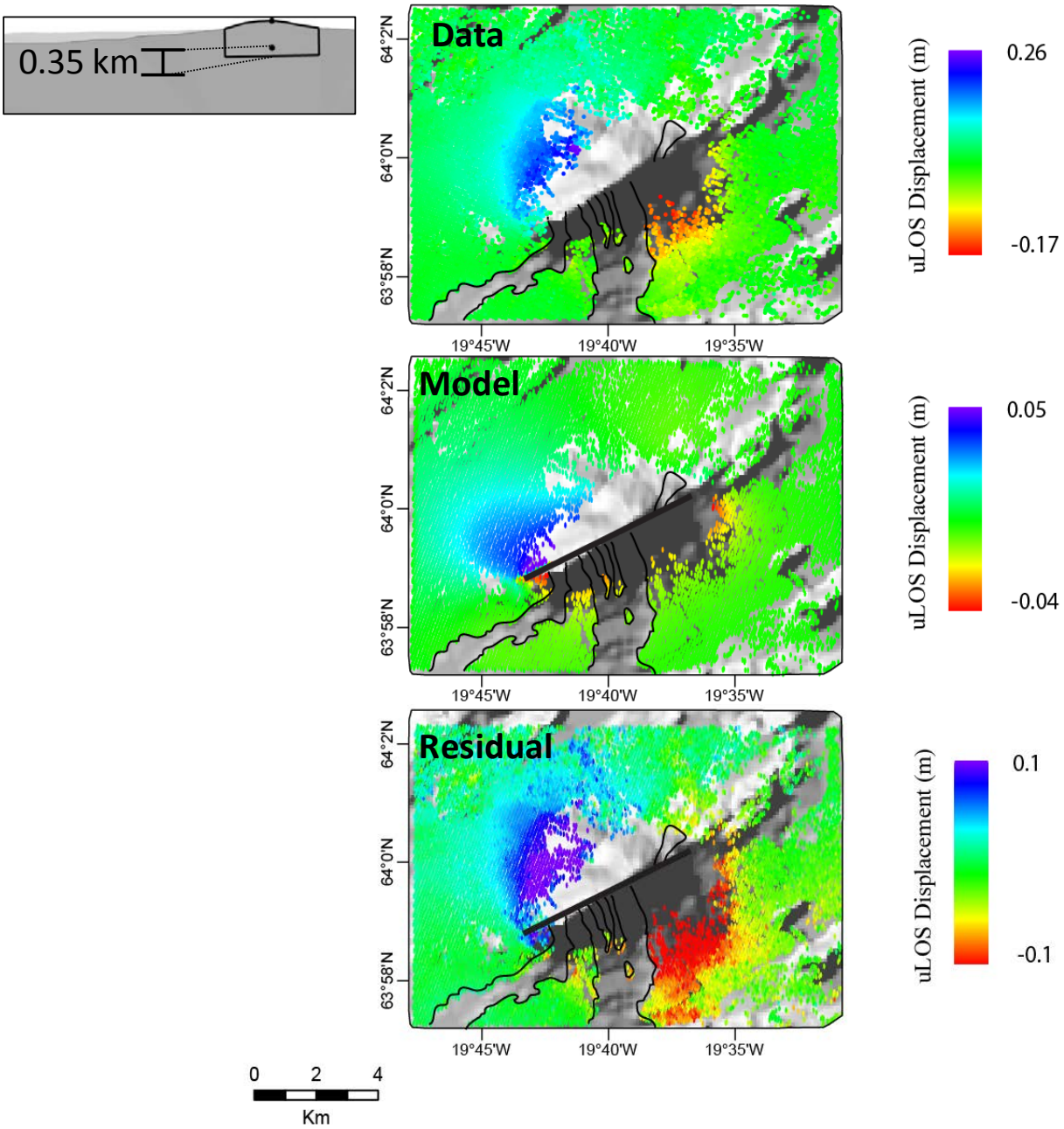

Figure 3.4. Results of Ts-3. Inset gives a zoomed-in view of the dike configuration. The Young's modulus for the model is 30 GPa, and the two black dots in the inset indicate the dike center; one on Hekla summit and the other at sea level. The top image is the InSAR data used, and the lava load is masked from the data, as indicated by black outlines in the figures. The dike is represented as a black line in the Model and Residual results. Strike and length of the dike is approximately to scale.

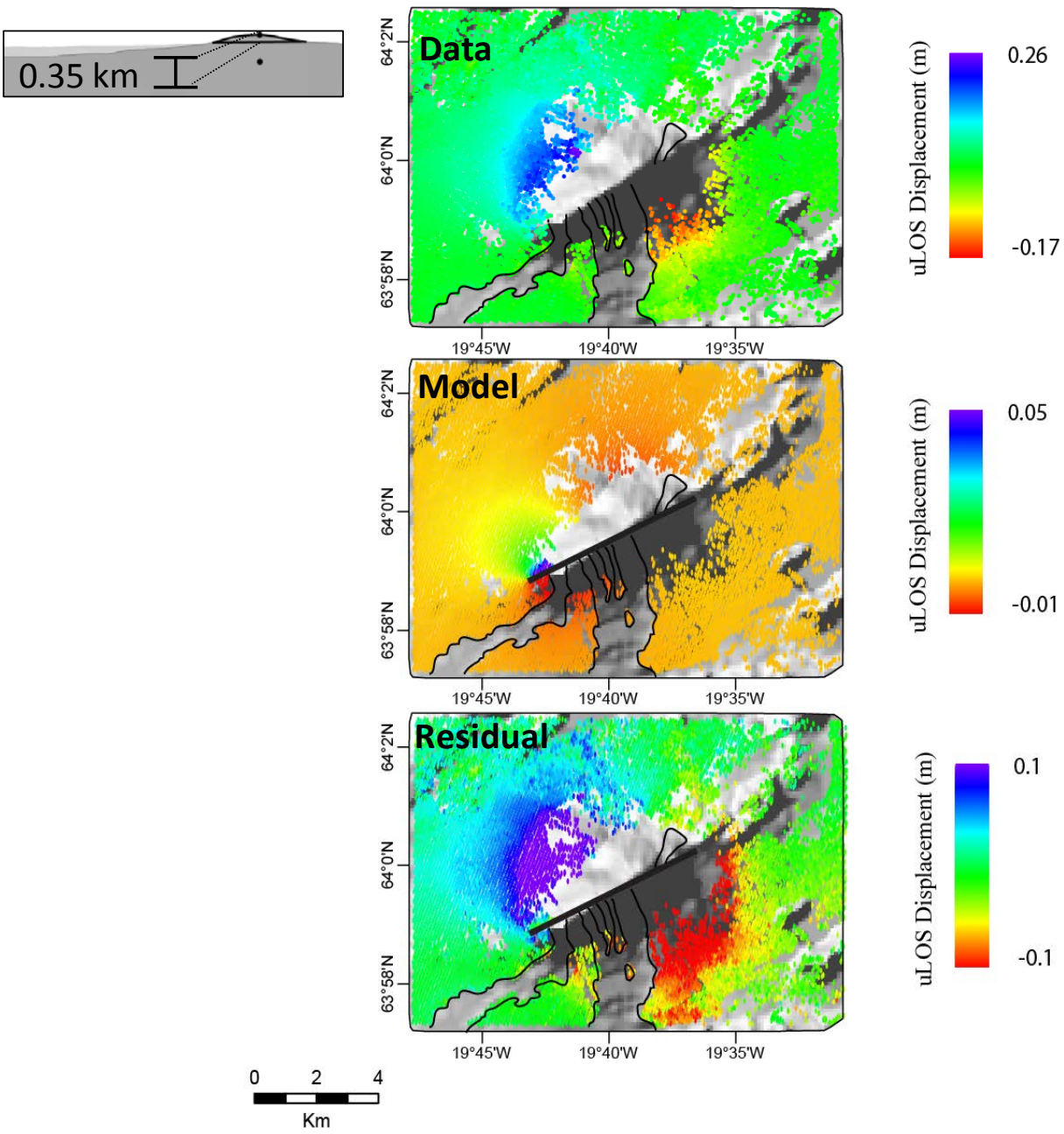

Figure 3.5. Results of Tt-3. Inset gives a zoomed-in view of the dike configuration. The Young's modulus for the model is 30 GPa, and the two black dots in the inset indicate the dike center; one on Hekla summit and the other at sea level. The top image is the InSAR data used, and the lava load is masked from the data, as indicated by black outlines in the figures. The dike is represented as a black line in the Model and Residual results. Strike and length of the dike is approximately to scale.

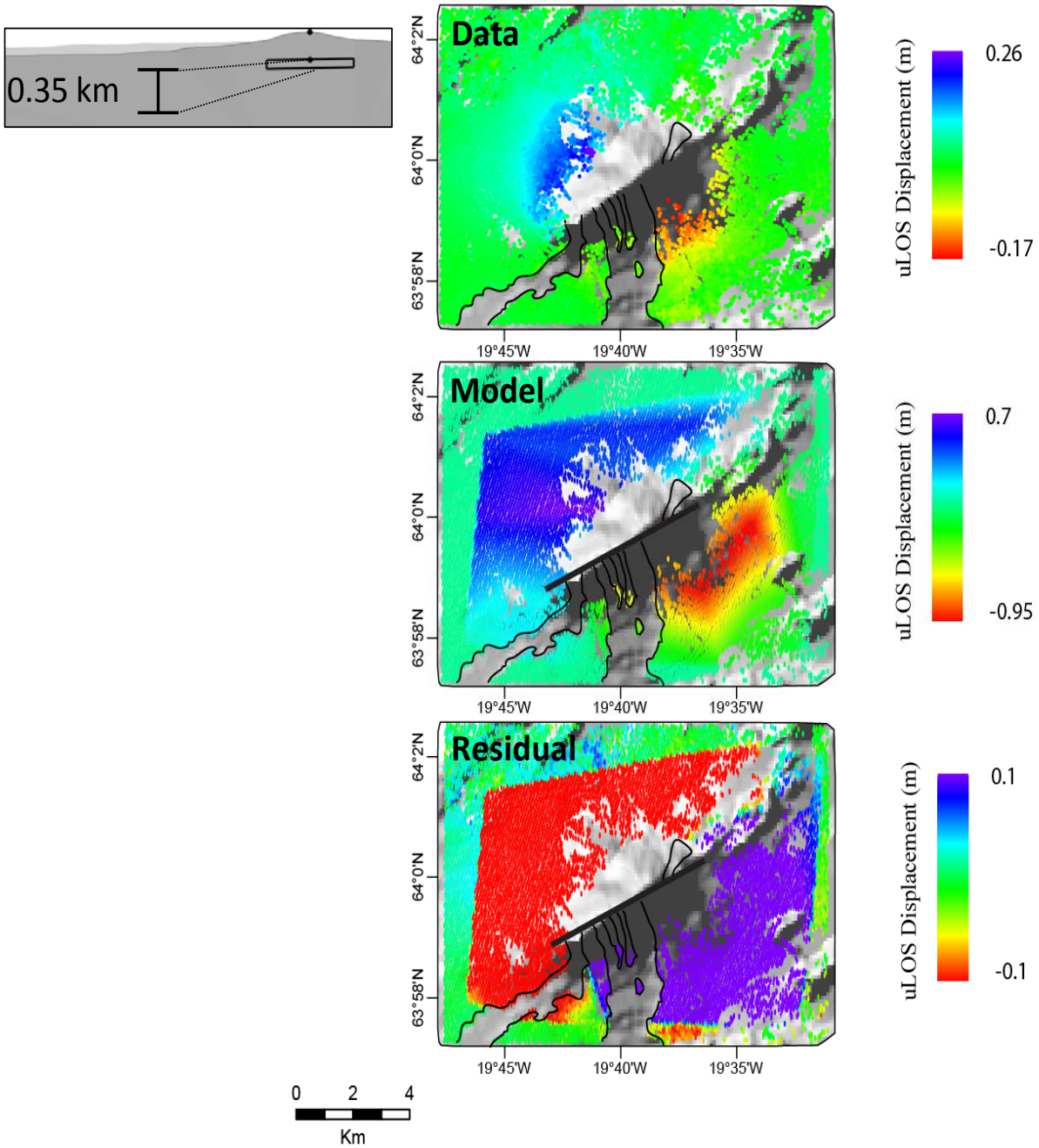

Figure 3.6. Results of Ts-3b. Inset gives a zoomed-in view of the dike configuration. The Young's modulus for the model is 30 GPa, and the two black dots in the inset indicate the dike center; one on Hekla summit and the other at sea level. The top image is the InSAR data used, and the lava load is masked from the data, as indicated by black outlines in the figures. The dike is represented as a black line in the Model and Residual results. Strike and length of the dike is approximately to scale.

predictions between the HEHS and FEMs is just between H-5 and the three FEM configurations using the 5.8 km dike. H-5 predicts 24-28 cm of dike opening while the FEMs predict opening

Table 3.2. Results of the two HEHS models. Although results of the smaller fissure with different rock properties can be inferred from equation 1.1, the alteration is included here for ease of comparison.

	H-5 (30 GPa Young's modulus)	**H-3 (14.3 GPa Young's modulus)**
Open (cm)	26 ± 2 cm	11 ± 5 cm
Strike-slip (cm)	64 ± 3 cm	1.18 m ± 10 cm
Ground deformation range	-7 to 5 cm	-31 to 37 cm
Error range	-16 to 19 cm	-33 to 40 cm

on the scale of 1-9 cm (including covariance ranges). The decrease in estimated opening of the FEMs is expected because adding topography decreases the amount of material at the top of the model domain being moved by the opening of the fissure relative to the direction of movement. The addition of topography also increases predicted strike-slip motion by 20-30 cm (Table 3.1-3.2).

All of the configurations of the 5.8 km wide dike predict approximately the same amount of opening as Ts-3, within covariance ranges, but 20-30 cm more strike-slip. Ts-3b predicts 16 cm of opening, but with a large covariance of 23 cm. The corresponding predicted strike-slip motion is also large, with an equally large covariance of 44 cm (Table 3.1). According to equation 2.6, the large covariance values are due to the extremely large magnitude of predicted deformation values compared to the size of the InSAR data (Figure 1.2).

If blind fissures are disregarded, generally dike area has a positive relationship with estimated strike-slip motion on the dike: as dike area decreases, so does estimated strike-slip. The opposite is true for opening: the smallest dikes predict the biggest opening. Ts-5b predicts

the same movement as Ts-5, but Ts-3b predicts different movements from any model configuration.

2. Discussion

The decrease in estimated opening of the dike compared to the equivalent HEHS configuration is likely a function of the shape of the volcano relative to the orientation of the dike and movement along it. Decreased opening is expected because the fissure is a ridge; the amount of material perpendicular to the dike in the FEM is much less than the amount of material perpendicular to a dike embedded in a HEHS. The amount of material parallel to the dike, however, is relatively the same in the two approaches, and the shape of Hekla does not seem to be the biggest determining factor in the dominance of strike-slip. If it were, there should be a correlation between strike-slip movement, and the relative amount the dike is embedded in the volcano, but that is not the case. Model Ts-5 predicts less strike-slip than Tt-5, but less of the dike (as a percentage of total dike width) is in the edifice of Hekla in Ts-5, suggesting that strike-slip estimates should decrease as fissure length increases, but estimates of strike-slip from all topographic models (regardless of fissure length) indicate the opposite relationship. Model Tt-3, predicts the same amount of strike-slip as Ts-3, even though the two configurations have different percentages of the dike contained within the volcano. Therefore, some other factor may be controlling the predicted contribution of strike-slip.

The strong strike-slip component in the estimates from both the HEHS and the topographic FEM support the notion from Soosalu and Einarsson (2005) that Hekla is located more in the SISZ rather than the EVZ. Dip-slip movement is not accommodated in the models, so indications of any faulting similar in style to the “book shelf” faulting of the SISZ are not

available, but the overall tendency towards strike-slip solutions from the models indicate shear stresses, not tensile stresses, are defining the behavior of the fissure during an eruption, especially when topography is included in the model domain.

The relatively strong component of strike-slip motion predicted by the topographic FEMs of Hekla could also have implications for the strike of the dike at depth (Pedersen, personal comm). Acocella and Neri (2009) suggest that dike propagation in areas without topography is usually controlled by regional tectonic stresses, while dike propagation within volcanic edifices seems to be controlled more by the shape (Fiske and Jackson, 1972) and topography of the edifice, as well as the local stress conditions. Hekla's ridge and fissure are not well aligned with the general trend of rifting in the EVZ (Soosalu and Einarsson, 1997, 2005) nor with faults in the SISZ, even though the regional stresses of the SISZ are likely affecting Hekla (Gronvöld et al., 1983; Soosalue and Einarsson, 2005). This could be due to a change in the controlling factor of the dike orientation, from regional stresses to stresses associated with the topography of Hekla, which may change the strike of the fissure at depth. If this is the case, the strength of the different components of movement (i.e. strike-slip and opening) along a dike with the same strike at all depths should change with depth to compensate for the directional constraint of the fissure.

The predictions of model Ts-3 are going to be dominated by the edifice of the volcano, which is 4 times as tall as the depth of that dike. The fact that a model of a dike embedded at the very top of the volcano predicts a similar amount of strike-slip as Tt-3 (i.e. a model in which the dike passes completely through the edifice and just barely extends below sea level) indicates three things: (1) the dike orientation does not change at all within the volcano, or (2) the dike orientation changes only a very small amount, or (3) the orientation changes at or near the

bottom of the volcano, or a combination of the above. Such a change in strike could extend down past sea level for the full length of the rest of the dike or, possibly, change again at depth. The increase in predicted strike-slip from the configurations of the 0.35 km dike to configurations of the 5.8 km dike supports the notion of a change in strike near or below the bottom of the volcano, because the predictions of those longer dikes are influenced more by the geometry of the fissure at depth rather than the geometry within the volcano edifice.

The differences in the strike-slip component of the different configurations can shed some light on how far down a change in strike may extend, as well as the number and magnitude of changes. Ts-3 predicts about 30 cm less strike-slip motion than Tt-5, indicating a relatively large change in strike may occur somewhere between the bottom of the Ts-3 dike and the bottom of the Tt-5 dike, but model Ts-5 predicts only 20 cm more strike-slip than Ts-3. These predictions are hard to reconcile, because they indicate the configuration of Ts-3 is closer to Ts-5 than to Tt-5, even though any change in strike between Ts-3 and Tt-5 should carry through to Ts-5, unless there is a second change in strike.

The predictions of the blind dikes, however, can clarify the discrepancy because they isolate the areas under the volcano. Those predictions indicate only one change in strike within the very bottom parts of the volcano and/or upper portions of the crust at depth. The predictions from Ts-5b indicate the orientation of the dike beneath the edifice is generally the same as the entire width of the dike in Ts-5. The prediction from Ts-3b, however, indicates there could be a change in the strike just at or slightly below sea level. Even a slight change in strike could cause the drastic differences in predictions if the change happens above the dike in Ts-3b such that the entire dike has a different orientation. If this change in strike is relatively minor, the predictions from Ts-5 and Ts-5b could still be the same because the dikes in those two configurations extend

down to 7.25 km depth, while the volcanic edifice is only 1.45 km above sea level. Thus, even if the orientation of the upper 1.45 km of the dike were different from the bottom 5.8 km, the overall orientation could still be quite similar, as long as any change in strike is relatively small. Because Tt-5 has a higher percentage of the dike within the edifice, this change in strike could affect the predictions more than the longer dike in Ts-5.

If the results of the model are due to a change in strike of the dike, there has to be geologic reasons which could cause such a change. Volcanoes build topography through a combination of erupted material piling up and internal growth (Biggs et al., 2010). Hekla's topography is mainly a result of a build-up of lava and ash from its extensive eruption history, and the volume of material expelled from Hekla through time provide more than enough material to build the volcano up to its present volume (Sigmundsson, 2006; Sigvaldason, 1967).

Aside from regional stresses or local loading stresses, the properties and orientation of the materials through which a dike propagates affect the direction of propagation (Acocella and Neri, 2009; Giberti and Wilson, 1989; Gudmundsson et al., 1999, Gudmundsson, 2002). Conversely, the orientation of the dike and steepness of the slope should affect the orientation and thicknesses of the lava flows emitted from the eruptive fissure. Thus, the historical orientation of an eruptive fissure could be recorded by the orientation of the layers of lava emitted. Orientation of tephra and other airborne materials, however, is influenced by many other things such as fragmentation, meteorological conditions, eruption column dynamics and particle sizes (Gronvold et al., 1983; Swindles et al., 2011; Thorarinsson and Sigvaldason, 1971). Therefore, the layers of Hekla alternate between lavas controlled by factors related to the eruptive fissure orientation and tephra controlled by factors not related to the eruptive fissure orientation. This layering could provide local stresses oriented differently than regional stresses. Initially, the eruptive fissure orientation

is controlled by regional stresses, and this orientation determines, to some extent, the orientation of the lavas but not the tephras. At some point, the build-up of topography could cause the layering and topographic edifice to become the dominant control on the orientation of the eruptive fissure. Thus, a change in eruptive fissure orientation within the lower edifice of the volcano is geologically plausible, especially at a volcano which is one of the most active in Iceland and has produced more tephra than any Icelandic volcano in the last 11,000 years (Thorarinsson and Sigvaldason, 1971; Swindles et al., 2011).

Another aspect highlighted by including topography is the possibility of a configuration where the dike in a model never intersects sea level, but still intersects the free-surface of the model domain. Topographic corrections cannot recreate or compensate for such a model configuration, but recent results for the geometry of the Hekla dike from strain data associated with the 2000 eruption (Sturkell et al., 2013) indicate the dike under Hekla is likely less than 0.5 km wide, which is about one third of the total elevation of the volcano. A study at Piton de la Fournaise (Fukushima et al., 2010) has found the best-fit dike geometry for several eruptions at that volcano never extends more than halfway into the volcanic edifice. The dike intersects the surface in a saw-tooth pattern along a slightly curved fissure. Such geometry is simply not possible with a HEHS and topographic corrections. The saw-tooth pattern configuration is worth consideration at Hekla because of the timing in activation of different parts of the fissure during the past several eruptions (Gronvold et al., 1983; Hoskuldson et al., 2007; Linde et al., 1993; Thorarinsson and Sigvaldason, 1972). These configurations deserve investigation and can be explored with a topographic FEM, but they simply cannot be explored with the modeling techniques employed by Ofeigsson et al. (2011) and Sturkell et al. (2013).

LAYERED ELASTIC HALF-SPACE MODEL

1. Results

An FEM is modified to simulate HEHS assumptions to test the sensitivity of deformation predictions to material properties distributed as a LEHS. Two main configurations of layering are investigated using the same two dike widths from the topographic FEM. One layering configuration uses four layers: the first three layers are 1 km thick each, while the fourth layer comprises the rest of the domain (Figures 2.13, 2.15, 2.17). This configuration of the 5.8 km dike is called L-5.1. The models using this configurations of the 0.35 km dike are L-3.1 and L-3.1Y12. The second model name indicates the Young's modulus of the upper layer is 12.8 GPa, rather than the Young's modulus of the top layer used by the other two configurations (i.e. 14.3 GPa). The other layering configuration is designed to have five layers total: the first two layers are 0.5 km thick, the next two layers are 1 km thick, and the fifth layer comprises the rest of the model domain (Figures 2.14 and 2.16). The configurations of the 5.8 km and 0.35 km dike are called L-5.2 and L-3.2, respectively. Model L-3.2, however, had to have a different layer thickness for the top two layers due to partitioning issues in Abaqus. The top layer in this configuration is 0.35 km and the second layer is 0.65 km thick.

The results for the different LEHS model configurations are summarized in Table 3.3, and deformation predictions and residuals for the forward models are shown in Figures 3.7-3.11. Most of the predicted movements are very similar, but the differences are highlighted here. The predicted movements of L-5.1 are no different (within the variance) than the predicted movements of H-5 (Table 3.2). The predicted strike-slip for L-5.2 is also the same, but the amount of predicted opening is larger by about 7 cm. The results for L-3.1 are different from H-3 (Figure 3.12), despite having a fissure embedded in a material with the same properties.

Table 3.3. Summary of results for the LEHS FEM. The first three columns are results for LEHS models with 1 km thick layers. The second two columns are results for LEHS models with the top layer split into two layers with different rock properties.

	L-5.1	**L-3.1**	**L-3.1Y12**	**L-5.2**	**L-3.2**
Open (cm)	28 ± 2 cm	22 ± 6 cm	22 ± 6 cm	35 ± 2 cm	17 ± 6 cm
Strike-slip (cm)	60 ± 3 cm	1.96 m ± 13 cm	1.94 ± 14 cm	60 ± 4cm	1.81 m ± 13 cm
Ground deformation range	-7 to 4 cm	-34 to 46 cm	-33 to 44 cm	-3 to 4 cm	-31 to 38 cm
Error range	-16 to 19 cm	-41 to 43 cm	-40 to 42 cm	-22 to 19 cm	-34 to 39 cm

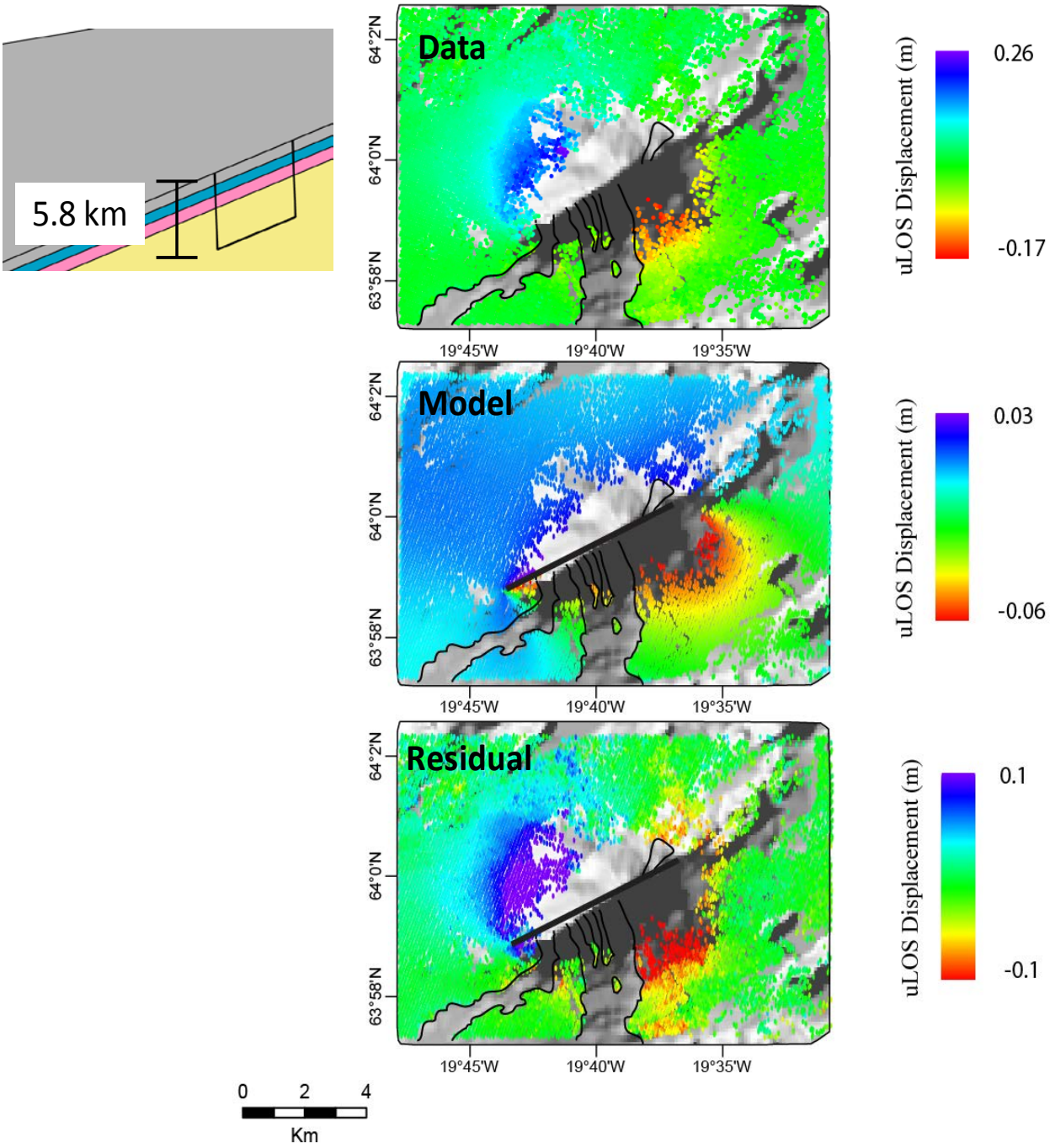

Figure 3.7. Results L-5.1. Inset gives a zoomed-in view of the dike and layering configuration. The Young's modulus for the grey layer is 14.3 GPa, blue layer is 27.7 GPa, pink layer is 33.5 GPa, and yellow layer (i.e. the rest of the model domain) is 30 GPa (Table 2.2). The top image is the InSAR data used, and the lava load is masked from the data, as indicated by black outlines in the figures. The dike is represented as a black line in the Model and Residual results. Strike and length of the dike is approximately to scale.

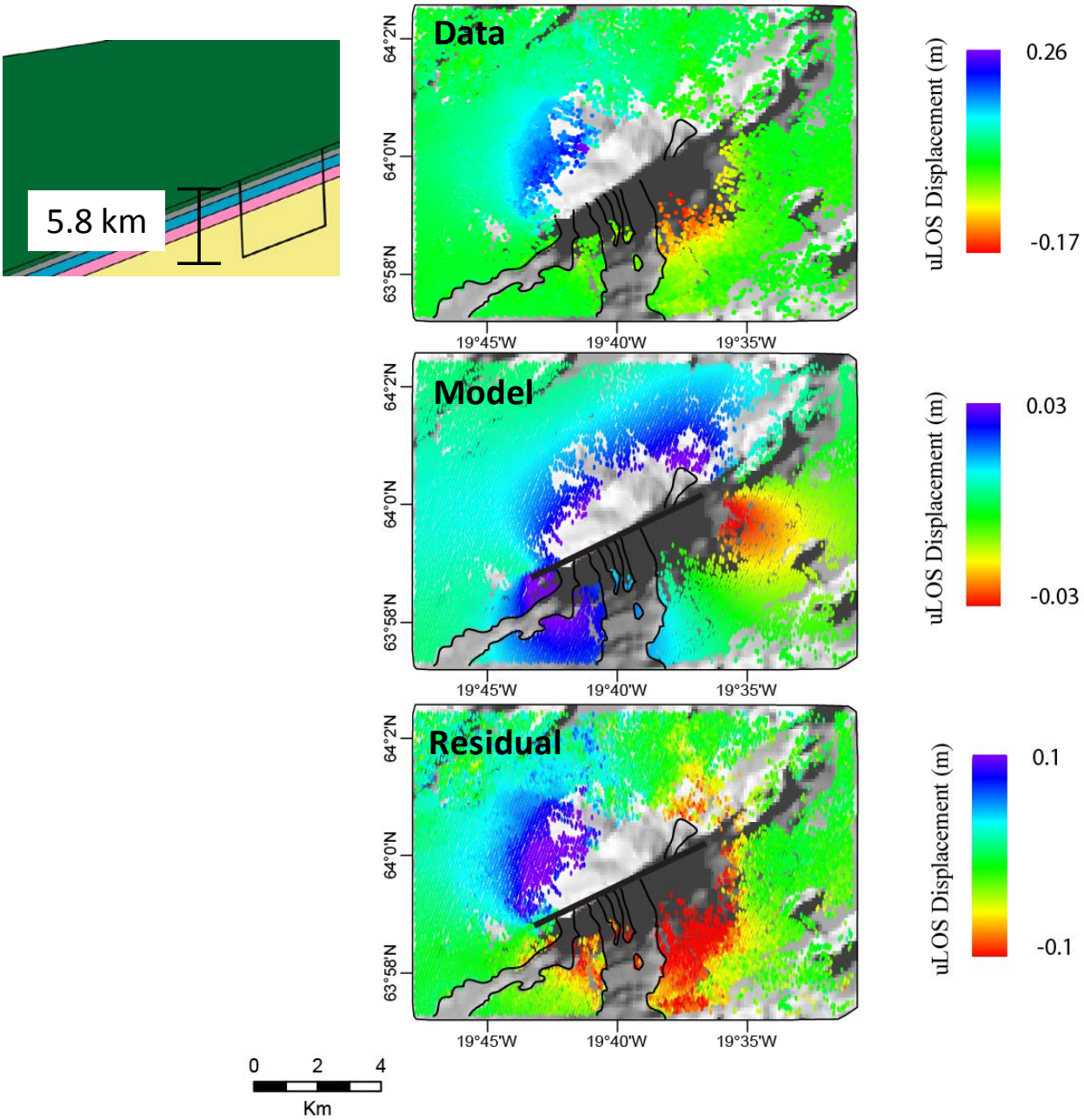

Figure 3.8. Results L-5.2. Inset gives a zoomed-in view of the dike and layering configuration. The Young's modulus for the green layer is 12.8 GPa, grey layer is 14.3 GPa, blue layer is 27.7 GPa, pink layer is 33.5 GPa, and yellow layer (i.e. the rest of the model domain) is 30 GPa (Table 2.3). The top image is the InSAR data used, and the lava load is masked from the data, as indicated by black outlines in the figures. The dike is represented as a black line in the Model and Residual results. Strike and length of the dike is approximately to scale.

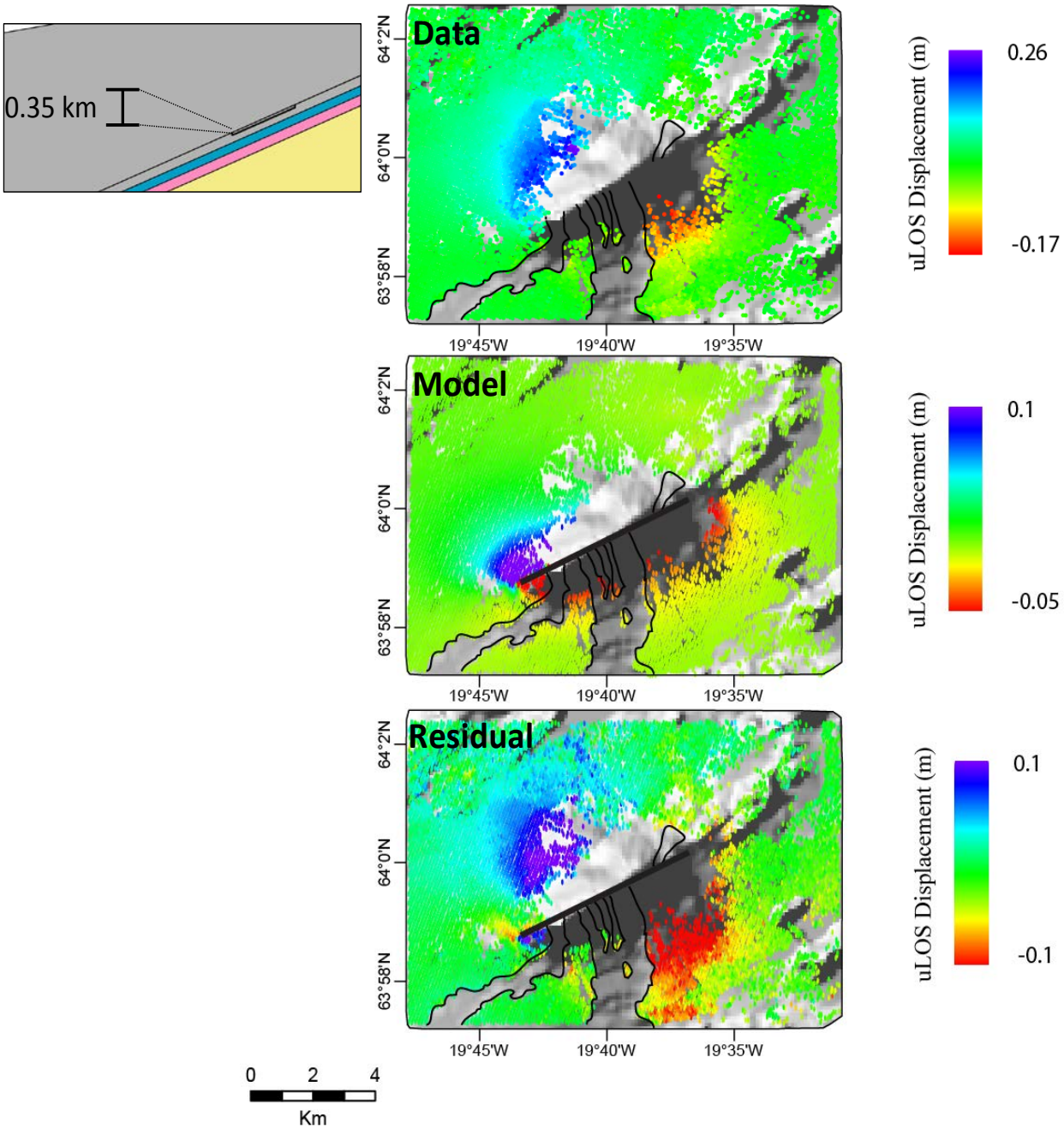

Figure 3.9 Results L-3.1. Inset gives a zoomed-in view of the dike and layering configuration. The Young's modulus for the grey layer is 14.3 GPa, blue layer is 27.7 GPa, pink layer is 33.5 GPa, and yellow layer (i.e. the rest of the model domain) is 30 GPa (Table 2.2). The top image is the InSAR data used, and the lava load is masked from the data, as indicated by black outlines in the figures. The dike is represented as a black line in the Model and Residual results. Strike and length of the dike is approximately to scale.

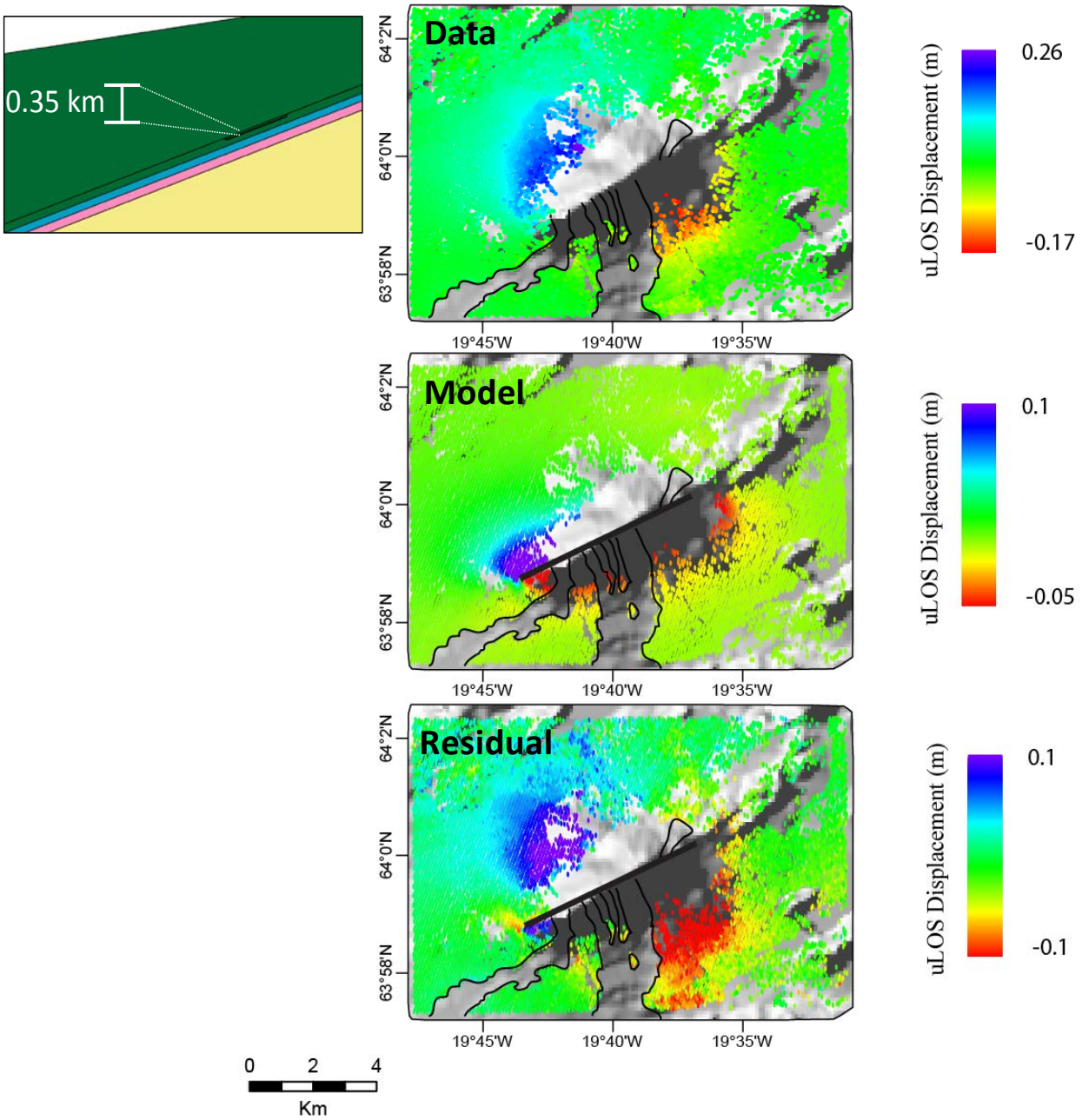

Figure 3.10. Results L-3.1Y12. Inset gives a zoomed-in view of the dike and layering configuration. The Young's modulus for the green layer is 12.8 GPa, blue layer is 27.7 GPa, pink layer is 33.5 GPa, and yellow layer (i.e. the rest of the model domain) is 30 GPa (Table 2.2). The top image is the InSAR data used, and the lava load is masked from the data, as indicated by black outlines in the figures. The dike is represented as a black line in the Model and Residual results. Strike and length of the dike is approximately to scale.

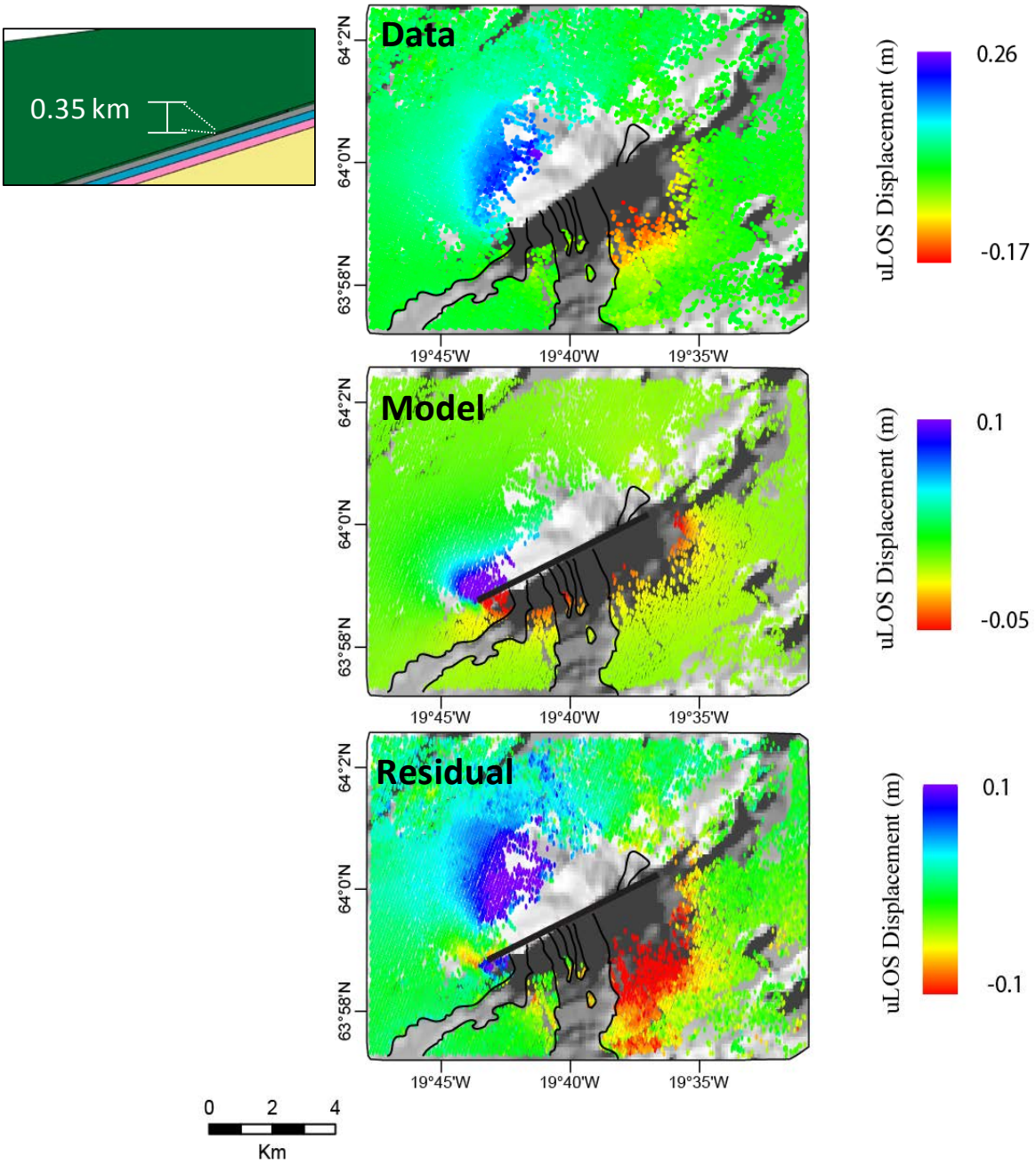

Figure 3.11. Results L-3.2. Inset gives a zoomed-in view of the dike and layering configuration. The Young's modulus for the green layer is 12.8 GPa, grey layer is 14.3 G Pa, blue layer is 27.7 GPa, pink layer is 33.5 GPa, and yellow layer (i.e. the rest of the model domain) is 30 GPa (Table 2.3). The top image is the InSAR data used, and the lava load is masked from the data, as indicated by black outlines in the figures. The dike is represented as a black line in the Model and Residual results. Strike and length of the dike is approximately to scale.

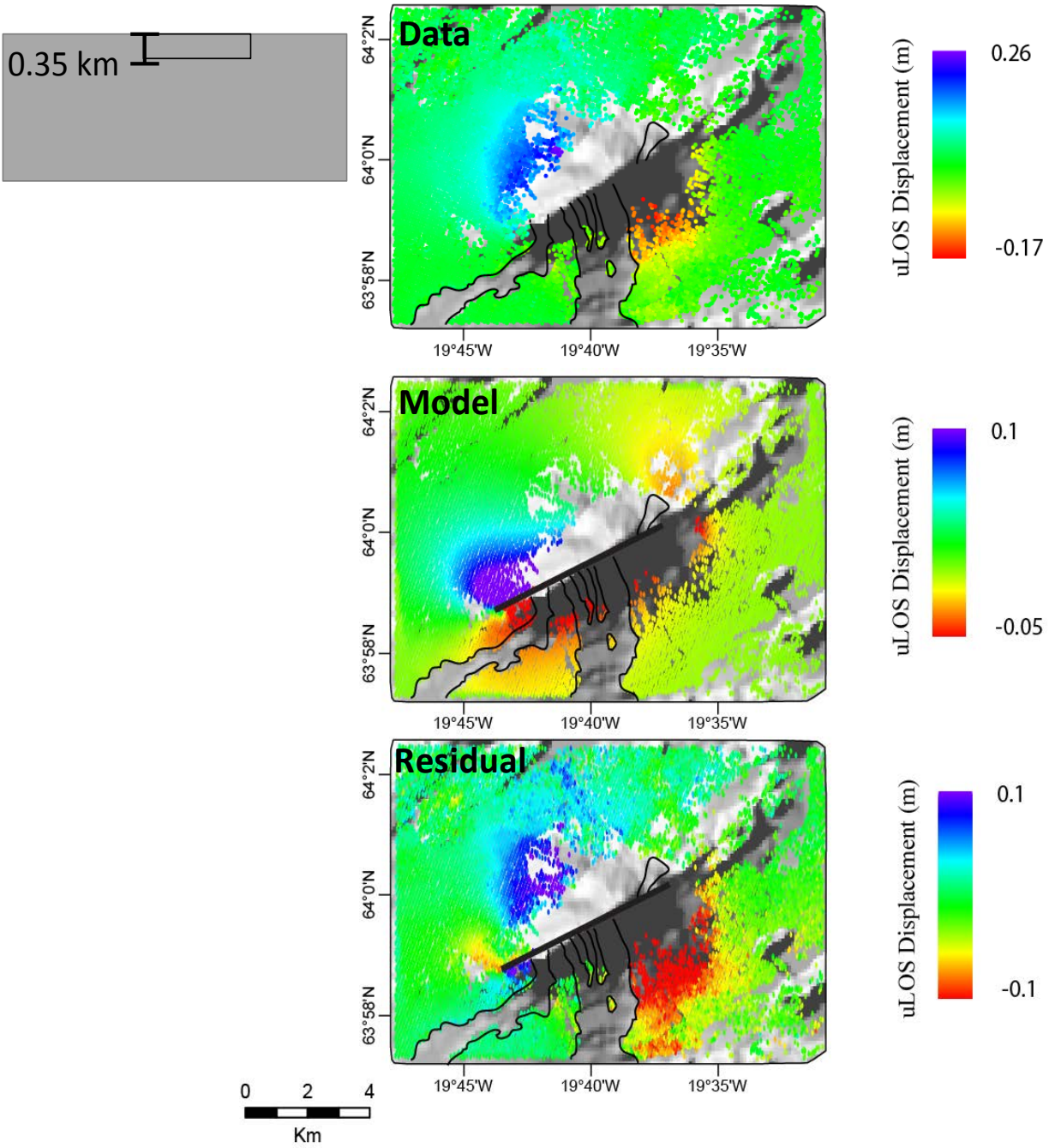

Figure 3.12. Results H-3. Inset gives a zoomed-in view of the dike configuration. The Young's modulus for this configuration is 14.3 GPa. The top image is the InSAR data used, and the lava load is masked from the data, as indicated by black outlines in the figures. The top image is the InSAR data used, and the lava load is masked from the data, as indicated by black outlines in the figures. The dike is represented as a black line in the Model and Residual results. Strike and length of the dike is approximately to scale.

2. Discussion

The similarities and differences between L-5.1 and H-5 indicate a relationship between the method in which the dike is allowed to move and the predicted movements of the fissure. Model L-5.1 has different properties for the top 3 km of the problem domain than model H-5, but the lower 22 km are the same. This similarity in the majority of the problem domain, even though it is away from the surface, appears to be the controlling factor on the predictions of the two models. The 5.8 km dike penetrates all the layers, including the lower portion of the model domain. Although most of the dike is in the upper 3 km of the LEHS model, only the uppermost 1 km of the problem domain has a Young's modulus that is much different than the Young's modulus used in the HEHS model. This configuration, combined with the uniform displacement constraint placed on the fissure, could explain why H-5 and L-5.1 predict the same dike movement.

The relative increase of 7 cm in estimated opening for L-5.2 compared to L-5.1 (Table 3.3) is interesting. In general, a material with a lower Young's modulus should require less stress to produce the same amount of strain. Therefore, lowering the Young's modulus of the uppermost 0.5 km of the problem domain should either not affect the results at all (following the premise that uniform opening prevents the layers from interfering with dike movement), or should lower the amount of estimated opening required to recreate the observed deformation. The deformation estimates (Figures 3.7-3.8) from the two configurations, however, indicates the layer with a lower Young's modulus does not transmit the deformation across the surface as well as the layer with a higher Young's modulus. Thus, even though there should be less stress to produce the same amount of strain directly at the site of the load (i.e. the fissure), the strain is not transmitted throughout the material as effectively in a material with a lower Young's modulus.

Because the data are incoherent directly along the expression of the eruptive fissure, only deformation data which is farther out from the site of the load is available. The inability of the material to effectively transmit stress and the lack of data directly on the fissure yields a predicted opening which is greater than expected, even though the upper material is weaker and there is a constraint of uniform movement along the dike. These results indicate there may be a "tipping point" in the role material properties, width and movement of the dike, and layer thickness and proximity to the top of the model domain has in predicting fissure behavior given the constraint of uniform displacement.

Model L-3.1 has the same Young's modulus for the top layer in as the entire problem domain for H-3, while the top layer of L-3.1Y12 has a slightly lower Young's modulus than H-3. Model L-3.1 and L-3.1Y12 predict the same dike movement, but that dike movement is different than the predicted movement of H-3 (Tables 3.3 and 3.2). The relationship between the top layer the subsequent layers could be affecting the movement of the fissure, even though the fissure never crosses those layers.

The surface deformations predicted by the models, however, demonstrate the difference between the configurations. Model L-3.1 predicts a similar pattern of ground deformation as H-3 (Figures 3.9 and 3.12). Model L-3.1Y12 (Figure 3.10) also predicts a similar range of deformation as L-3.1 (Table 3.3), but the deformation drops off quickly with distance away from the fissure as well as in model L-3.2 (Figure 3.11). This pattern is also seen in model L-5.2 compared with L-5.1. These results indicate the upper layer may affect ground deformation predictions, while the bottom layers have a larger role in the predicted fissure movement, even in dikes that are not long enough to cut though the lower layers.

A relationship exists between fissure width, layer thickness and properties, and dike opening. The strike-slip predictions for the models seem more dependent on fissure width, although the strike-slip L-3.2 is 13-15 cm smaller than the strike-slip predicted for L-3.1 and L-3.1Y12, this change is just within the covariance of the predictions. In general, the configuration of the top two layers is not more influential on the predicted dike movement than the complete layering configuration of the model, although a wider (i.e. deeper) dike may predict bigger opening if the uppermost sections of the model have a lower Young's modulus. The predicted opening for a dike completely embedded in the top layer is still dependent on the properties of the layers below. The predicted ground deformations, however, are more dependent on the properties of the uppermost layer, although a second layer, which is very close to the top, may influence the deformation pattern.

LAYERED TOPOGRAPHIC FEM

1. Results

The results of the layered topographic FEMs are quite variable and command a more thorough review than the previous configurations. The results are summarized in Table 3.4, and predicted deformations and residuals are shown in Figures 3.13-3.17 but some interesting patterns are pointed out here. Model LTs-5.1 predicts approximately the same fissure movement as L-5.1 and H-5 (Tables 3.3 and 3.2, respectively), but 20 cm less strike-slip motion and 10 times greater opening than Ts-5. The deformation predicted by LTs-5.1 is between -4 and 10 cm, which is much smaller than the range of deformation (about -30 to 35 cm) for L-5.1 or H-5, but closer to Ts-5.1, which predicts deformation ranging between -10 and 9 cm.

Table 3.4. Summary of results for the layered topographic FEM. Columns are organized by thickness of the top layeyer; "full" means the top layer extends from the summit of Hekla down to 1 km below sea level (i.e. about 2.4 km total thickness), "half" means the top layer is 0.5 km thick and embedded in the top of Hekla. The second layer for these models still extends down to 1 km below sea level, for a total thickness of 2 km. The column label including "0.5 km fissure from summit" indicates that fissure starts at the summit of Hekla and extends 0.5 km from the summit. The bottom of this fissure is roughly 1.4 km above sea level.

	LTs-5.1	**LTs-5.1b**	**LTs-5.2**	**LTs-3.1**	**LTs-3.2**	**LTt-3.2**	**LTs-3.1b**
Open (cm)	29 ± 2 cm	15 ± 3cm	16 ± 2 cm	30 ± 5 cm	45 ± 5 cm	64 ± 10 cm	97 ± 24cm
Strike-slip (cm)	61 ± 3 cm	53 ± 4 cm	64 ± 3 cm	1.5 m ± 8 cm	1.2 m ± 8 cm	2.07 m ± 15 cm	13.13 m ± 55 cm
Ground deformation range	-5 to 10 cm	-2 to 4 cm	-5 to 11 cm	-21 to 50 cm	-11 to 30 cm	-33 to 79 cm	-1.16 to 1.87 cm

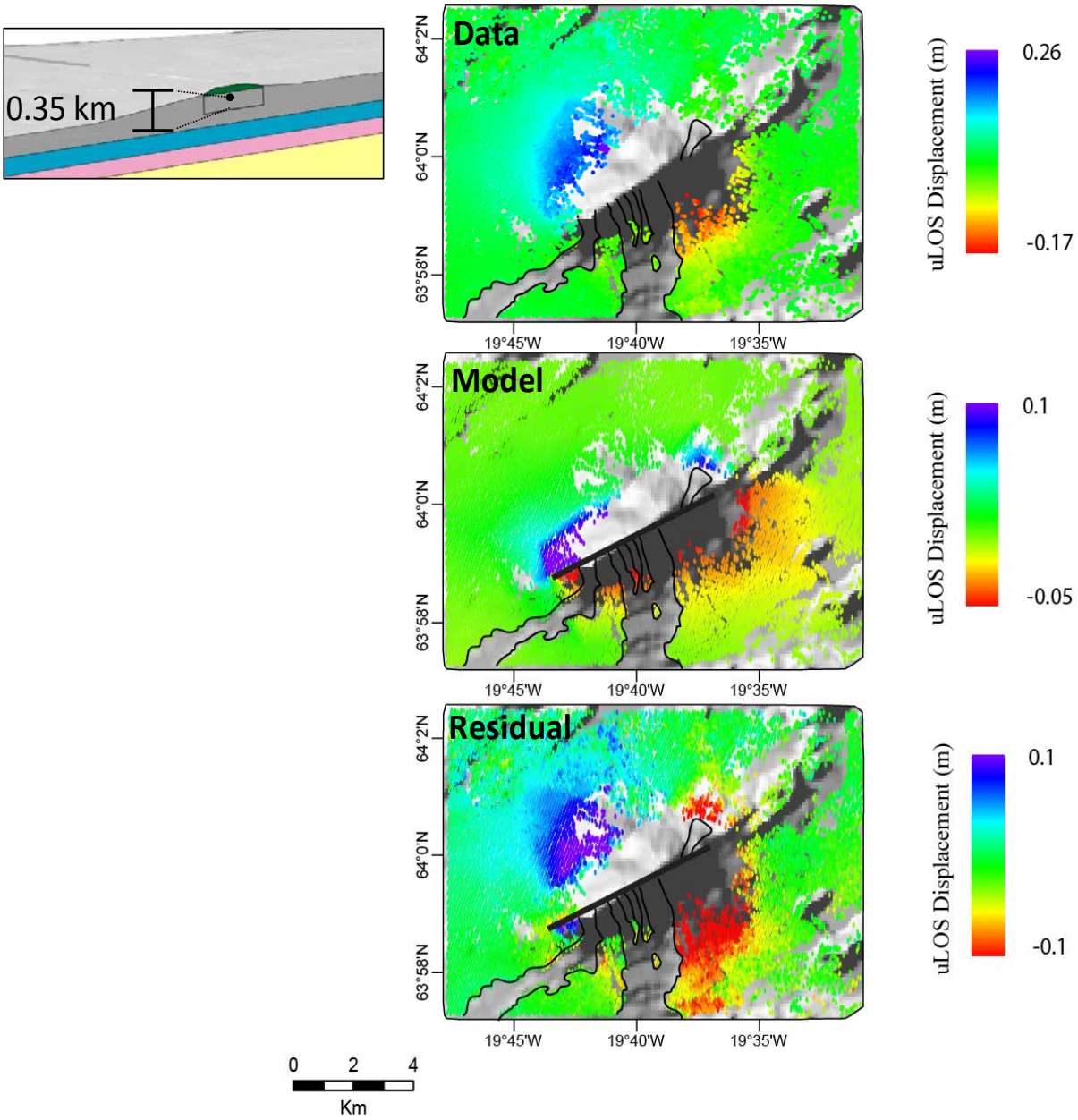

Figure 3.13. Results of LTs-3.2 (inset). The Young's modulus for the green layer is 12.8 GPa, grey layer is 14.3 GPa, blue layer is 27.7 GPa, pink layer is 33.5 GPa, and yellow layer (i.e. the rest of the model domain) is 30 GPa (Table 2.3). The black dot in the inset indicates sea level under the dike center. The top image is the InSAR data used, and the lava load is masked from the data, as indicated by black outlines in the figures. The dike is represented as a black line in the Model and Residual results. Strike and length of the dike is approximately to scale.

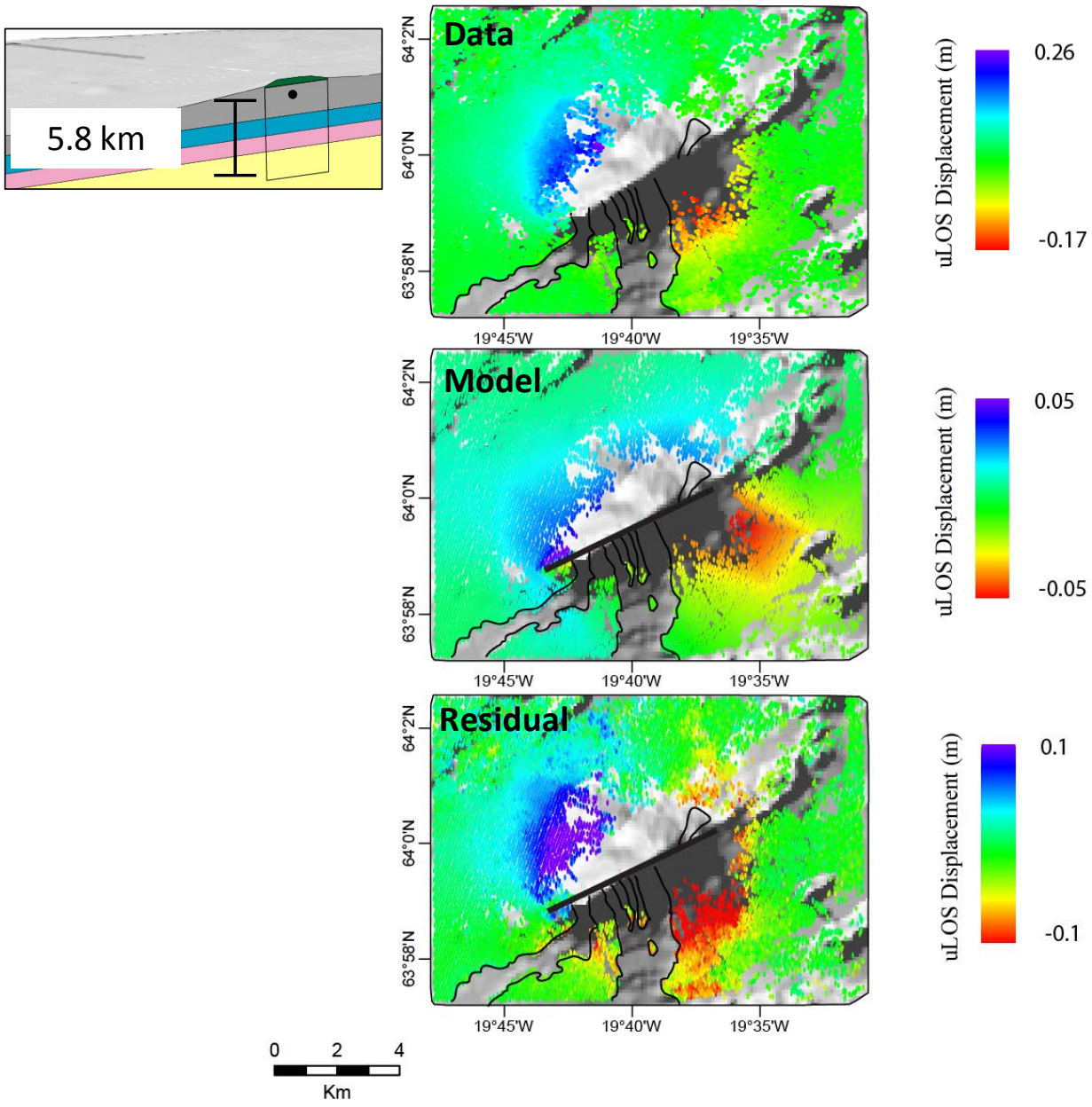

Figure 3.14. Results of LTs-5.2 (inset). The Young's modulus for the green layer is 12.8 GPa, grey layer is 14.3 GPa, blue layer is 27.7 GPa, pink layer is 33.5 GPa, and yellow layer (i.e. the rest of the model domain) is 30 GPa (Table 2.3). The black dot in the inset indicates sea level under the dike center. The top image is the InSAR data used, and the lava load is masked from the data, as indicated by black outlines in the figures. The dike is represented as a black line in the Model and Residual results. Strike and length of the dike is approximately to scale.

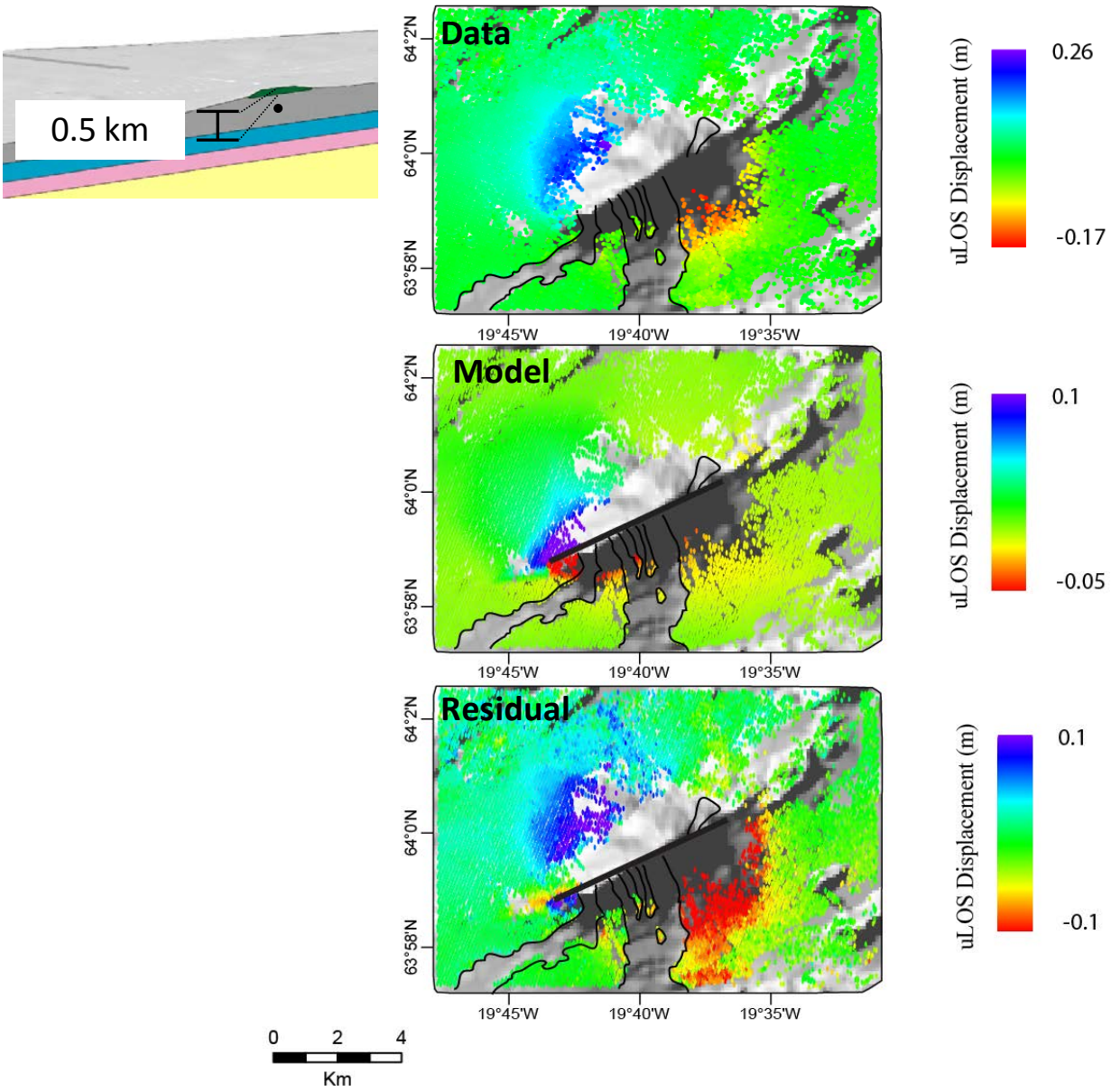

Figure 3.15. Results of LTt-3.2 (inset). The Young's modulus for the green layer is 12.8 GPa, grey layer is 14.3 GPa, blue layer is 27.7 GPa, pink layer is 33.5 GPa, and yellow layer (i.e. the rest of the model domain) is 30 GPa (Table 2.3). The black dot in the inset indicates sea level under the dike center. The top image is the InSAR data used, and the lava load is masked from the data, as indicated by black outlines in the figures. The dike is represented as a black line in the Model and Residual results. Strike and length of the dike is approximately to scale.

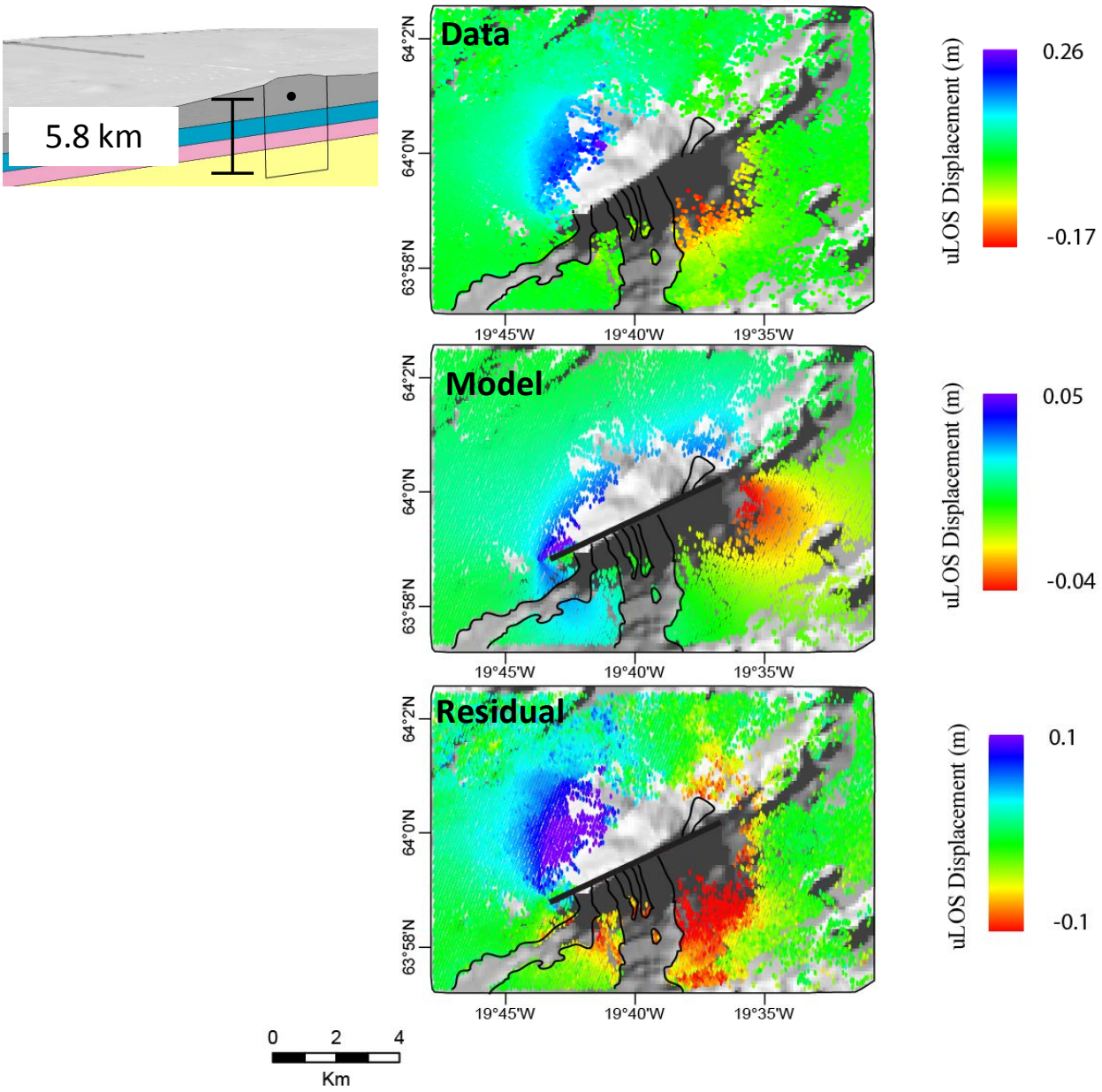

Figure 3.16. Results of LTs-5.1 (inset). The Young's modulus for grey layer is 14.3 GPa, blue layer is 27.7 GPa, pink layer is 33.5 GPa, and yellow layer (i.e. the rest of the model domain) is 30 GPa (Table 2.2). The black dot in the inset indicates sea level under the dike center. The top image is the InSAR data used, and the lava load is masked from the data, as indicated by black outlines in the figures. The dike is represented as a black line in the Model and Residual results. Strike and length of the dike is approximately to scale.

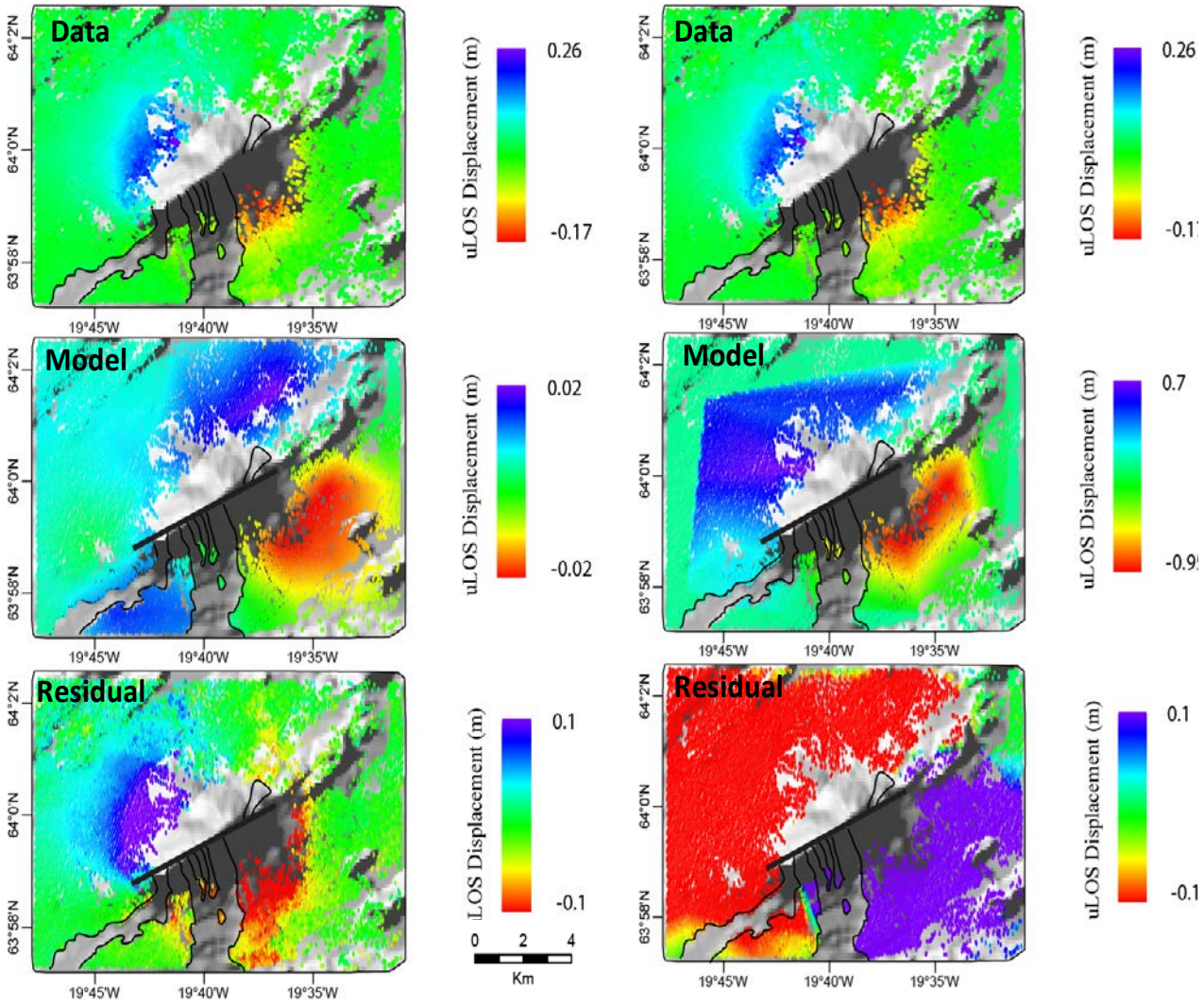

Figure 3.17. Results of the blind dikes. The figures on the left are from LTs-5.1b, while the figures on the right are from LTs-3.1b. The top images is the InSAR data used, and the lava load is masked from the data, as indicated by black outlines in the figures. The dike is represented as a black line in the Model and Residual results. Strike and length of the dike is approximately to scale.

Model LTs-5.1b predicts about 15 cm opening and 53 cm strike-slip which is different from the predicted dike behavior of Ts-5.1b (Table 3.1). Model LTs-5.1b predicts a range of ground deformation between -2 to 4 cm, while Ts-5.1b predicts ground deformation from -5 to 4 cm. Model LTs-5.2 predicts roughly the same amount of strike-slip as L-5.2, but about half the amount of opening. Ground deformation for LTs-5.2 has a range between -5 and 10 cm, whereas predicted ground deformation for L-5.2 ranges roughly between -30 and 45 cm.

Model LTs-3.1 predicts roughly 1.5 m of strike-slip (Table 3.4); approximately 25% smaller than the L-3.1 and L-3.1Y12 (Table 3.3). The predicted strike-slip from this model is nearly twice as large as that predicted by Ts-3 (Table 3.1). The predicted opening is slightly larger than the estimated opening for L-3.1 and L-3.2, but the covariance yields some overlap in results. The predicted opening for LTs-3.1 is approximately ten times that of Ts-3. The range of predicted deformation from this model is -21 to 50 cm, while Ts-3 predicts -4 to 6 cm of deformation while L-3.1 and L-3.1Y12 predict -33 to 46 cm deformation.

Model LTs-3.2 predicts 15 cm greater opening than LTs-3.1, but 30 cm less strike-slip. The range of deformation predicted by this model is -11 to 30 cm while the range of deformation predicted by L-3.2 is -31 to 38 cm. Model LTt-3.2, which completely contains the dike in that top layer, estimates 64 cm of opening, which is an increase of about 20 cm from the previous configuration and an increase in estimated strike-slip of nearly 1 m. This configuration predicts a deformation range of -33 to 79 cm. The estimated dike movement of LTs-3.1b predicts an opening of roughly 97 cm and strike-slip of 13.13 m. The range of deformations this configuration predicts is quite large: -1.16 to 1.87 m.

2. Discussion

Model LTs-5.1 indicates rock property layering plays a bigger role in the predicted movement of the dike, even though the dike is constrained to uniform displacement. The addition of topography affects the predicted surface deformations more. The behavior of the dike in model LTs-5.1b is affected by the layering but is less affected by the topographic edifice, indicating the extra load of the volcano still does not play much of a role in the behavior of a blind dike, even in the presence of layered rock properties which would transmit the stress differently homogeneous rock properties.

The movements and predicted deformation of the 0.35 km dike are much more variable, likely because this dike is more sensitive to the different inputs simply because of the small width. It is too small to pass through several different layers in the layered topographic FEMs, and so it is the best indicator of how each input may affect the predictions independent of the other inputs. The strike-slip estimates for the dike are drastically different, even given their relatively large magnitudes, but a clear trend of increased estimated opening is seen as the influence of the top layer increases. Of the configurations using a 0.35 km dike, LTs-3.1 has the smallest estimated opening, and the estimated opening increases by 15 cm for the configuration with a 0.5 km thick upper layer. The estimated opening increases another 20 cm for LTt-3.2.

The difficulty in finding a clear link with the layering, dike width, and strike-slip estimates could be related to the inferred change in strike of the fissure, although until the change in strike is determined and quantified, the level of influence cannot be calculated. The estimates for LTs-3.1b are larger than any other model configuration for both opening and strike-slip. The combination of weaker material allows larger movements of the fissure, as evidenced by the estimated 13 m of strike-slip motion, and this large movement is required to predict the

deformation signal of the InSAR. The large range of movements is extremely close to the dike and drop off quickly with distance, such that much of the deformation has decayed before reaching the area covered by the InSAR.

The relationship between topography and layering seems to indicate that the topography dominates ground deformation values. Layering, on the other hand, dominates estimated dike movement, especially estimated opening for the smaller dike. The smaller dike does not pass through multiple layers, but even when it does, the layers do not have drastically different rock properties. This allows the rock properties to influence the estimated movements of the dike. The behavior of the larger dike is essentially the same regardless of the layering, and this probably because the layers are acting in a composite manner, rather than on an individual basis, so a drastic change in the layering or overall rock properties is needed before major differences in estimates will occur.

SUMMARY OF ALL RESULTS

1. F-Test results

Deciding to include topography, layering, or both in a model hinges on the important question of statistically improved results from the new configurations. The results of an F-test indicate whether the results are a statistical improvement based on the critical value. The results of the F-tests between all models is in Table 3.5. Table 3.6 is an annotated version of Table 3.5. In Table 3.6, only results between configurations of the same dike width are included, and comparisons producing an F-test value smaller than the critical value are set to zero. The results indicate the HEHS models yield the best predictions, but this is not always the case, as evidenced by the residuals for H-5 compared to Ts-5 or Tt-5 (Figures 2.25, 3.1, and 3.3, respectively). The

Table 3.5. F-Test results for comparisons of all models. Each column represents the "new model" (i.e. the model being tested), while each row represents the "baseline" model. Values for the SSE are given for each model as a reference. As an example; the value of 0.747 is the value of the F-test statistic testing if model H-3 predicts the data better than model H-5. Because the value is less than 1.03 (i.e. the critical value), H-3 does not predict the data better than H-5, although the comparison is technically invalid due to the different fissure geometries in the two models. This is addressed in Table 3.6.

	S_1	H-5	H-3	Ts-5	Ts-5b	Tt-5	Ts-3	Tt-3	Ts-3b	L-5.1	L-3.1	L-3.1Y12	L-3.2	L-5.2	LTs-3.2
S_0	SSE	15.72	21.04	134.3	108	141.8	111	100	1773	16.65	23.03	24.2	23.4	23.2	47
H-5	15.716	1	0.747	0.117	0.146	0.111	0.142	0.157	0.009	0.944	0.682	0.649	0.672	0.677	0.334
H-3	21.04		1	0.157	0.195	0.148	0.190	0.210	0.012	1.264	0.914	0.869	0.899	0.907	0.448
Ts-5	134.25			1	1.243	0.947	1.209	1.343	0.076	8.063	5.829	5.548	5.737	5.787	2.856
Ts-5b	108				1	0.762	0.973	1.080	0.061	6.486	4.690	4.463	4.615	4.655	2.298
Tt-5	141.8					1	1.277	1.418	0.080	8.517	6.157	5.860	6.060	6.112	3.017
Ts-3	111						1	1.110	0.063	6.667	4.820	4.587	4.744	4.784	2.362
Tt-3	100							1	0.056	6.006	4.342	4.132	4.274	4.310	2.128
Ts-3b	1772.9								1	106.480	76.982	73.260	75.765	76.418	37.721
L-5.1	16.65									1	0.723	0.688	0.712	0.718	0.354
L-3.1	23.03										1	0.952	0.984	0.993	0.490
L-3.1Y12	24.2											1	1.034	1.043	0.515
L-3.2	23.4												1	1.009	0.498
L-5.2	23.2													1	0.494
LTs-3.2	47														1

Table 3.5 (cont'd).

	S_1	LTs-5.2	LTt-3.2	LTs-5.1	LTs-3.1	LTs-5.1b	LTs-3.1b
S_0	SSE	43.8	52.06	38.93	66.4	34.02	2179
H-5	15.716	0.359	0.302	0.404	0.237	0.462	0.007
H-3	21.04	0.480	0.404	0.540	0.317	0.618	0.010
Ts-5	134.25	3.065	2.579	3.448	2.022	3.946	0.062
Ts-5b	108	2.466	2.075	2.774	1.627	3.175	0.050
Tt-5	141.8	3.237	2.724	3.642	2.136	4.168	0.065
Ts-3	111	2.534	2.132	2.851	1.672	3.263	0.051
Tt-3	100	2.283	1.921	2.569	1.506	2.939	0.046
Ts-3b	1772.9	40.477	34.055	45.541	26.700	52.113	0.814
L-5.1	16.65	0.380	0.320	0.428	0.251	0.489	0.008
L-3.1	23.03	0.526	0.442	0.592	0.347	0.677	0.011
L-3.1Y12	24.2	0.553	0.465	0.622	0.364	0.711	0.011
L-3.2	23.4	0.534	0.449	0.601	0.352	0.688	0.011
L-5.2	23.2	0.530	0.446	0.596	0.349	0.682	0.011
LTs-3.2	47	1.073	0.903	1.207	0.708	1.382	0.022
LTs-5.2	43.8	1	0.841	1.125	0.660	1.287	0.020
LTt-3.2	52.06		1	1.337	0.784	1.530	0.024
LTs-5.1	38.93			1	0.586	1.144	0.018
LTs-3.1	66.4				1	1.952	0.030
LTs-5.1b	34.02					1	0.016
LTs-3.1b	2179						1

Table 3.6. Annotated F-Test results for valid comparisons between models. Results for models with different fissure geometry or different starting points (for the topography models) are not included. A value of zero indicates the model at the top of the column does not predict the data better that the model at the left of the row, while a non-zero value indicates the value of the F-test statistic.

	H-5	H-3	Ts-5	Ts-5b	Tt-5	Ts-3	Tt-3	Ts-3b	L-5.1	L-3.1	L-3.1Y12	L-3.2	L-5.2	LTs-3.2
H-5	0		0	0	0				0				0	
H-3		0								0	0	0		0
Ts-5			0	1.2431	0				8.0631				5.7866	
Ts-5b				0	0				6.4865					
Tt-5					0				8.5165					
Ts-3						0	1.11	0		4.8198	4.58678	4.744		2.3617
Tt-3							0	0		4.3422	4.13223	4.274		2.1277
Ts-3b								0		76.982	73.2603	75.76		37.721
L-5.1									0				0	
L-3.1										0	0	0		0
L-3.1Y12											0	1.034		0
L-3.2												0		0
L-5.2													0	
LTs-3.2														0

Table 3.6. (cont'd)

	LTs-5.2	LTt-3.2	LTs-5.1	LTs-3.1	LTs-5.1b	LTs-3.1b
H-5	0		0		0	
H-3		0		0		0
Ts-5	3.0651		3.4485			
Ts-5b					3.1746	
Tt-5						
Ts-3				1.6717		
Tt-3		1.9209				
Ts-3b						0
L-5.1	0		0		0	
L-3.1		0		0		0
L-3.1Y12	0			0		0
L-3.2		0		0		0
L-5.2	0		0		0	
LTs-3.2		0		0		0
LTs-5.2	0		1.1251		1.28748	
LTt-3.2		0				
LTs-5.1			0			
LTs-3.1				0		
LTs-5.1b					0	
LTs-3.1b						0

HEHS model predicts smaller deformations, and so has smaller error values overall (Table 3.2), but more of them (Figure 2.26) indicating this model does not, in fact, predict the deformation better than the equivalent models with topography. The topographic models using a 0.35 km wide dike cannot be compared to the equivalent HEHS model (i.e. H-3) because that model uses different rock properties than the topography model.

Results of the F-tests between the layered HEHS models and equivalent HEHS indicate the HEHS models do a better job fitting the data, and a visual comparison between results confirms this assertion, indicating adding the layers used in this study does not improve predictions of a HEHS model. Results of the F-tests between the topographic FEMs and the layered topographic FEMs, however, indicate adding layering to topographic FEMs does improve predictions. Keep in mind that configurations using different starting reference elevations should not be compared because the dikes will have a different surface area (i.e. blind dikes for the topographic FEM should be compared only with the topographic layered FEM using the same blind dike). Visual inspection of the results for both models (Figures 3.1-3.2, 3.4-3.6 and 3.13 to 3.17 respectively) indicate the F-test results do not apply to the topographic models using a 5.8 km wide dike, but do apply to the models using a 0.35 km dike.

2. General Discussion

Definite differences are seen in estimates of dike behavior and deformation from the HEHS model and the topographic FEM and layered topographic FEM. The differences between predictions from the LEHS model and an equivalent HEHS model are more ambiguous. The predictions of the layered topographic FEM are different than predictions of the homogeneous topographic FEM, indicating a relationship exists between layering and topography, which

would otherwise be overlooked and could produce biased results if only topography or only layering is included. It is likely this interplay is related to the shape and extent of the volcanic edifice, thickness of layers, and contrast of rock properties between layers.

The addition of topography into a HEHS model for an area with significant relief (such as a volcanic edifice) changes some fundamental aspects of the model such that effects of topography may be more significant than even source geometry (Williams and Wadge, 2000). This is evident in the topographic FEM of this study. The addition of topography alters the predictions of both dike movement and estimated ground deformation. The F-test results do not indicate a bulk statistical improvement of predictions from topographic FEMs compared to an uncorrected HEHS, but visual inspection of residuals indicates the F-test results may be biased due to larger displacements predicted by the topographic FEMs. Topographic FEMs also allow exploration of various dike configurations, such as one whose geometry changes with depth, that are not possible to analyze with HEHS models and topographic corrections. Such a configuration, however, has been indicated at Hekla both by the results of this study and the geologic history of the area. Implementing the new modeling techniques demonstrated here is crucial if these geometries are to be explored.

The different LEHS configurations for a larger dike do not predict relatively different ground deformations or strike-slip predictions than a HEHS, although the opening predicted by a dike with the weaker top layer indicates the weaker layer can affect the opening estimate of the entire dike, but the overall nature of the properties is most important. A larger dike in a stiffer volume can transmit strain farther distances than a smaller dike in a weaker material (equation 1.1.). The combination of weaker material properties and poor data coverage near the dike contributes to the larger prediction values for deformation and dike movement in models where

the dike has a smaller width. Results of the F-test also indicate the layered HEHS models do not predict the data better than the equivalent HEHS models. If an HEHS model is utilized to model dike behavior, results of this study indicate the assumption of homogeneity in the model will not negatively affect model predictions.

The combination of topography and layering into a single model indicates predictions of dike behavior are more influenced by the material properties than by the addition of topography, although ground deformation estimates may be more sensitive to topography. These effects are more pronounced with a smaller dike. The larger dike is relatively unaffected by the different properties of the layers because the predicted movement and ground deformations are a result of the combined layer properties. Individual layers do not affect the predicted dike movements. The difference between layered topographic FEMs of smaller versus larger dikes is also evident in results of the F-tests and visual inspection of the model predictions. The F-tests indicate all layered topographic models predict the data better than their equivalent topographic FEMs (Table 3.5), but visual inspection of the results indicates the topographic FEMs of the 5.8 km wide dike predict the data better than the layered topographic FEMs, while the opposite is true for FEMs of the 0.35 km dikes. Because the layering has more of an effect on the smaller dike, and those models yield better predictions than models which do not include layering, it is recommended layering be included in topographic FEMs of dike behavior during an eruption.

The results of this study support a shift in the modeling world from HEHS models to FEMs. Discounting rock property layering in topographic FEMs can lead to results of dike movement which are biased in a manner related to these inputs. The flexibility and power of FEMs far outweighs the computational burden they may present, and that burden will only continue to lessen with advancing technology.

CHAPTER 4

PROJECT CONCLUSIONS

Utilizing layered rock properties in a model with topography directly input as the free-surface is something unprecedented in modeling dike behavior. Improving the model further, as discussed in this chapter, could help make such models the standard rather than the exception Commonly employed assumptions, previously required to complete analyses in a reasonable time, are biasing results in a manner which prevents accurate dike parameter estimates. The different configurations of the FEM with topography highlight different considerations and dike orientations made possible only by including topography in the model domain. The most important implication for these models is the possibility of a change in strike of the Hekla dike at depth. HEHS models require a square dike geometry which cannot change in the model domain, and the topographic corrections are basically an addition to the depth of calculation points in the model. The possibility of exploring different dike which changes shape or orientation between the volcanic edifice and the areas of the domain below sea level is not possible with topographic corrections.

Also, a dike which intersects the surface cannot be modeled at all with topographic corrections, even though there is a surface expression of the dike at Hekla. Different parts of the eruptive fissure are observed to be active at different times during the past several eruptions (Grönvold et al., 1983; Gudmundsson et al., 1992; Höskuldsson et al., 2007; Thorarinsson and Sigvaldason, 1972), indicating perhaps different parts of the dike and eruptive fissure may

behave independently during an eruption. Such a consideration requires models which allow the dike to intersect the surface, but such a configuration is not possible with topographic corrections. In fact, in the Williams and Wadge (1998, 2000) corrections, a dike which intersects the topographically-corrected surface will cause a singularity in the calculations. Also, the preferred simple topographic correction from Williams and Wadge (1998) is not possible in areas of extreme topography. The calculation results in a model configuration similar to the "blind fissure" configuration used here. The topographic corrections which have been utilized have too many restrictions, and these restrictions may be what is preventing an accurate and consistent estimate of the dike geometry of Hekla.

The difference in estimated dike movements and predicted ground deformations between the LEHS and HEHS models indicate the overall layering of a domain may influence the estimated movement of the dike. The predicted ground deformations, however, are more sensitive to the properties of the top layer, and possibly the second layer if the top layer is sufficiently thin.

Models which follow HEHS assumptions have thus far produced estimates of the dike geometry which vary widely, indicating a fundamental change may be needed to the models. The addition of topography and layering of rock properties should be included in future inversions of the dike geometry at Hekla as well as at other volcanoes with significant relief and known (or estimated) heterogeneities in the rock properties. Although only vertical layering is explored in this study, lateral variations is rock properties can also be included in FEMs.

SUGGESTIONS FOR FUTURE WORK

Several options should be explored to improve the predictions of the models, even though the dike geometry is fixed. These include modeling the dike with a distributed opening and/or changing the kinematic constraint equations. Using distributed movement along a fault (or fissure) plane has groundwork laid in previous research using other study sites (e.g. Menodza and Hartzell, 1999, Hughes and Masterlark, 2008) and would be very useful at Hekla. The biggest surface area of the best-fit geometries (i.e. a 6.6 km by 5.8 km fissure) would provide the most coverage and best allow the model to indicate the specific movement for each patch of the fissure. The first question associated with this model relates to the best number of patches to use because each patch requires a separate FEM. A good starting point may be a design which splits the fissure in half vertically and has a new patch every 1 km from the top of Hekla summit. This can be done in Abaqus by partitioning the dike and assigning each partition a specific name. The elements and nodes along the partitions can then be separated out and have unique values applied to them in the kinematic constraint equations. The results of these forward models can be solved for simultaneously by expanding the dimensionality of the G matrix. Laplacian smoothing, such that each patch cannot move in a different direction or by a significantly different amount from its neighboring patch, can help the inversion arrive at the most plausible solution. The result would be the estimated slip of each patch according to the equation 2.5. The best-fit geometry of a vertical dike could be indicated using this method as well because areas along the dike which are not needed would likely decay to relatively zero displacement. For example, if the length of the dike should really be 4 km, the predicted movement for the outside 1 km of the dike on either side may be near zero.

Simulating dike behavior as a fault is not new, but running such simulations in a 3-D FEM is innovative, and results from this study indicate the FEM is a necessary improvement on the HEHS model. While the model configuration of this study is specific to Hekla, FEMs can be applied to any active volcano with dikes and/or sills moving through the system. Use of an FEM rather than a HESH model makes more sense at volcanoes with significant relief and well constrained rock properties.

Although beyond the scope of this dissertation, these estimated displacements from an improved model could be transformed into pressures using equations 1.1 and compared to estimated pressures/depths of the magma chamber under Hekla, because the pressure of the magma chamber is related to the amount of opening of the fissure (Buck et al., 2006). Such a comparison would elucidate the nature of the connection between the fissure and the magma chamber at depth.

In summary, the general conclusions of this study are:

1. Embedding topography into an FEM of dike movement improves the predictions of the fissure movement, but including layers in a HEHS model does not change nor improve the predictions of uniform dike movement as much.
2. The strike of Hekla fissure may not represent the strike of the dike at depth, and FEMs with topography included may be able to elucidate changes of the strike (and possibly other geometric changes) due to the presence of the volcano itself.
3. Layered topographic FEMs have shown that dike movement is more sensitive to the relationship between dike width and overall layering of the model given the constraint of

uniform dike movement, but the predicted ground deformations are more sensitive to dike width and the properties of the top layers.

4. Layered topographic FEMs of a smaller dike, which is more influenced by layering than a larger dike, produce better results than topographic FEMs using an assumption of homogeneity.

Future work indicated by the results of this study include:

1. Re-evaluation of the conceptual model to include distributed movement of the dike could elucidate many issues with the best-fit geometry. The predictions of each patch would indicate the best-fit geometry for a dike at any given dip. The effect of distributed opening within a homogeneous topographic FEM may be a good starting point for such models, especially if better tomography under the volcano is not available. The ability of each patch to move freely could compensate for unknown variations in the rock properties and still provide useful information for dike behavior during the eruption.

2. Better seismic tomography of rock properties under Hekla is needed. While beyond the scope of this project, improved tomography would greatly benefit any future models of Hekla. The 1-D crustal model used to create rock layering for this study is based off crustal properties roughly 15 km south east of the volcano. Ideally, tomography would be fully 3-D, down to at least 1 km below sea level, but a high-resolution 1-D profile directly on the edifice of Hekla to 1 km depth would also be very useful.

COMPLETE REFERENCE LIST

Acocella, V., and Neri, M., 2009, Fissure propagation in volcanic edifices: Overview and possible developments: Tectonophysics, v. 471, p. 67-77.

Anderson, K., and Segall, P., 2011, Physics-based models of ground deformation and extrusion rate at effusively erupting volcanoes: Journal of Geophysical Research, v. 116, B07204, doi:10.1029/2010JB007939.

Árnadóttir, T., Jónsson S., Pollitz, F.F., Jiang, W., and Fiegl, K., 2005, Postseismic deformation following the June 2000 eathquake sequence in the south Iceland seismic zone: Journal of Geophysical Research, v. 110, B12308, doi: 10.1029/2005JB003701.

Árnadóttir, T., Lund, B., Jian, W., Geirsson, H., Björnsson, H., Einarsson, P., and Sigurdsson, T., 2009, Glacial rebound and plate spreading: results from the first countrywide GPS observations in Iceland: Geophysical Journal International, v. 177, p. 691-716.

Bensen, G.D., Ritzwoller, M.H., Barmin, M.P., Levshin, A.L., Lin, F., Moschetti, M.P., Shapiro, N.M., and Yang, Y., 2007, Processing seismic ambient noise data to obtain reliable broad-band surface wave dispersion measurements: Geophysical Journal International, v. 169, doi:10.1111/j.1365-246X.2007.03374.x.

Biggs, J., Mothes, P., Ruiz, M., Dixon, T.H., Baker, S., and Hong, S-H., 2010, Stratovolcano growth by co-eruptive intrustion: the 2008 eruption of Tungurahua Ecuador: Geophysical Research Letters, v. 37, L21302, doi:10.1029/2010GL044942.

Brandsdottir, B., and Menke, W.H., 2008, The seismic structure of Iceland *in* The dynamic Geology of Iceland: Jokull, No. 58, p. 17-34.

Buck, W.R., Einarsson, P., and Brandsdottir, B., 2006, Tectonic stress and magma chamber size as controls on fissure propagation: Constraints from the 1975-1984 Krafla rifting episode: Journal of Geophysical Research, v. 111, B12404, doi:10.1029/2005JB003879.

Christensen, N.I., and Mooney, W., 1995, Seismic velocity structure and composition of the continental crust: A global review: Journal of Geophysical Research, v. 100, p. 9761-9788.

Christensen, N.I., 1996, Poisson's ratio and crustal seismology: Journal of Geophysical Research, v. 101, p. 3139-3156.

Darbyshire, F.A., White, R.S., and Priestley, K.F., 2000, Structure of the crust and uppermost mantle of Iceland from a combined seismic and gravity study: Earth and Planetary Science Letters, v. 181, p. 409-428.

Decker, R.W., Einarsson, P., and Mohr, P.A., 1971, Rifting in Iceland: New Geodetic Data: Science, v. 173, p. 530-533.

Decriem, J., Árnadóttir, T., Hooper, A., Geirsson, H., Sigmundsson, F., Keiding, M., Ofeigsson, B.G., Hreinsdottir, S., Einarsson, P., LaFemina, P., and Bennett, R.A., 2010, The 2008 May 29 earthquake doublet in SW Iceland: Geophysical Journal International, v. 181, doi: 10.1111/j.1365-246X.2010.04565.x.

Dugmore, A. J., Newton, A.J., Edwards, K.J., Larson, G., Blackford, J.J., and Cook, G.T., 1996, Long-distance marker horizons from small-scale eruptions: British tephra deposits from the AD 1510 eruption of Hekla, Iceland: Journal of Quarternary Science, v. 11, p. 511-516.

Einarsson, T., 1950, Chemical analyses and differentiation of Hekla's magma: The eruption of Hekla 1947–1948, 4, 4, Societas Scientiarum Islandica, Reykjavík, 44 p.

Fedorova, T., Jacoby, W.R., and Wallner, H., 2005, Crust-mantle transition and Moho model for Iceland and surroundings from seismic, topography, and gravity data: Tectonophysics, v. 296, p. 119-140.

Fiske, R.S., and Jackson, E.D., 1972. Orientation and growth of Hawaiian volcanic rifts: the effect of regional structure and gravitational stresses. Proceedings of the Royal Society of London, v. 329, p. 299–326.

Fukushima, Y., Cayol, V., Durand, P., and Massonnet, D., 2010, Evolution of magma conduits during the 1998-2000 eruptions of Piton de la Fournaise volcano, Réunion Island: Journal of Geophysical Research, v. 115, doi:10.1029/2009JB007023.

Geirsson, H., LaFemina, P., Árnadóttir, T., Sturkell, E., Sigmundsson, F., Travis, M., Schmidt, P., Lund, B., Hreinsdóttir, S., and Bennett, R., 2012, Volcano deformation at active plate boundaries: Deep magma accumulation at Hekla volcano and plate boundary deformation in south Iceland: Journal of Geophysical Research, v. 117, B11409, doi:10.1029/2012JB009400.

Giberti, G., and Wilson, L., 1990, The influence of geometry on the ascent of magma in open fissures: Bulletin of Volcanology, v. 52, p. 515-521.

Grapenthin, R., Ofeigosson, B., Freysteinn, S., Sturkell, E., and Hopper, A., 2010, Pressure sources versus surface loads: Analyzing volcano deformation signal composition with an application to Hekla volcano, Iceland: Geophysical Research Letters, v., 37, doi:10.1029/2010GL044590.

Gronvöld, K., Larsen, G., Einarsson, P., Thorarinsson, S., and Saemundsson, K., 1983, The Hekla eruption 1980-1981: Bulletin of Volcanology, v. 46, p. 349-363.

Gudmundsson, A., Oskarsson, N., Gronvöld, K., Saemundsson, K., Sigurdsson, O., Stefansson, R., Gislason, S., Einarsson, P., Brandsdottir, B., Larsen, G., Johannesson, H., and Thordarson, T., 1992, The 1991 eruption of Hekla: Bulletin of Volcanology, v. 54, p. 238-246.

Jónsson S., Einarsson, P., and Sigmundsson, F., 1997, Extension across a divergent plate boundary, the Eastern Volcanic Rift Zone, south Iceland, 1967-1994, observed with GPS and electronic distance measurements: Journal of Geophysical Research, v. 102, p. 11,913-11,929.

Haney, M., Nies, A., Masterlark, T., Needy, S., and Pedersen, R., 2011, Interpretation of Rayleigh-wave ellipticity observed with multicomponent passive seismic interferometry at Hekla Volcano, Iceland: The Leading Edge, May, p. 526-531.

Heap, M.J., Vinciguerra, S., and Meredith, P.G., 2009, The evolution of elastic moduli with increasing crack damage during cyclic stressing of a basalt from Mt. Etna volcano: Tectonophysics, v. 471, p. 153-160.

Höskuldsson, A., Oskarsson, N., Pedersen, R., Gronvöld, K., Vogfjord, K., and Olafsdottir, R., 2007, The millennium eruption of Hekla in February, 2000: Bulletin of Volcanology, v. 70, p. 169-182.

Hughes, K.L.H., and Masterlark, T., 2008, Slip distribution for the 2004 Sumatra-Andaman earthquake constrained by both GPS data and tsunami run-up measurements: Bollettino di Geofisica: Teorica ed Applicata, v. 49, p. 165-169.

Hughes, K.L.H., 2011, Coseismic and postseismic deformation of the great 2004 Sumatra-Andaman Earthquake, Doctoral Dissertation: Alabama, 216 p.

Kaban, M.K., Flovenz, O.G., and Palmason, G., 2002, Nature of the crust-mantle transition zone and the thermal state of the upper mantle beneath Iceland from gravity modeling: Geophysical Journal International, v. 149, p. 281-299.

Kelly, D. F. and Barton, M., 2008, Pressures of crystallization of Icelandic magmas: Journal of Petrology, v. 49, p. 465-492.

LaFemina, P.C., Dixon, T.H., Malservisi, R., Árnadóttir, T., Sturkell, E., Sigmundsson, F., and Einarsson, P., 2005, Geodetic GPS measurements in south Iceland: Strain accumulation and partitioning in a propagating ridge system: Journal of Geophysical Research, v. 110, B11405, doi:10.1029/2005JB003675.

Lillesand, T.M., Kiefer, R.W., and Chipman, J.W., 2004, Remote sensing and Image Interpretation: New York, John Wiley and Sons, Inc., 5th ed, 763 p.

Linde, A.T., Agustsson, K., Sacks, S., and Stefansson, R., 1993, Mechanism of the 1991 eruption of Hekla from continuous borehole strain monitoring: Nature, v. 365, p. 737-740.

Maclennan, J., McKenzie, D., Gronvöld, K., and Slater, L., 2001, Crustal accretion under northern Iceland: Earth and Planetary Science Letters, v. 191, p. 295-310.

Masterlark, T., 2003, Finite element model predictions of static deformation from dislocation sources in a subduction zone: Sensitivities to homogeneous, isotropic, Poisson-solid, and half-space assumptions*:* Journal of Geophysical Research, v. 108, doi:10.1029/2002JB002296.

Masterlark, T., 2007, Magma intrusion and deformation predictions: sensitivities to the Mogi assumptions: Journal of Geophysical Research, v. 112, B06419, doi:10.1029/2006JB004860.

Masterlark, T., and Hughes, K.L.H., 2008, Next generation of deformation models for the 2004 M9 Sumatra-Andaman earthquake: Geophysical Research Letters, v. 35, doi:10.1029/2008GL035198.

Masterlark, T., Haney, M., Dickinson, H., Fournier, T., and Searcy, C., 2010, Rheologic and structural controls on the deformation of Okmok volcano, Alaska: FEMs, InSAR, and ambient noise tomography: Journal of Geophysical Research, v. 115, doi:10.1029/2009JB006324.

Masterlark, T., Fiegl, K.L., Haney, M.M., Stone, J., Thurber, C.H., and Ronchin, E., 2012, Nonlinear estimation of geometric parameters in FEMs of volcano deformation: Integrating tomography models and geodetic data for Okmok volcano, Alaska, Journal of Geophysical Research, v. 117, doi:10.1029/2011JB008811.

Mendoza, C., and Hartzell, S., 1999, Fault-slip distribution of the 1995 Colima-Jalisco, Mexico, earthquake: Bulletin of the Seismological Society of America, v. 89, p. 1338-1444.

Mogi, K., 1958, Relations between the eruptions of various volcanoes and the deformations of the ground surfaces around them: Bulletin of Earthquake Research Institute, v. 36, p. 99-134.

Menke, W., 1989, Geophysical Data Analysis: Discrete Inverse Theory: San Diego, Academic International Geophysics Series, v. 45, 289 p.

Ofeigsson, B.G., Hooper, A., Sigmundsson, F., Sturkell, E., and Grapenthin, R., 2011, Deep magma storage at Hekla volcano, Iceland, revealed by InSAR time series analysis: Journal of Geophysical Research, v. 116, doi:10.1029/2010JB007576.

Okada, Y., 1992, Internal deformation due to shear and tensile faults in a half space: Bulletin of the Seismological Society of America, v. 82, p. 1018-1040.

Pedersen, R., Jónsson S., Árnadóttir, T., Sigmundsson, F., and Feigl, K.L., 2003, Fault slip distribution of two June 2000 Mw6.5 earthquakes in South Iceland estimated from joint inversion of InSAR and GPS measurements: Earth and Planetary Science Letters, v. 213, p. 487-502.

Pedersen et al., 2009, Using finite element modeling (FEM) to investigate complex inter-eruptive deformation pattern observed at Hekla volcano, Iceland, *AGU-Fall Meeting*, San Francisco, CA (abstract).

Roth, F., 1990, Subsurface deformations in a layered elastic half-space: Geophysical Journal International, v. 103, p. 147-155.

Shapiro, N.M., Campillo, M., Stehly, L., and Ritzwoller, M., 2005, High resolution surface wave tomography from ambient seismic noise, Science, v. 307, p. 1615– 1618, doi:10.1126/science.1108339.

Sigmarsson, O., Hémond, C., Condomines, M., Fourcade, S., and Oskarsson, N., 1991, Origin of silicic magma in Iceland revealed by Th isotopes: Geology, v. 19, p. 621-624.

Sigmundsson, F., 2006, Iceland geodynamics; crustal deformation and divergent plate tectonics. Springer, 209 pp.

Sigvaldason, G., 1974, The petrology of Hekla and origin of silicic rocks in Iceland: The eruption of Hekla 1947–1948, 5, 1, Societas Scientiarum Islandica, Reykjavík, 44 p.

Solaro, G., Acocella, V., Pepe, S., Ruch, J., Neri, M., and Sansosti, E., 2010, Anatomy of an unstable volcano from InSAR: Multiple processes affecting flank instability at Mt. Etna, 1994, 2008: Journal of Geophysical Research, v. 115, doi:10.1029/2009JB000820.

Soosalu, H., and Einarsson, P., 1997, Seismicity around the Hekla and Torfajokull volcanoes, Iceland, during a volcanically quiet period, 1991-1995: Bulletin of Volcanology, v. 59, p. 36-48.

Soosalu, H., Einarsson, P., and Thorbjarnardottir, B.S., 2005, Seismic activity related to the 2000 eruption of the Hekla volcano, Iceland: Bulletin of Volcanology, v. 68, p. 21-36.

Sturkell, E., Ágústssonb, K., Linde, A.T., Sacks, S., Einarsson, P., Sigmundsson, F., Geirsson, H., Pedersen, R., LaFemina, P., and Olafsson, H., 2013, New insights into volcanic activity from strain and other deformation data for the Hekla 2000 eruption: Journal of Volcanology and Geothermal Research: v. 256, p. 78-86.

Swindles, G., Lawson, I.T., Savov, I.P., Connor, C.B., and Plunkett, G., 2011, A 7000 yr perspective on volcanic ash clouds affecting northern Europe: Geology, v. 39, doi: 10.1130/G32146.1.

Thorarinsson, S., 1967a, The eruptions of Hekla in historical times, *in* Eruption of Hekla 1947-1948: Societas Scientiarium Islandica, ser. 5, p. 1-44.

Thorarinsson, S., and Sigvaldason, G.E., 1972, The Hekla eruption of 1970: Bulletin of Volcanology, v. 36, p. 269-288.

Tryggvason, E., 1994, Observed ground deformation at Hekla, Iceland prior to and during the eruption of 1970, 1980-1981, and 1991: Journal of Volcanology and Geothermal Research, v. 61, p. 281-291.

Turcotte, D.L., and Schubert, G.J., 2002, Geodynamics: Applications of continuum physics to geologic problems, 2nd ed: Cambridge University Press, New York, 456 p.

Wang, H.F., 2000, Theory of Linear Poroelasticity: With Applications to Geomechanics: Princeton, Princeton University Press, 287 p.

Williams, C., and Wadge, G., 2000, An accurate and efficient method for including the effects of topography in three-dimensional elastic models of ground deformation with applications to radar interferometry: Journal of Geophysical Research, v. 105, p. 8103-8120.